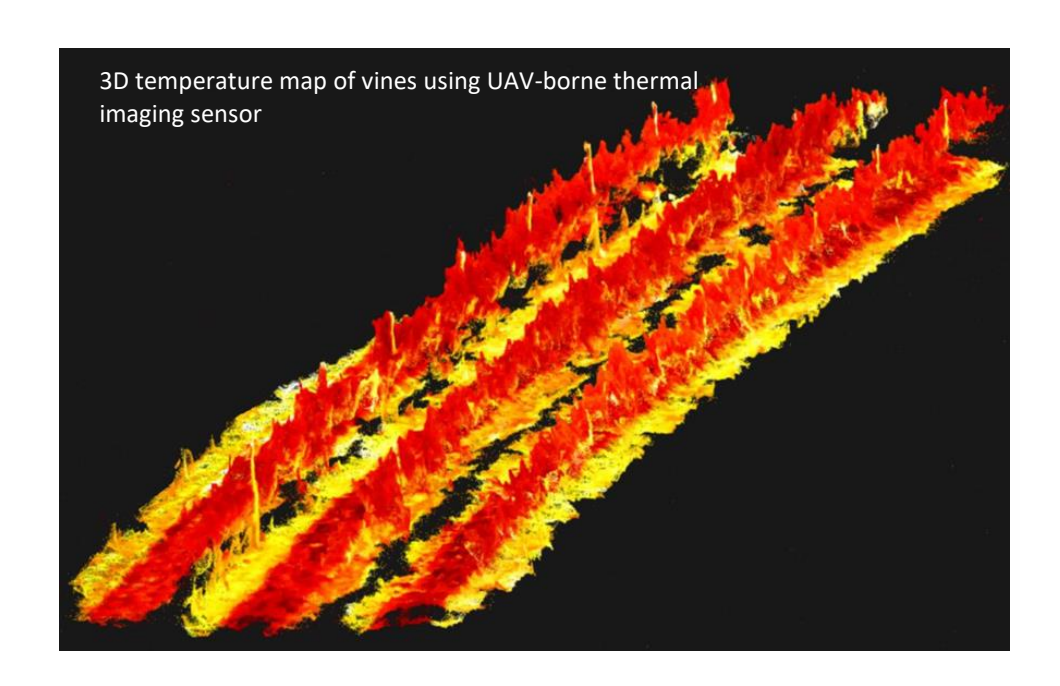






# Use of Unmanned Air Vehicles for Early Detection of Extreme Weather Events in Vineyards



## FINAL REPORT TO WINE AUSTRALIA

Project Number: USA 1601

Principal Investigator: Professor Anthony Finn

Research Organisation:

**Defence and Systems Institute, University of South Australia** 

Date: October 2019

Title: Use of Unmanned Air Vehicles for Early Detection of Extreme Weather Events in

Vineyards

**Author:** Professor Anthony Finn

Defence and Systems Institute, University of South Australia

Mawson Lakes, SA 5095

**Principle Investigator:** Professor Anthony Finn, Director of the Defence and Systems Institute (DASI) at the

University of South Australia

Email: anthony.finn@unisa.edu.au

Telephone: +61 8 8302 5703

Date October 2019

The content of this document is confidential and was prepared exclusively for Wine Australia. It is not intended for, nor does University of South Australia accept any responsibility for, its use by any third party. The report is Copyright University of South Australia and may not be reproduced without permission. All rights reserved.

# **Contents**

| Abstract                         |   |   |    |  |
|----------------------------------|---|---|----|--|
| Executive Summary                |   |   | 5  |  |
| Structure of this report         |   |   |    |  |
| P                                | articip   | pants   | 7  |  |
| 1                                | Pro   | oject rationale and objectives                              | 7  |  |
| 2                                | Te  | chnology concepts and components                            | 8  |  |
|                                  | 2.1   | Acoustic Atmospheric Tomography                             |    |  |
|                                  | 2.2   | LWIR Thermography   | 9  |  |
|                                  | 2.3   | Structure from motion                                       | 11 |  |
|                                  | 2.4   | Multi-UAV Acoustic Tomography                               |    |  |
|                                  | 2.5   | Equipment Details   | 13 |  |
| 3                                | B Field deployments and assessment                            |   | 17 |  |
|                                  | 3.1   | Performance assessment: simulation                          |    |  |
|                                  | 3.2   | Performance assessment: field comparisons                   |    |  |
| 4                                | Fie   | eld measurements  | 26 |  |
| •                                | 4.1   | Heat stress easurements                                     |    |  |
|                                  | 4.2   | Frost event measurements                                    |    |  |
| 5                                | De  | etermination of vineyard properties                         | 59 |  |
| 6                                | Pro   | oject evaluation: potential for adoption and lessons learnt | 74 |  |
| 7                                | Со  | oncluding remarks and future work                           | 76 |  |
| 8 Project media and publications |   | 78  |    |  |
| 9                                | Int   | tellectual property   | 78 |  |
| R                                | efere   | nces  | 79 |  |
| A                                | Acknowledgements8   |   |    |  |
| Α                                | Appendix: Additional heat stress trial data (February 2018)83 |   |    |  |
|                                  | -   | · · · · · · · · · · · · · · · · · · ·                       |    |  |

### **Abstract**

This project developed and demonstrated technology to measure and map whole vineyard microclimate at a sub-metre scale in 3D using atmospheric acoustic tomography (AAT) coupled with long wave infrared thermography. The AAT system was based on a commercially available unmanned aerial vehicle (UAV) fitted with sensors that measure the sound of the UAV as it flies autonomously over the vineyard. A two-dimensional array of microphones deployed throughout the vineyard also measure the sound generated by the UAV as it flies. Accurate, 3D, concurrent, continuous observation and visualisation of air, vine and ground temperatures, and wind speeds across vineyard blocks of around 10Ha is now possible. High-resolution plant and heat stress factors and thermal maps of frost patterns can thus be derived as a function of geographic and temporal variation across a vineyard.

## **Executive Summary**

This report represents the final submission to Wine Australia for the project entitled, "Use of Unmanned Air Vehicles for Early Detection of Extreme Weather Events in Vineyards". The project was co-funded by Wine Australia and the Australian Government Department of Agriculture, Water and Environment as part of its Rural R&D for Profit program.

The project, which had a strong technology focus, has resulted in the developed of a transportable, unmanned aerial vehicle (UAV)-based meteorological monitoring capability for observing frost and heat-prone vineyards with high accuracy and at unprecedented levels of resolution. The technology is designed to measure microclimates across a vineyard block over a growing season, or even multiple seasons, which would assist vineyard management decisions for protecting against crop damage resulting from weather- related stress.

The research allows users to accurately estimate and visualise microclimates across vineyard blocks in 3D, permitting computation of plant stress factors like evapotranspiration (ET) and crop water stress index (CWSI). Using such parameters, users can now assess differences in microclimatic conditions within a region or vineyard and optimise irrigation, which is normally applied uniformly across a block. This would deliver water and energy savings.

Similarly, during frost events the technology can provide high resolution thermal maps of the surface and air temperatures surrounding the vineyards as a function of geographic and temporal variation. This permits evaluation of the effectiveness and/or need for different frost mitigation strategies, such as frost fans or sprinklers. As the technology is still in its infancy, the full value of the microclimatic information it offers is still being assessed. However, initial conclusions suggest frost mitigation strategies based on air temperature measurements alone may be sub-optimal.

In addition to the design and development of the technology and lessons learnt therein, several heat and frost stress events were observed and continue to be examined. Feedback from these analyses informed the technology's potential application space and commercialisation considerations. However, the project would benefit from more analysis of the data sets acquired: this will be an ongoing task

The technology is based on a commercially available Matrice 600 unmanned aerial vehicle (UAV) that was fitted with acoustic sensors that measured the pressure field (noise) generated by the UAV as it flew autonomously. Micro-sensors capable of synchronously recording meteorological variables such as wind velocity, temperature, pressure, and relative humidity were also fitted to this UAV. Two-dimensional arrays of microphones were deployed across two 10Ha vineyards: one at Wynn's, Coonawarra, the other at Jacob's Creek in the Barossa Valley. Each ground sensor also synchronously measured the pressure field generated by the UAV and matched them to those measured onboard the aircraft. From the correspondence relationships variations in sound speed for the signals propagating between the UAV and the ground sensors were computed as the aircraft overflew the vineyards. Using a technique commonly used in medicine, archaeology, and remote sensing known as tomography—which determines the inner properties of the observed medium—temperature and wind velocity profiles above and surrounding the vineyards were then computed in 3D.

In conjunction with this UAV, a second Matrice 600, equipped with a camera capable of high spatial and temporal resolution thermal imagery, was also flown over the vineyards, and the temperatures of the ground and vines calculated from the long wave infrared (LWIR) measurements. A technique known as structure from motion (SfM) was applied to the LWIR images to create 3D thermal point clouds of the vineyard. Finally, the 3D thermographic measurements were fused with the 3D tomographic information and the micro-climates around the vineyard visualised at unprecedented levels of accuracy and resolution. Several severe frost and heat events were observed.

Furthermore, using the thermographic and tomographic data, together with estimates of solar irradiance and object emissivity (obtained during the LWIR sensing operations), evapotranspiration levels and crop water stress indices were computed as a spatial function of vineyard geography over a day. The technology also enabled visualisation of the impact of devices such as frost fans and irrigation strategies. Ultimately automatic dissemination of information gathered using this technology in near real time would enable growers to respond more quickly, cost-effectively, and precisely to severe weather events, which will become increasingly common through climate change.

In addition to the above, a technique for identifying and classifying vine properties such as row width, height, cover-fraction, and missing segments was developed. The genesis of this algorithm was as a bi- product of the need for the tomographic-thermographic data fusion routines to uniquely identify the thermographic (LWIR radiation) properties of the vineyard, i.e. the need to automatically separate vines from inter-row material as they have different emissivity. The algorithm offers users the ability to rapidly, efficiently and non-destructively visualise plant vigour as a spatial function of vineyard geography: the information may be integrated into decision support tools to improve management practices.

The algorithm uses a sequence of overlapping aerial images obtained from visible and long wave infrared cameras carried by the UAV and SfM to extract the underlying topography of the surface terrain. The 3D point clouds were then classified in terms of their hue, saturation, surface temperature and height relative to this surface topography, and the vine and inter-vine material discriminated from one another. The accuracy of the algorithm in terms of its ability to identify vine properties was evaluated using field measurements and was shown to be very effective.

#### Structure of this report

Section 1 of the report provides the project objectives and Section 2 the basic technology concepts, together with the hardware and software builds. Section 3 outlines the campaign of field deployments and some preliminary conclusions drawn from these observations. Section 4 describes the algorithm for identifying and classifying vine properties such as row width, height, cover-fraction, and missing segments. The report concludes with a summary of the project and a description of future potential research.

#### **Participants**

The project assembled an experienced, multi-disciplinary team from the wine industry, academia, UAV specialists, and meteorologists, including Dr Michael McCarthy (South Australian Research and Development Institute), Dr Catherine Kidman (Wynn's Coonawarra Estate), Tim McCarthy (Treasury Wine Estates), Pernod Ricard Winemakers, Dr Greg Holland (US National Center for Atmospheric Research), Peter Smith (Barton Vale Technologies), and Professor Anthony Finn (University of South Australia).

## 1 Project rationale and objectives

Many factors affect grapevine productivity: climate, weather, soil properties, topography, grape variety, management practices, and pests and diseases, with spatial variations of such factors within and between vineyards impacting both grape quality and yield. Optimal management practices are highly desirable, with decisions depending upon precise situational awareness of crop state ideally based on information gathered safely, efficiently, and non-destructively. Such tools allow the Australian wine and grape industry to face its fierce global competition in the marketplace and allow the sector to improve competitiveness through technology developments that deliver productivity gains.

In this context, remote sensing offers considerable opportunities, with visible (VIS), long wave infrared (LWIR) and near infrared (NIR) hyperspectral sensors all providing windows into the complex surface chemistry present in vineyards. Although potentially promising, satellite-based observations are not routinely exploited: imagery from several satellite systems is commercially available, but the spatial resolution of their VIS and LWIR sensors (5-30m) is generally inadequate for mapping small vineyards [1]. Moreover, the superposition of signal returns from vines and inter-row material within a single pixel makes extraction of desired signatures difficult. Row structure and topography of underlying terrain must also be accounted for to avoid introduction of effects that depend upon the directionality of observations or signal reflectance [2-6]. Higher spatial resolution sensors (5-20cm) are therefore essential if the properties of inter-row returns are not to contaminate vine signatures, which are of prime importance to any decision support tool. Furthermore, satellite orbital characteristics, together with sensor pose, drive temporal availability of such data sets, as does the prevalence of cloud cover.

Alternative, more operationally flexible remote sensing options, such as aircraft and Unmanned Aerial Vehicles (UAVs), are also available; and—relative to their satellite counterparts—the proximity of such platforms to vines intrinsically improves the ground resolution of the sensors carried. Although operation of such platforms is generally weather-dependent, planning flights close to particular stages of plant development is straightforward and several authors have examined mapping crop vigour using such techniques [7-10]. In the past few years increased availability of UAVs has also added new opportunities to acquisition of high spatial resolution imagery. As a result, there have been many studies into the acquisition and exploitation of multi- or hyperspectral data sets to assess vine vigour [11-14], grape species [15, 16], and water and nitrogen stress [12, 17] against vegetation indices, such as the normalised difference vegetation index [18].

The technology developed under this program offers growers knowledge of vineyard microclimates at the

micro-scale. The impact of extreme weather on vines and fruit is well-known. Variability in vineyard micro-climate produces variability in grape quality and production, which influences economic risk for several wine growing regions. There is a particularly strong relationship between grapevine yield, wine quality and extreme weather, the effects of which are well-known. The synoptic conditions that lead up to such events are also easily recognised: forecasters are seldom surprised. However, the duration of such weather events, exactly where frost events occur, precisely how hot it is within individual vineyards and under canopies and what the impact is on individual plants within a vineyard are all much harder to predict and monitor. Moreover, in the longer term, climate change will lead to growth in extreme weather events.

Several protection methods are available to wine growers for combating extreme weather conditions, including private forecasting services at the micro-scale. However, such empirical forecasts typically rely upon a few point source measurements and projections updated from synoptic and mesoscale models that themselves rely upon data taken tens of kilometres from wine growing regions (and which are several hours old). There is a need for growers to know vine and fruit temperatures at the micro-scale with great precision and in near real time.

The approach described here delivers a combination of vine, foliage, ground, and air temperatures and wind speed observations at the micro-scale (sub-metre). These are estimated to be accurate to within 0.2°C and 0.3m/s, respectively. The technology is based on small, man-portable unmanned aerial vehicles (UAVs) that undertake autonomous flights vineyards.

## 2 Technology concepts and components

#### 2.1 Acoustic Atmospheric Tomography

Details of the technique are available in [19-26] and summarised below. A 2D array of microphones is deployed across a 10Ha vineyard and the sound fields at each sensor measured synchronously ( $\leq$  100µs) with that generated by a UAV as it overflies the perimeter of the sensor array/vineyard. Careful correspondence of these two sets of observations allows sound speeds for signals propagating between the UAV and microphones to be calculated. As the location of the UAV and ground microphones are known accurately ( $\leq$  0.05m), ray path geometry may be computed, and a technique known as *tomography* applied. Tomography—which is used extensively in medicine, archaeology, and remote sensing—uses the geometry of emitters (UAV locations over time) and receivers (microphones) to determine the properties of the observed medium from the intersection of measurements taken passing through it. A depiction of the concept in 2D is shown in Figure 1. The relationship between sound speed, air temperature, and wind velocity, then allows profiles of the atmosphere to be computed and visualised for the vineyard environment. For a one-dimensional array of microphones, a 2D atmospheric profile is obtained; and for a 2D array of microphones a 3D profile is obtained.

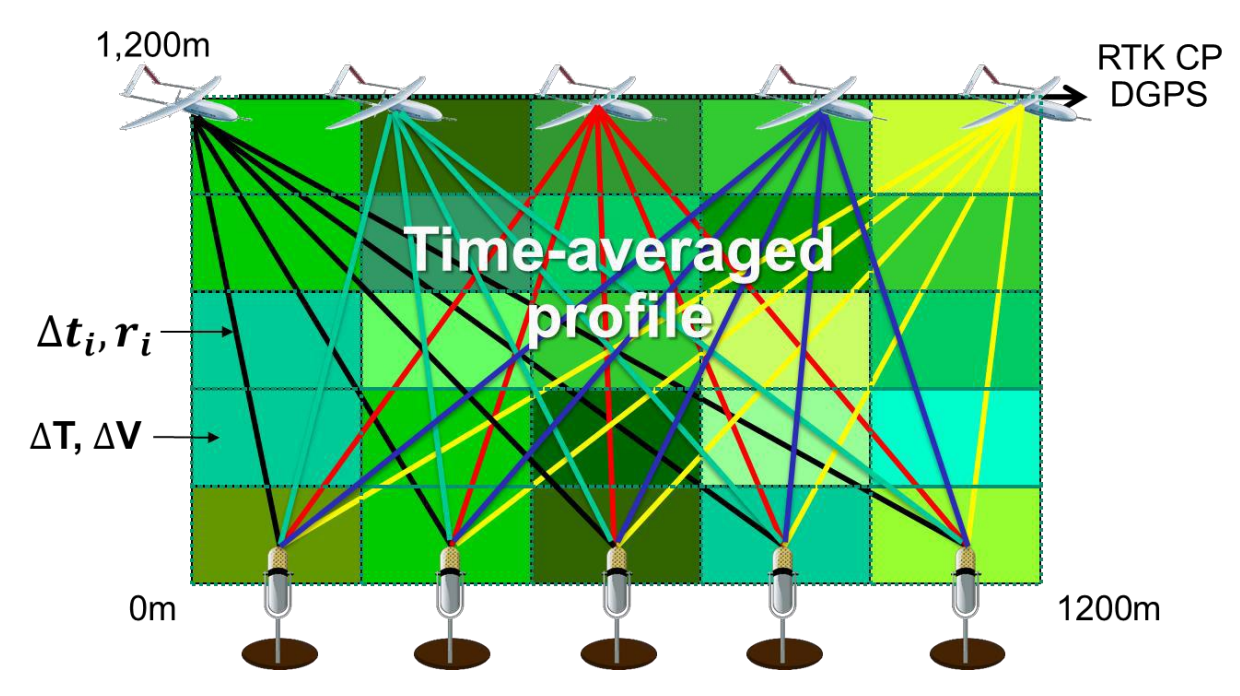


Figure 1: Graphical depiction of acoustic atmospheric tomography. As the UAV overflies an array microphones on the ground, the propagation delay,  $\Delta t_i$ , for the i<sup>th</sup> ray (of length  $r_i$ ) may be computed from the correspondence of the sound fields measured synchronously by them and a microphone onboard the UAV. The intersection of the rays allows 'elements' of the atmosphere to have their temperature (T) and wind velocities (V) computed. In fact, the differences in temperature and wind ( $\Delta T$  and  $\Delta V$ , respectively) relative to a nominal value are computed.

#### 2.2 LWIR Thermography

A second UAV, equipped with a camera capable of high-resolution thermal imagery, is also flown over the vineyards to obtain ground and vine temperatures based on the long wave infrared (LWIR) irradiance measurements. Unfortunately, as not all the radiation received by the LWIR camera derives from the target object, to measure vine temperature accurately radiation from surrounding objects must be accounted for in the temperature calculations. The total radiation,  $I_{tot}$ , received by the LWIR camera derives from several sources (Figure 2): radiation from the object of interest (e.g. vines), plus radiation from the surroundings (e.g. the ground) reflected onto the object's surface, less the attenuation suffered by both components as they pass through the atmosphere, plus radiation received directly from the atmosphere.

Knowledge of an object's emissivity,  $\varepsilon_{obj}$ , (and hence reflectivity = 1 – emissivity), temperature of the atmosphere,  $T_{atm}$ , and environment,  $T_{refl}$ , and atmospheric transmittance,  $\tau_{atm}$ , allows these factors to be accounted for and the temperature of the object,  $T_{obj}$ , to be computed. Mathematical details of precisely how this is achieved are available in [27], but essentially the temperature of an object may be computed using

$$T_{obj} = \sqrt[4]{I_{tot} - \left(1 - \varepsilon_{obj}\right) \cdot \tau_{atm} \cdot \sigma \cdot T_{refl}^4 - \left(1 - \tau_{atm}\right) \cdot \sigma \cdot T_{atm}^4} \tag{1}$$

Where  $\sigma \approx 5.67 \times 10^{-8} \text{Wm}^{-2} \text{K}^{-4}$  is the Stefan-Boltzmann constant and all temperatures are in Kelvin.

The most important calibration parameter for field temperature measurement using thermography is emissivity as this indicates how much radiation is emitted from the target object when compared to that from a black body of the same temperature. In objects with high emissivity, such as plants, slight variations in the computed emissivity value cause only minor changes in the resulting surface temperatures. However, for lower emissivity objects such as reflective surfaces, small errors in emissivity measurement can cause significant variation in derived temperature estimates.

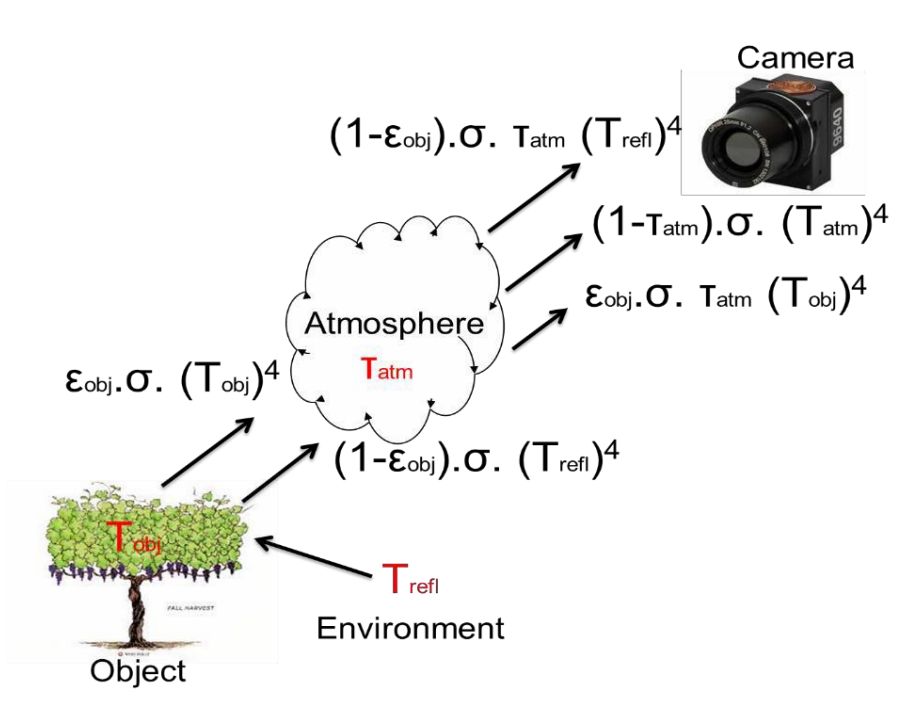


Figure 2: Radiation components observed by long wave infrared camera

As a result, during the UAV flights temperature monitoring devices were placed around the vineyard under (to protect them from the radiative effects of the sun) boards of known emissivity. One board had an emissivity of 0.95, the other 0.03 (images of these boards are shown in Figure 3). Based on the known temperature of the high emissivity boards, any discrepancy in temperature observed thermographically may be adjusted so that more accurate real temperatures of the objects in the environment can then be calculated.

Although not as important in frost conditions (because vineyards predominantly comprise high emissivity plant material), measurement of reflected temperature is also important, especially when reflectivity of an object is high, e.g. when there is dry soil uncovered by plant material (as per heat stress conditions). In this project reflector boards covered with crumpled pieces of aluminium foil were placed next to the high emissivity boards and the temperature of the reflector measured thermographically. The temperature of this board was then computed (using Equation (1)) assuming an emissivity of one and no atmospheric loss; and the computation is then repeated—again using Equation (1)—using the previously computed temperature of the reflector board as the reflected temperature. The resulting temperature is the final reflected temperature,  $T_{refl}$ .

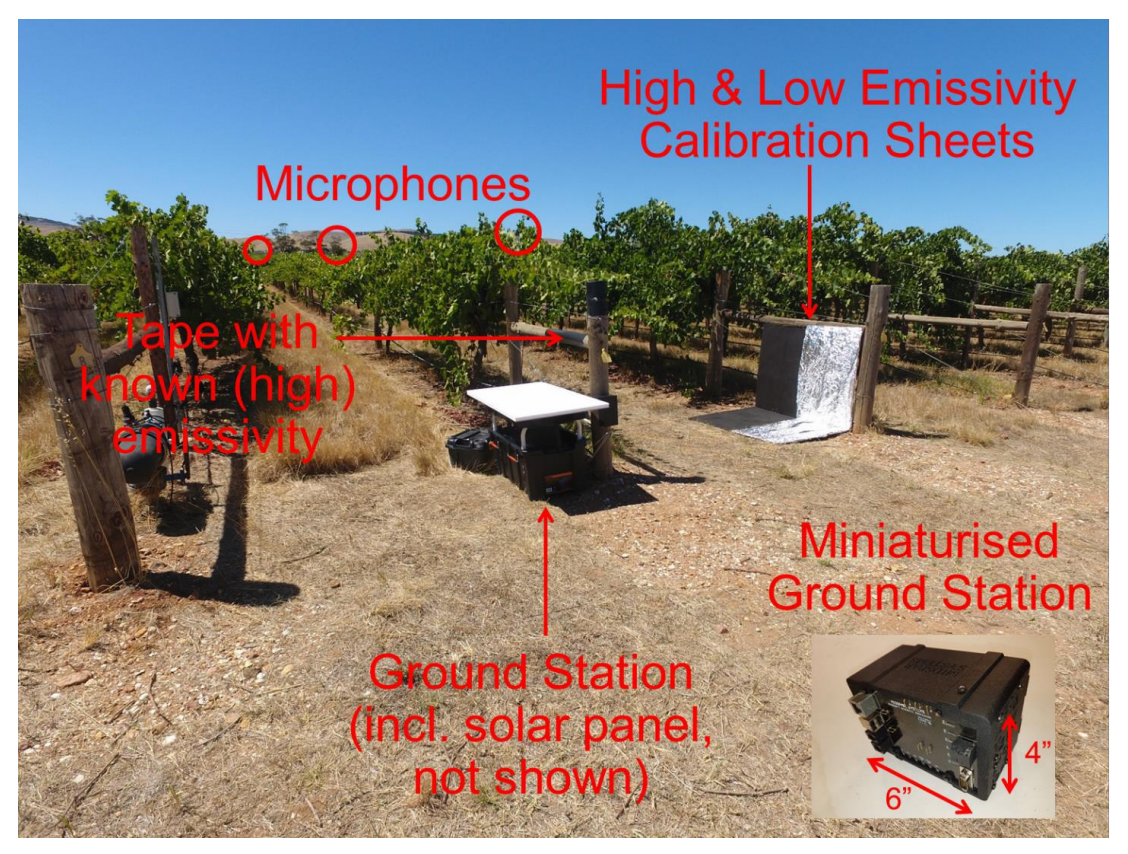


Figure 3: Ground station setup in vineyard, showing microphones (50m apart), and thermographic calibration boards

The thermographic and tomographic data are then fused with other meteorological and solar load data so that micro-climates around and within the vineyard can be obtained at sub-metre levels of accuracy and resolution. Both frost and heat events have been successfully observed during this project.

#### 2.3 Structure from motion

Structure from motion (SfM) is the process of estimating the 3-D structure of a scene from a set of 2D images. It is used in many applications, such as robot navigation, autonomous driving, and augmented reality. SfM has been extensively described in the literature [28-30]<sup>1</sup>. The process consists of two main components: camera motion estimation and DPC reconstruction. Initially, a sparse set of points are matched across the image stack to find correspondences. Such features are typically extracted using algorithms like SIFT (scale invariant feature transformation) [31] and SURF (speeded up robust features) [32]. The sequence of views is then iteratively processed to track a denser set of points across the views so that the pose of the camera can be established for each image set and—after the relevant coordinate transforms have been accommodated—a dense 3D reconstruction of the scene made. The process of estimating camera motion (and hence DPC) is generally improved if camera pose is recorded during image capture and applied during SfM computations, which in our case it was not. If a suitable selection of ground control points (GCP) are applied to the resulting DPC, absolute scale and orientation may also be determined. This was achieved through matching the reconstructed DPC to a Google Earth view of the same area.

-

<sup>&</sup>lt;sup>1</sup> In order to carry out the SfM computations we have used proprietary software (written by UniSA in MATLAB), as well as MetaShape (previously known as Agisoft Photoscan) and Reality Capture.

## 2.4 Multi-UAV Acoustic Tomography<sup>2</sup>

Despite its unprecedented capacity to observe vineyard microclimates, ground-based UAV AAT has some disadvantages. For example, as it compares the acoustic signature observed onboard the UAV with the Doppler-shifted sequence received by an array of ground-based microphones the technique loses accuracy at greater altitudes. The ground placement of microphones also imposes geometric restrictions on the tomography that reduces the achievable level of accuracy; and field deployments are very time-consuming. Small UAV's also have top speeds of around 20m/s, so the atmosphere changes during the observation period and the resulting inversion therefore represents only a time-averaged sample of the atmosphere, not a crisp snapshot.

We therefore examined the feasibility of an AAT technique that uses two or more UAVs. The technique permits faster observations, and hence less time-averaging of the atmosphere. It also offers even higher levels of user-control and mobility than the ground-based AAT. Most importantly, the technique allows simultaneous reciprocal time delay measurements to be observed along near-identical ray paths. As this is analogous to a sonic anemometer the influence of wind on the sound speed can be eliminated, enhancing the accuracy of the inversion.

Furthermore, despite the low viscosity of air and rapid changes over small distances and time scales, the possibility of identifying energy harvesting opportunities for fixed wing UAV flight exists. To date this has only been possible based only on onboard sensors that rely upon the direct effects of the motion of the air on the UAV, i.e. using parameters such airspeed, altitude and throttle settings. In other words, the distribution and motion of atmospheric gradients inferred or learnt from multi-UAV AAT can be exploited by allowing the UAVs to perform static or dynamic soaring manoeuvres [33, 34]. The mathematical details of multi-UAV AAT are more complex that single-UAV AAT and are contained in [22].

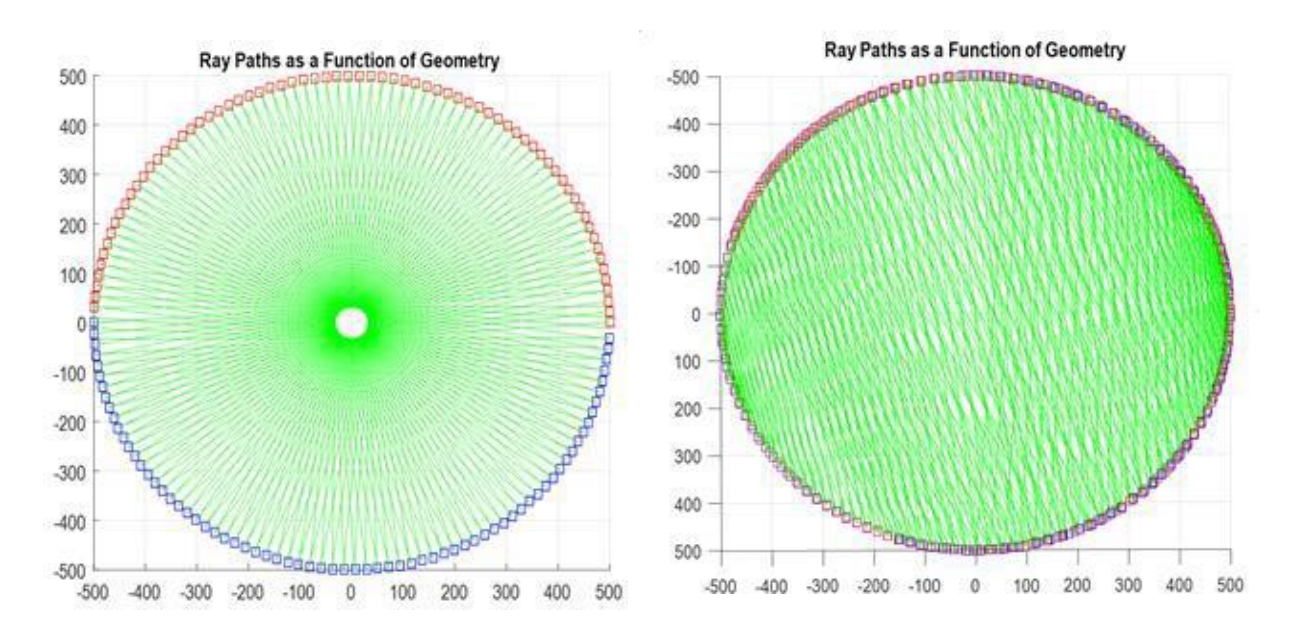


Figure 4: Ray paths vs. angle for: (left) UAVs flying similar velocities and 'chasing each other's tail, and (right) UAV1and UAV2 flying velocities in opposite directions that vary sinusoidally.

12

<sup>&</sup>lt;sup>2</sup> The multi-UAV technology is not as robust or mature as the single-UAV approach, but it is more readily deployed.

Essentially, multi-UAV AAT works in the same way as a giant (multi-UAV based) sonic anemometer. Signals are emitted and received by the UAVs and signal processing techniques applied to obtain the propagation delays at sub-millisecond levels of accuracy. Knowing the locations of the UAVs at every epoch to within ±0.03m the time delays may be corresponded to geometry, sound speed, and hence temperature and wind velocity. As velocity field errors tend to grow in the direction perpendicular to individual rays, however, the relative flight paths of each UAV are important.

For example, if both UAVs fly clockwise circular paths with the same velocity, starting 180° out of phase, the ray paths—which propagate in both directions—will intersect like 'spokes in a wheel' (Figure 4, left). Moreover, the rays will not pass through the centre of the circle, as the receiving UAV moves during signal propagation; and they will only intersect at shallow angles at the outer elements of the circle. Whilst this makes the bi-directional resolution of the wind vector component simpler, it also makes the inversion problem sparse and ill-posed; and effectively precludes decoupling the combined effects of temperature and wind on sound speed.

#### 2.5 Equipment Details

The various hardware builds required for this project are described in this section.

Thermographic Payload: This comprises a gimbal-mounted ICI 8640P long wave infrared (LWIR) thermal imaging camera, which has a 640 x 480 14-bit Vanadium Oxide radiometric imager. This sensor has an update rate of 10fps and accuracy of 1°C. This payload also carries an Odroid digital camera with a 35mm lens. Both sensors had roughly 60° fields of view, providing a ground resolution of approximately 10cm or better. At the 10m/s forward velocity and 120m altitude typically used during trials, this provides about 85% and 50% overlap between images in the along- and across-track directions, respectively. This is allowed efficient coverage of a roughly 10Ha vineyard in about 3-5 minutes, depending upon prevailing weather conditions. The results are shown in Figure 5 and Figure 6.

The UAV/payload was flown over the vineyards in a sequence of opposing parallel lines, oriented along vine row direction, at constant forward horizontal velocity and altitude. This pattern, colloquially known as a 'lawn mower', is shown in Figure 7 as set of continuous white lines. The image shows the orthomosaic projection of the visible images obtained from the Odroid camera superimposed onto a Google Earth rendition of trial site at Jacobs Creek, Barossa Valley.

Initially, a bespoke 1.4kg UAV was built to carry the payload. When the payload was used in conjunction with this UAV, the platform position was determined using standard positioning service GPS (horizontal accuracy 3-5m), with altitude maintained using barometric pressure. Separation between each parallel path was about 70m. During the life of the project, however, a second Matrice 600 was procured by UniSA under another project and the payload carried by this UAV as more accurate GPS positioning is available to the larger UAV.

Several UAV-SfM integrated/automated flight path planners exist for managing the payload's image acquisition strategies. However, because the image sequences of vineyards are highly repetitive and the lighting conditions can vary between image sets, images were collected at a rate of 10Hz. This provided the optimal trade-off between rapid/efficient coverage of the vineyard and recreation of 3D structure from motion from the constrained geometry. The overarching goal for the flight path strategy was to avoid the need for potential users to become expert in the design of UAV flight paths and SfM operations. Thus, the trials also demonstrated the algorithm's robustness against imperfectly acquired real world data sets, and its insensitivity to noisy, imperfect and uneven performance of SfM.

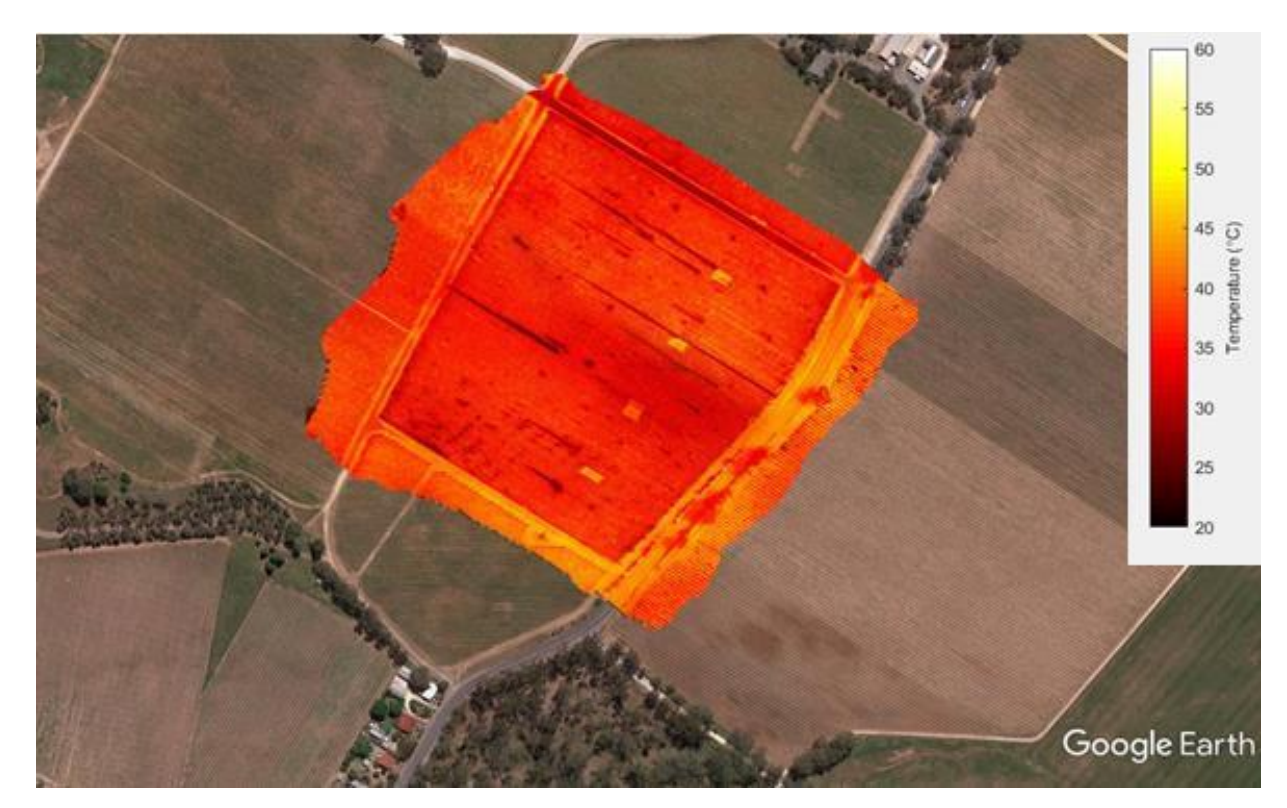


**Figure 5:** Orthomosaic view of the dense point cloud generated from LWIR thermal imaging camera superimposed onto a Google Earth extract of the Jacobs Creek site. The DPC is colour-coded according to the temperature scale on the right

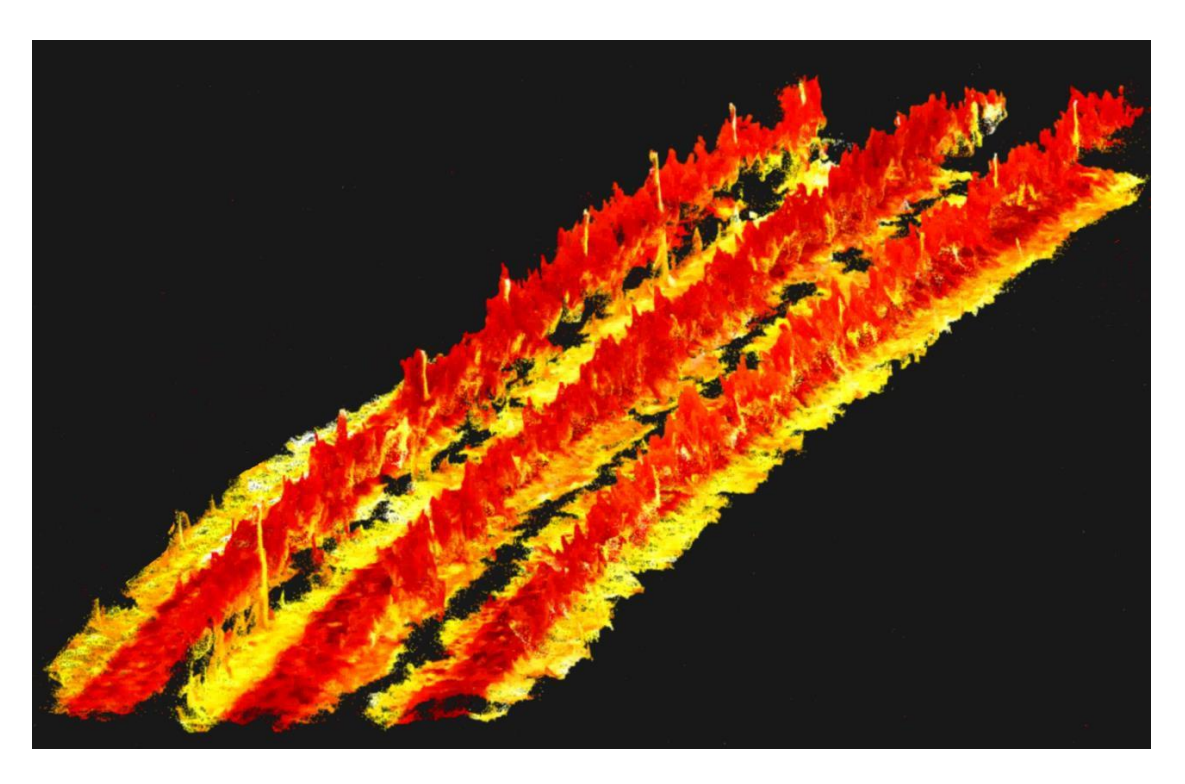


Figure 6: Close up 3D temperature map of vines taken in Spring using the UAV-borne thermal imaging sensor



**Figure 7:** Orthomosaic view of the VIS dense point cloud superimposed onto a Google Earth extract of the Jacobs Creek site at 34° 34′ 04″ South, 138° 56′ 00″ East. The white lines depict the approximate 'lawn mower' flight.

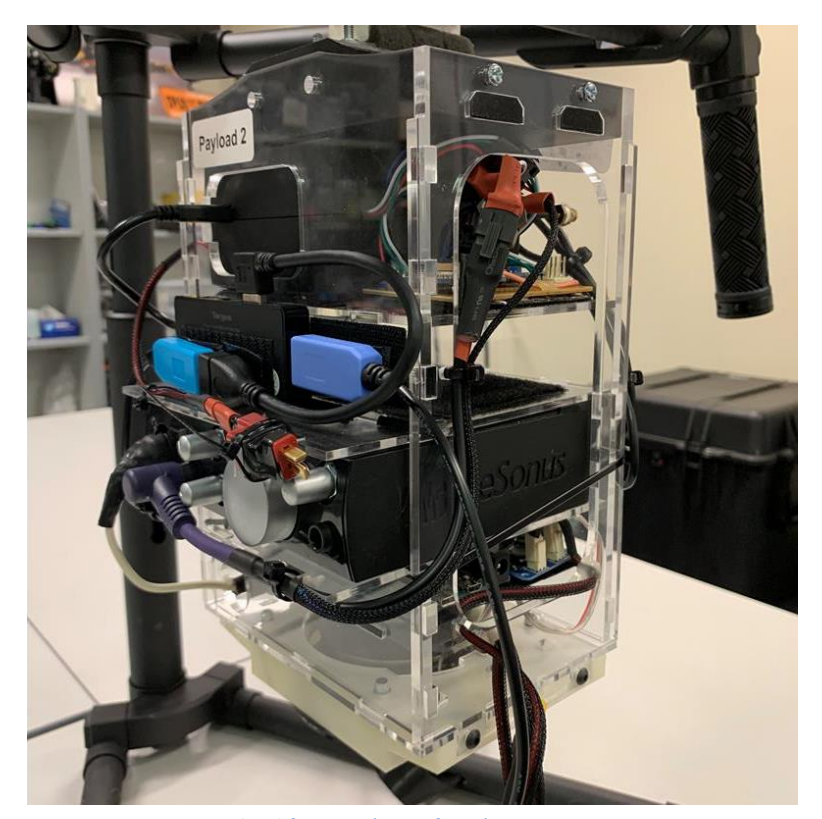


Figure 8: Acoustic payload for UAV (one of two)

**AAT Drone & Payloads:** A Matrice 600 UAV was modified to carry a payload designed and built under the project. The payload can simultaneously sample an ECM800 10mV/Pa condenser microphone at 44.1kHz and an accurate timing signal generated by the one pulse per second (1PPS) of a global positioning system

(GPS) receiver. The payload can also generate an acoustic signal (any pulsed or continuous spectral configuration), which can be detected at ranges in excess of 2km. Similarly, the payload continuously monitors UAV location and orientation (at a rate of 50Hz) and wind velocity measured onboard the UAV during motion (at a rate of 1Hz). The payload can operate under severe weather conditions ( $-5^{\circ}C - 50^{\circ}C$ ).

**Ground Stations:** 7 ground stations (Figure 9) were designed and built. Each unit comprises an 8-channel, 24-bit Data Acquisition (DAQ) recorder with 107dB spurious free dynamic range capable of simultaneously sampling 7 ECM800 10mV/Pa condenser microphones at 44.1kHz. Accurate time stamping of the data is obtained by the first channel of the DAQ also sampling a GPS-derived 1PPS edge. Each ground station is contained within a weatherproof box and can operate under unattended in extreme weather conditions (-5°C – 50°C), is battery/solar powered (and thus deployable for extended periods). The full set of seven ground stations can be operated remotely from a single computer in the field or over the internet.

**Meteorological micro-drone:** Micro meteorological sensors were integrated onto a Phantom IV UAV (Figure 10) to measure pressure, temperature, relative humidity, and location at a rate of 1Hz. Barometric pressure was used (in conjunction with a third, ground-based iMet-XQ sensor) to accurately determine sensor altitude to within ±0.5m as the vertical component of SPS GPS is generally accurate only to about ±20m. Thermodynamic temperature was converted to virtual temperature based on measurements taken onboard the UAV. Based on laboratory tests, the temperature sensor is accurate to within ±0.3°C.



**Figure 9:** Ground station (one of seven), comprising a laptop that manages and records data from an 8-channel, 24-bit DAQ with 107dB spurious free dynamic range. 7 channels sample ECM800 10mV/Pa condenser microphones at 44.1kHz. Accurate time timing is maintained by sampling the GPS-derived 1PPS edge on the 8<sup>th</sup> channel.



Figure 10: Meteorological sensors mounted above and below a Phantom IV UAV. They are placed above and within the airstream generated by the UAV's propellers to capture meteorological measurements. The meteorological sensors can measure pressure  $(\pm 1.5 \text{hPa})$ , temperature  $(\pm 0.3^{\circ}\text{C})$ , relative humidity  $(\pm 5\%)$ , and location  $(\pm 5m)$  simultaneously at a rate of 1Hz (note: the UAV's propeller blades are removed as a safety precaution while it is in the laboratory).

# 3 Field deployments and assessment

The reporting on the campaign of field deployments is split into three sub-sections: accuracy assessment, followed by observation of heat stress and frost events.

#### 3.1 Performance assessment: simulation

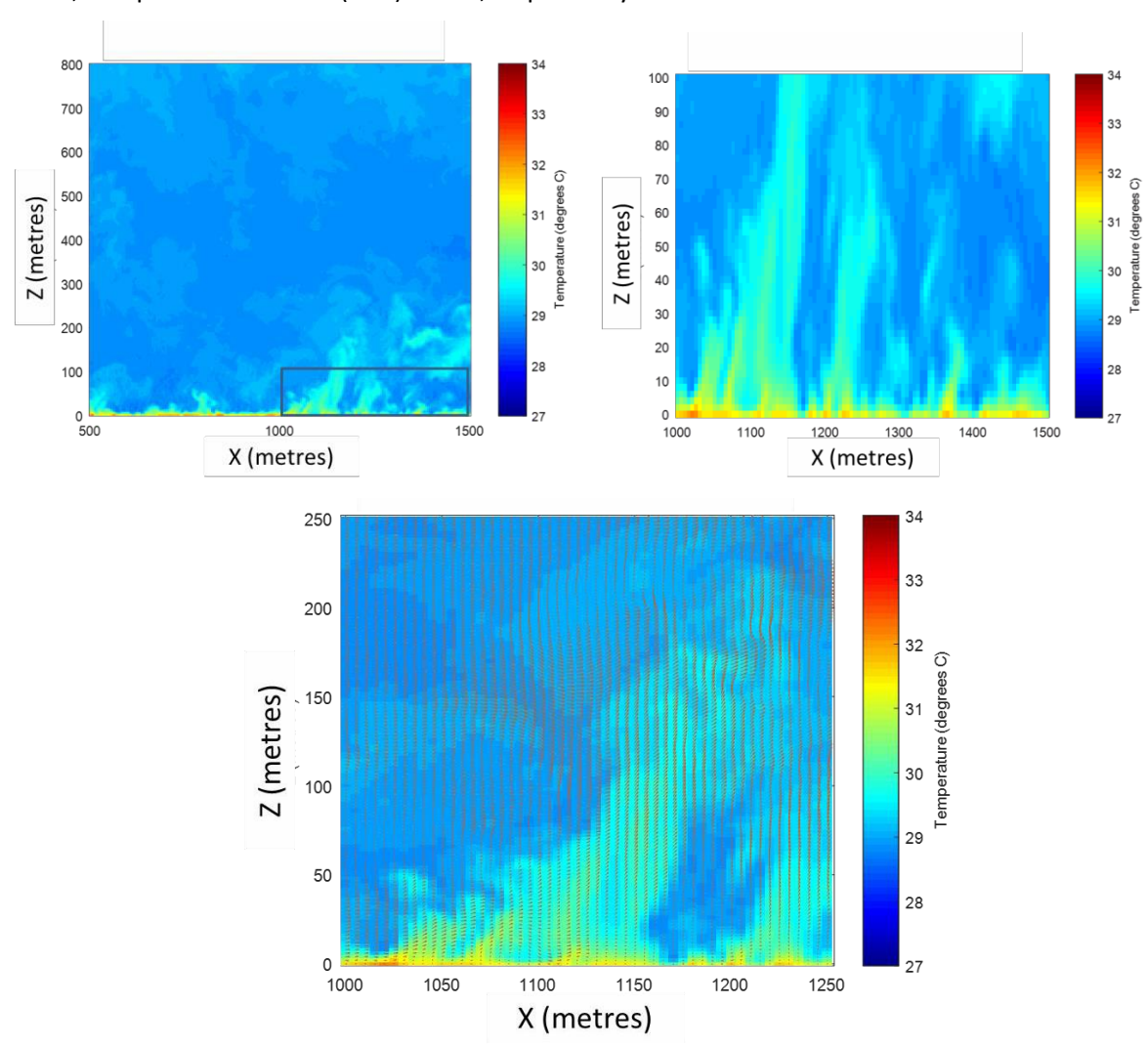
**Single UAV-Based AAT:** During the equipment construction phase of the project (year one), the focus the anticipated performance of UAV-based AAT was examined using synthetic 2D atmospheres based on Large Eddy Simulation (LES). Sullivan and Patton [35] generated a suite of atmospheric simulations for a canonical daytime convective planetary boundary layer (PBL) using large eddy simulation (LES). The volume of atmosphere represented in their simulations comprises a uniform grid mesh of 1,024<sup>3</sup> points in a 5,120m x 5,120m (horizontal) x 2,048m (vertical) volume. The simulations are carried forward in time for about 38 minutes, so the data set provides temperature and wind velocity at each point in the 3D space-time lattice. The parameters used to simulate this weakly sheared daytime convective PBL are contained in Sullivan and Patton [35].

Figure 11 (upper left) shows a vertical cross-section of temperature through the LES data set typical of that used in the analysis. Figure 11 (upper right) shows an expanded section of the image on the left. The lower figure shows a similar image (also expanded from that shown upper left) with wind velocity overlayed. Arrows point in the direction of the wind with lengths scaled according to speed (the largest represents the maximum wind speed, 2.8 m/s).

The AAT scenarios used a simulated linear array of microphones located over baselines ranging from 100m to 3,000m, with a range of sensor separations were use. At least 10 ground sensors covered any baseline. Although LES allows simulation of time-varying atmospheres, wind and temperature profiles were assumed to be frozen over the observation period. The  $100 \text{ m} \times 100 \text{ m}$  simulations were used to examine the extent

to which scale sizes at the resolution of the LES data set (2-5m) could be faithfully reproduced. Larger simulations (1,000 m and 3,000 m baselines by 1,000 m altitude) were used to examine the extent to which this fine-grain information could be extracted from larger scenarios more in keeping with the target application.

Rays were propagated through the known vertical profile of wind and the propagation delays determined by numerically integrating along the straight-line path between the start and end of each ray. The integration steps were aligned with the cell size of the LES data. The RBF were located within a uniform 100 m x 100 m grid. Representative propagation errors were superimposed onto the 'true' time delay value for each ray generated for the aircraft-ground sensor array geometries. The errors were applied as a bias (calculated as a percentage of propagation delay), a random component (represented by additive Gaussian white noise and applied around the bias) applied to each time delay, and a random component (represented by additive Gaussian white noise) applied to all locations. These errors represent propagation errors, signal processing errors, and position-location (GPS) errors, respectively.



**Figure 11:** Cross-sections of atmospheric profiles generated by Sullivan and Patton [35]. The upper right figure is an expanded section of that shown in the upper left. The lower figure shows temperature (colour coded as per the colour bar on the right hand side) and wind velocity (shown as arrows).

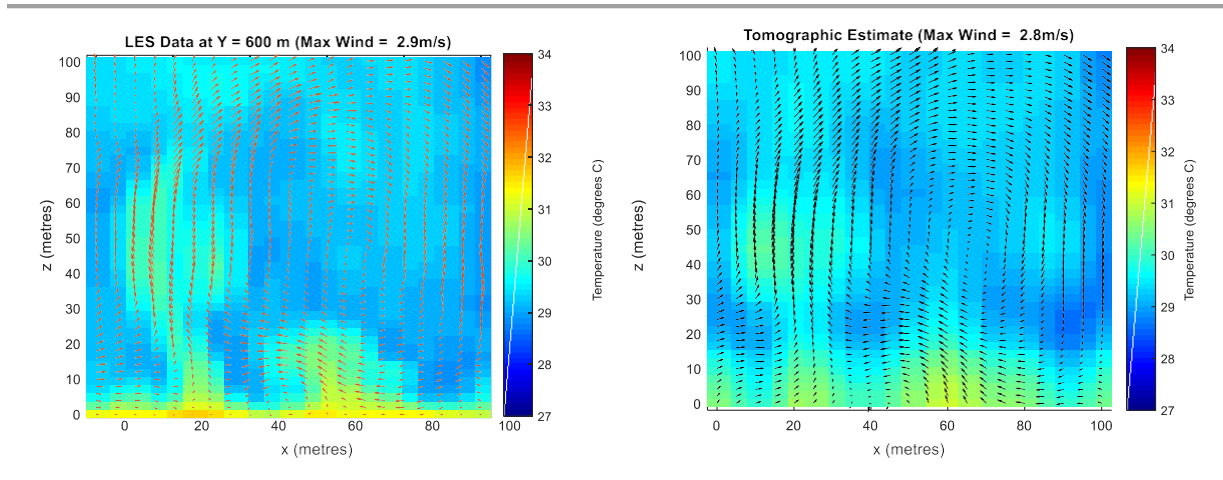
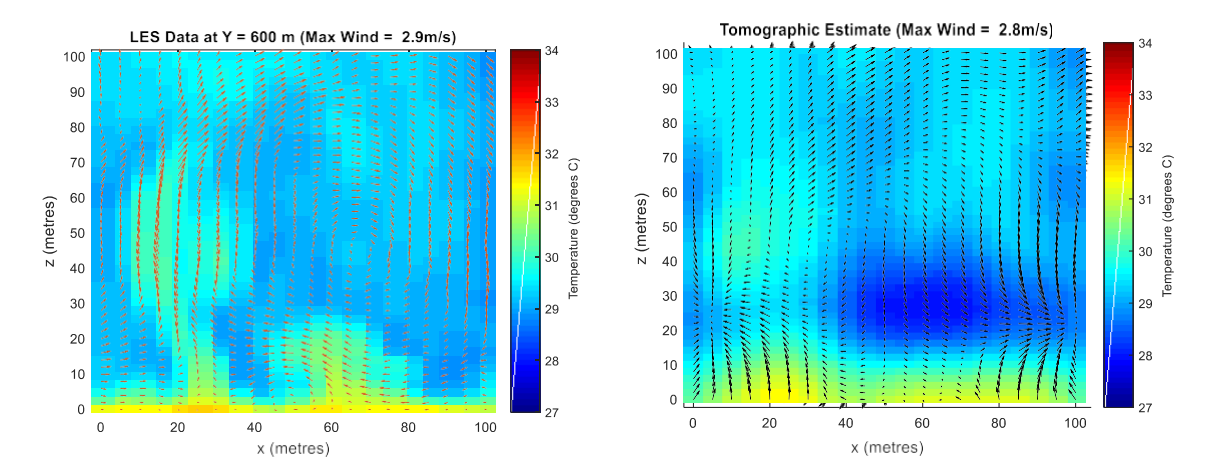


Figure 12: Target temperature and wind profiles (left) and those estimated using tomography (right). Errors due to signal processing and ray path propagation are 0.1ms and 0.01%, respectively.

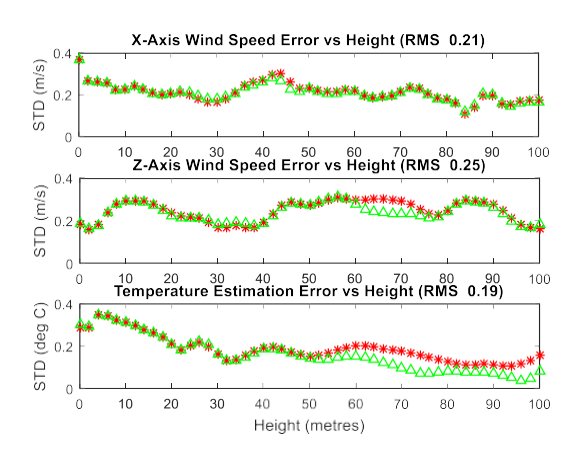


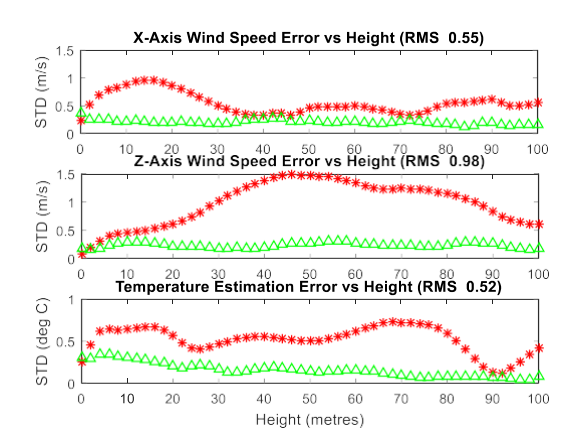
**Figure 13:** Target temperature and wind profiles (left) and those estimated using tomography (right). Errors due to signal processing and ray path propagation are 1ms and 0.1%, respectively.

Figure 12 shows comparisons between target and tomographic estimates of temperature and wind profiles derived using the error regimes of 0.1ms for signal processing, 0.1% ray path length, and 0.1m for GPS. Ground sensors were spaced at 10m intervals. Simulations for the target atmosphere (left) and reconstructions based on signal processing and ray path errors of 1ms and 0.5% (right) are shown in Figure

13. The higher errors produce significantly poorer estimates of the temperature and wind profiles and indicate the upper limit for tolerable observation noise for the technique.

The error plots for both Figure 12 and Figure 13 are shown in Figure 14. There are two components of error: direct and indirect. The direct error is the degree of mismatch between the target LES profiles and their replication using RBFs: the more RBFs used, the more faithfully the target data are replicated, and the lower the direct error. Ideally, massively dense RBF sets are used. However, the ill-posed and sparse nature of the inverse problem causes numerical instability in the matrix inversions. This forces a reduction in the number of RBF involved in the inversion, and hence its resolution.





**Figure 14:** Direct and indirect error plots for temperature and wind speed as a function of height. The figure on the left shows the error plots for measurement errors of 0.1ms and 0.1% path length, whereas the figure on the right shows temperature and wind speed errors for measurement errors of 1ms and 0.5% path length: red asterisks represent 'indirect' errors (estimates obtained from the tomographic inversion) and green triangles the results of directly fitting the same RBF lattice as used by the tomographic inversion directly to the LES data.

The indirect error is the accuracy with which the inversion can faithfully represent the 'best' RBF fit to the target data. In other words, it is possible to have substantial direct error but negligible indirect error if the original LES profiles are heavily spatially averaged through use of a small number of RBF. Thus, a key measure of success for the overall technique is given by comparison of the direct (red asterisks) and indirect errors (green triangles) as the link shows correspondence between the tomographic inversion and LES data at the same atmospheric scale size and RBF resolution (Figure 9).

To a first order the indirect error is governed by the number of RBFs (and hence separation distance between them)<sup>3</sup> While the Eikonal assumptions for propagation through such a medium would be questionable, for RBF separation distances < 1m temperature differences between the estimated and target atmospheres are negligible (< 0.01°C). If the RBF separation distance is increased to 10m (as per Figure 7) correspondence falls to about 0.2°C (1 $\sigma$ ). Pressure to increase separation distance between RBF (and hence reduce resolution and accuracy of the solution) is predominantly driven by the need to manage the number of degrees of freedom (DOF) in the inversion. Too many DOFs lead to numerical instabilities as errors in one (poorly observed) RBF coefficient typically propagate to others. This is because the inter- cellular relationship between coefficients is (at present) unconstrained.

**Multi-UAV Based AAT:** Two UAVs were 'flown' through the Sullivan and Patton LES data. The aircraft flew in opposite directions to one another at slightly different altitudes (to avoid collision). Their ray path intersection map is shown in the righthand image of Figure 4. The aircraft flight dynamics were not considered to be influenced by wind vectors or temperature variations and the structure of the atmosphere was assumed to be 'frozen' over the duration of the simulation.

The signal processing regime represented was based on that used during field trials reported elsewhere [36]: a 102 dB dynamic range, 44.1 kHz ADC on both UAVs, combined with a 2<sup>16</sup> point Fast Fourier Transform (FFT) with Welch averaging comprising four-times over-sampling and 50% overlap between

sample blocks. This represents ray paths to/from each UAV at 2 Hz and SNR commensurate with the experimental data reported in Rogers & Finn [36].

\_

<sup>&</sup>lt;sup>3</sup> The memory of the computer used to perform the inversion (an Intel® Core i7-5600U CPU@2.6GHz with 16 GB RAM) is also a factor as a more powerful machine would provide the capacity to process a denser ray set.

The UAV position and signal process errors were once again modelled by superimposing additive Gaussian white noise (AGWN) onto the locations of the aircraft and true propagation delays for each epoch. For position errors this was at levels commensurate with real time kinematic carrier phase Differential GPS,

i.e. 0.05 m. For the errors due to front end signal processing, the reduction in SNR due to wind noise and mutual interference from the UAV engine and ADC sampling rate jitter are modelled in accordance with levels derived in [21, 22], i.e. 0-10ms. Variations in the refractive index along the ray path were modelled by adding a percentage of the true delay in accordance with the benchmark regimes of an unstable atmospheric boundary layer suggested by Ostashev et al [37], i.e. 0.06%, 0.14%, and 0.67% for low, moderate and strong wind regimes, respectively [20].

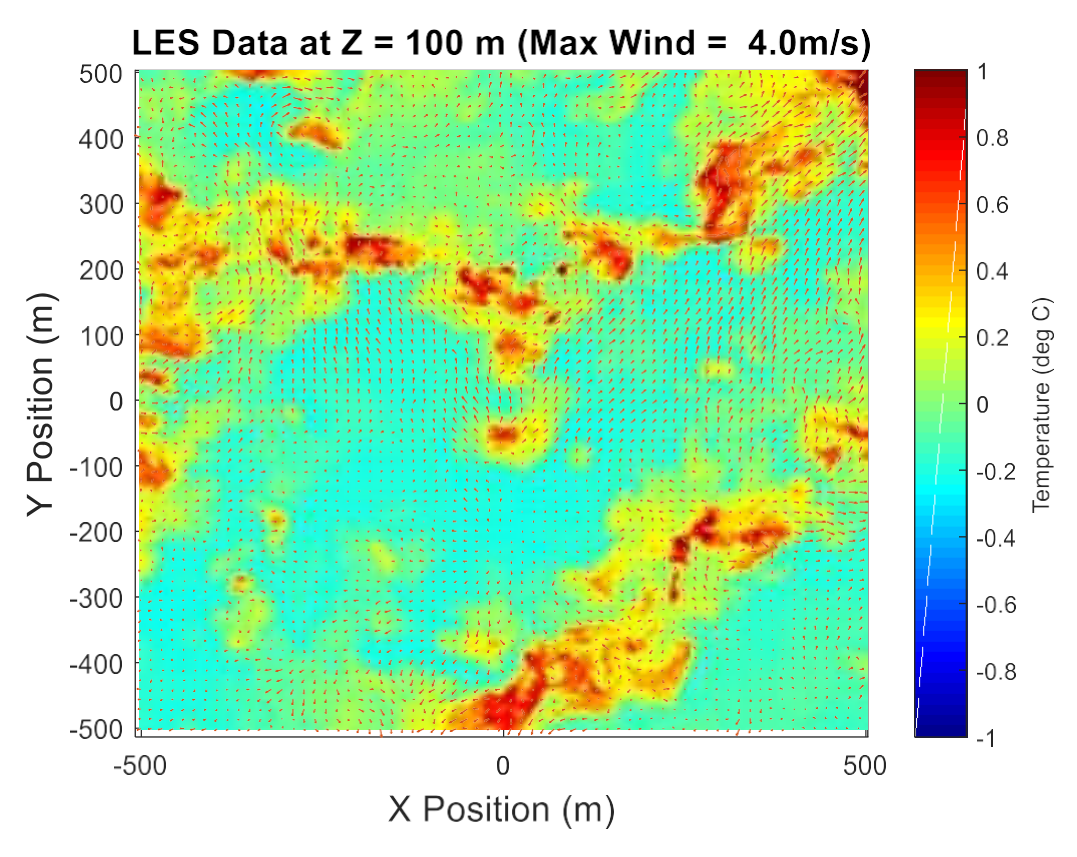


**Figure 15:** Cross-sections of a horizontal LES atmospheric profile at 100 m. Temperature is colour coded according to the scale on the righthand side. Wind speed is shown as arrows with magnitude proportional to speed (maximum, 4.0 m/s).

Figure 15a (top) shows a horizontal cross-section of temperature through the LES data set typical of that used in the analysis. Figure 15b-d (images, second top to bottom) show a representation of this data using RBF separated by 25m, 50m and 100m, respectively. The temperature is colour coded according to the bars on the righthand side of each figure, which show deviation from the average background temperature. Wind speed is shown as arrows with magnitude proportional to speed (maximum wind speed is 4.0 m/s). In other words, Figure 15b-d show spatially averaged LES data at varying degrees of resolution. The mismatch between these images and Figure 15a represents the *direct* error, i.e. an indication of the degree to which the target data can be accurately replicated using RBF.

To a first order the direct error is driven by the density of RBF. Although geometric acoustic assumptions for propagation through such a medium would be questionable, for RBF separated by 2m differences between estimated and target atmospheres are < 0.01°C and < 0.01 m/s rms. Lowering the resolution to 50 m increases errors to about 0.2°C and 0.1 m/s.

A requirement to reduce the spatial resolution of the estimate of the atmosphere is governed by the need to reduce the number of degrees of freedom (DOF) in the tomographic inversion: many DOF results in numerical instabilities. That is, the ill-conditioned nature of the inverse problem means that errors in poorly estimated coefficients propagate to others as the coefficient relationship is unconstrained (say, by a correlation distance [38]) except on flight path of the UAV.

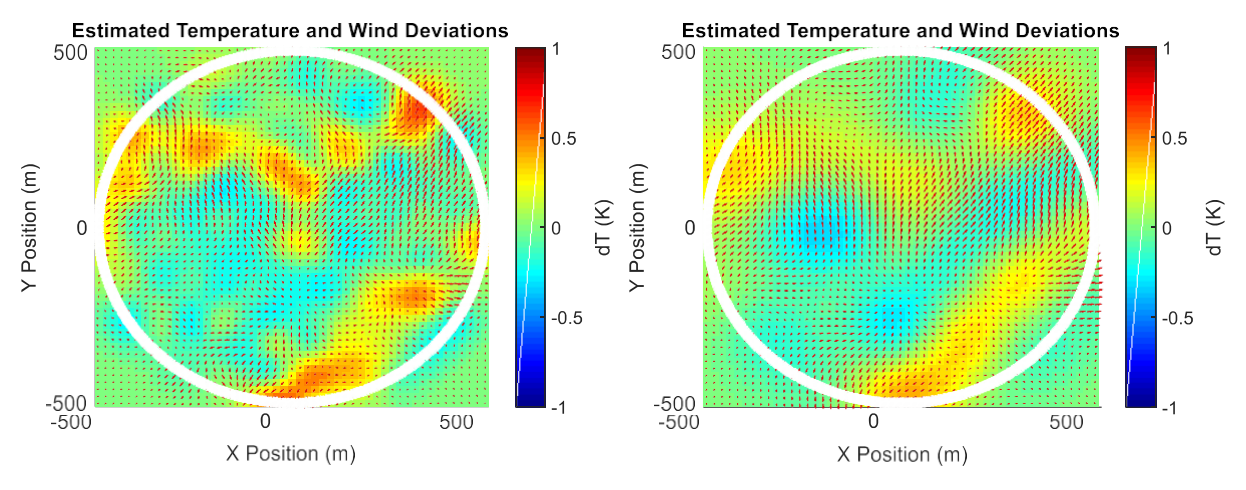


**Figure 16:** Estimated temperature and wind profiles based on (left) no time delay, path length, and GPS errors and (right) 10ms signal processing, 0.1% path length and 0.1 m GPS errors. Separation between RBF for the left-hand image is 75m and 150m for the right-hand one. The white asterisks represent the circular orbits flown by the UAVs.

### 3.2 Performance assessment: field comparisons

To assess the accuracy of the AAT, the results obtained through tomographic inversion were compared to a ZephIR LIDAR. LIDAR operates using similar principles to radar: near infrared light energy is emitted by the lidar and particulate matter carried by the atmosphere scatters the light, such that the wind velocity and height information may be obtained as a function of height from the Doppler shift and time delay information measured in the returned signal. To achieve this, assumptions are made regarding homogeneity of scatterers and the way they are carried by the wind. For a more complete understanding of the operating principles of these instruments the reader is referred to (Hall Jr et al., 1984, Hooper and Eloranta, 1986, Singal, 1997, Antoniou et al., 2003, May et al., 1989, May et al., 1988, May et al., 1990, Strauch et al., 1984).

Over a period of 5 days, field trials were conducted near Rowland Flat in South Australia. The days were hot  $(max > 40^{\circ}C)$  with moderate winds (5 - 10m/s). The UAV was repeatedly flown at an altitude of up to 120m above a 300m x 300m array of 49 microphones. The inter-sensor separation distances for the microphones was approximately 50m. All were positioned approximately 1.5m above ground level. The ground was flat with variation in elevation of about 12m. The vegetation was vines in full leaf (close to harvest).

The location of each microphone was determined using Real Time Kinematic Carrier Phase Differential Global Positioning System, which has an accuracy of  $\pm 0.03$ m. The UAV was also fitted with RTK CP DGPS, enabling position recording at 5Hz with similar accuracy. Horizontal wind velocity, air temperature, barometric pressure and relative humidity were also recorded onboard the UAV at 1Hz.

For practical reasons, the LIDAR was located just outside the microphone array, approximately 50m northwest of the sensor coinciding with the origin of the coordinate system. 3D wind velocities were observed at 10m intervals between altitudes of 30m and 110m every 15sec. The  $(1\sigma)$  nominal uncertainty for measurement error reported by the manufacturer is 0.3m/s for each axis, but this figure is generally dependent upon the prevailing conditions and particulate matter contained by the atmosphere. A more detailed assessment was not made.

A DJI Phantom IV UAV carrying two iMet-XQ sensors was also repeatedly flown around the perimeter of the microphone array between an altitude of 20m and 120m. Two sensors were used as there is typically up to 0.5°C variation between the two sensors, depending upon their placement on the UAV (Jacob et al., 2018). Position (based on SPS GPS), thermodynamic temperature, pressure, and relative humidity were recorded at 1Hz.

Pressure was used (in conjunction with a third, ground-based iMet-XQ sensor) to accurately determine sensor altitude to within ±0.5m as the vertical component of SPS GPS is generally accurate only to about ±20m. Thermodynamic temperature was converted to virtual temperature based on measurements taken onboard the UAV. Based on laboratory tests, the temperature sensor is known to be accurate to ±0.3°C.

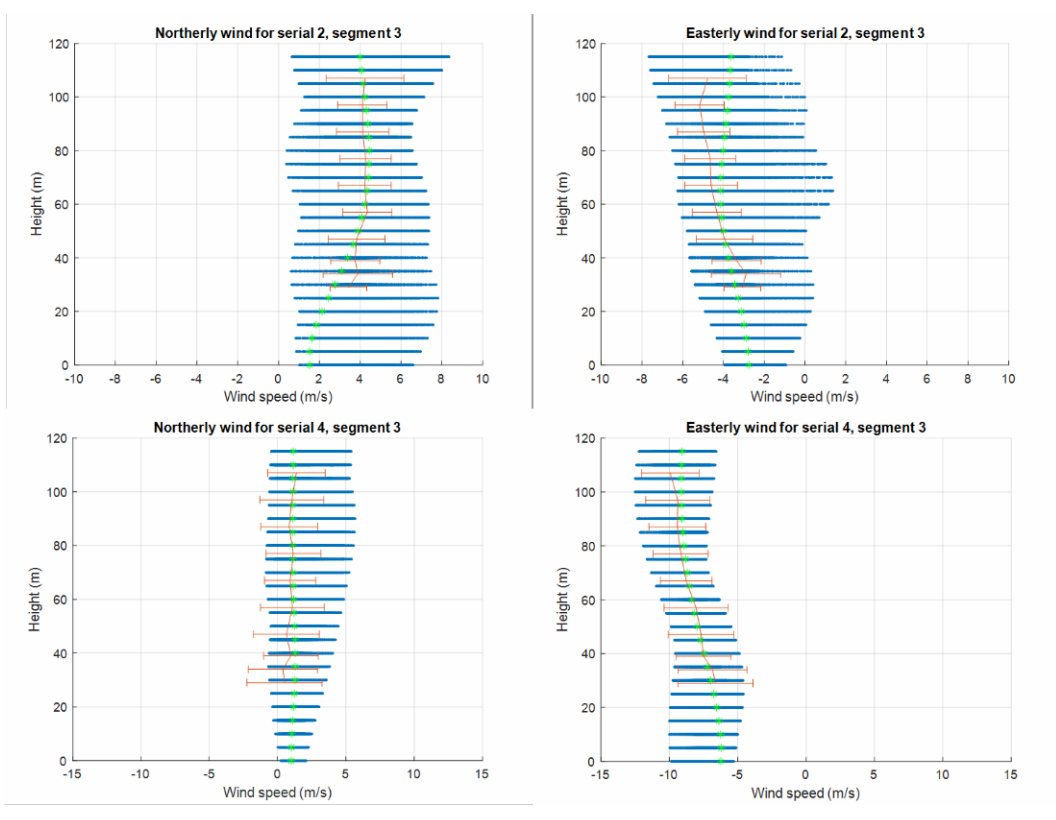


Figure 17: Comparison between horizontal wind speed components observed by LIDAR (red) and UAV-based AAT (green)

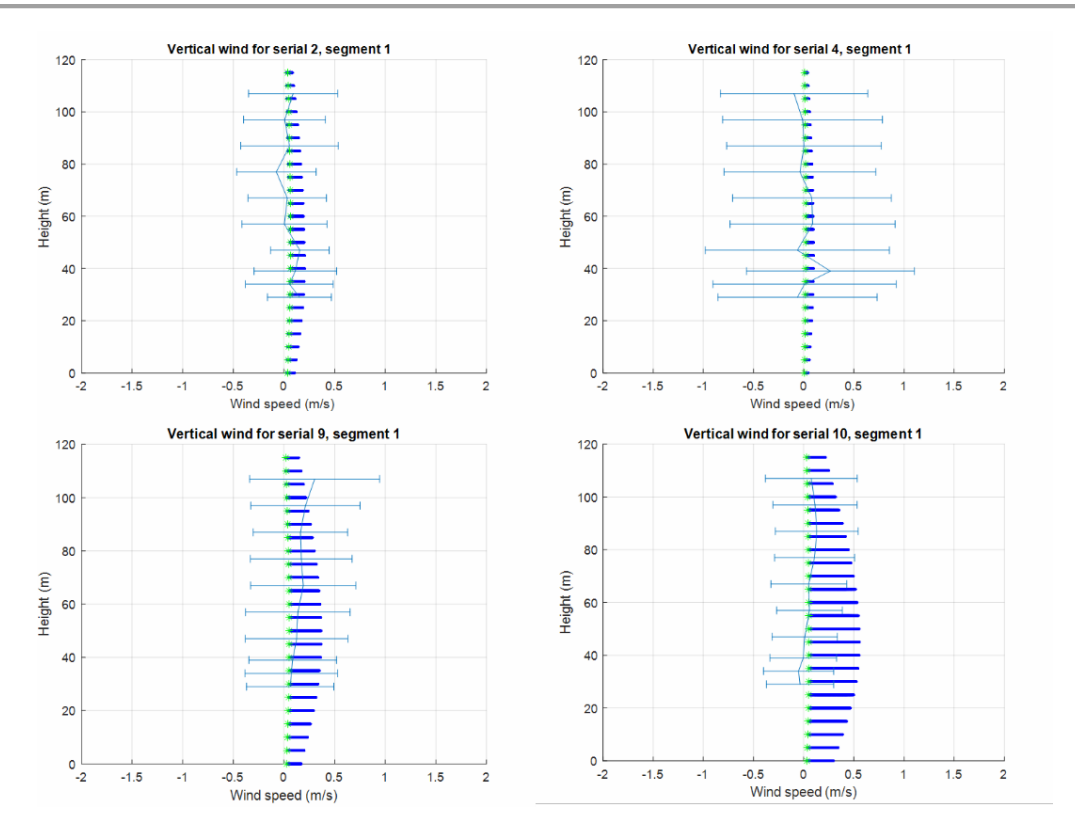


Figure 18: Comparison between vertical wind speed components observed by LIDAR (cyan) and UAV-based AAT (green)

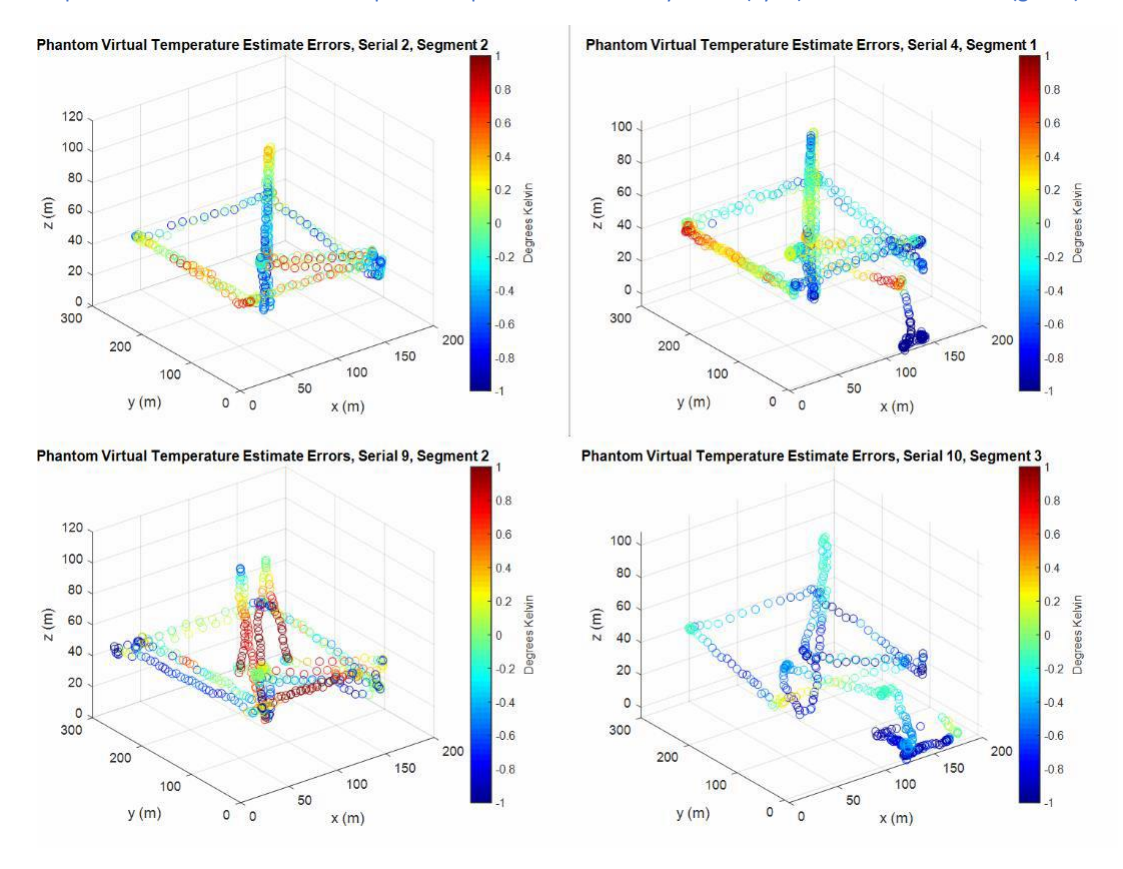


Figure 19: Comparison between temperature measurements directly observed (from a UAV) and AAT-derived

3D temporally averaged volumetric atmospheric profiles for wind velocity and temperature were then obtained using UAV-based AAT. These were compared to the independent measurements taken by the LIDAR and sensors onboard the Phantom UAV (Figure 1, Figure 2, and Figure 3).

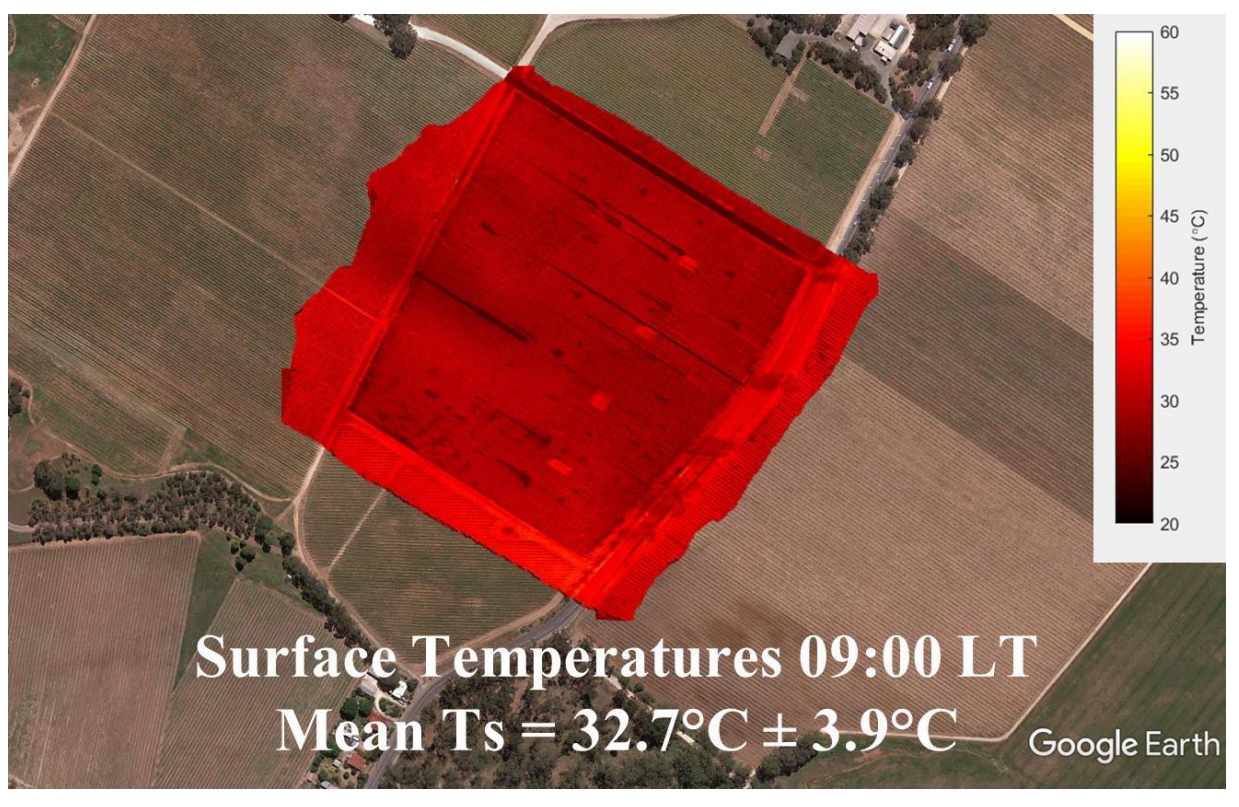
In Figure 17 and Figure 18 the vertical red line represents the temporal average of the LIDAR data over the duration of the entire AAT observation set, whereas the green dots represent the AAT estimates at each 10m increment for the location closest to the LIDAR. The (red) error bars associated with the LIDAR data represent min/max variation of the LIDAR measurements over the observation period of the AAT, whereas the blue bars represent the min/max variation of the AAT estimates over the area of the array at each 10m interval.

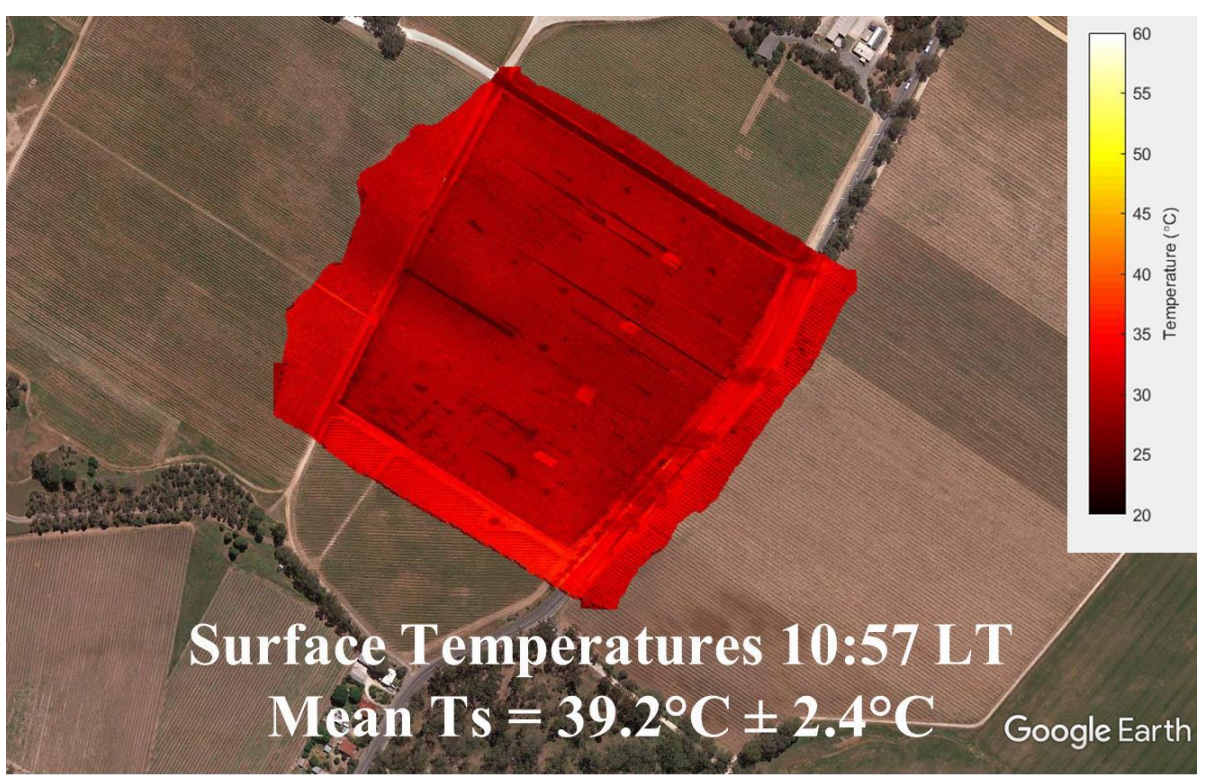
In Figure 19 typical differences between the mean of the virtual temperatures observed by the two iMet sensors onboard the Phantom UAV and the AAT estimates are displayed. They are colour-coded in accordance with the scale on the right of each image. The coordinate system is such that the origin coincides with the leftmost microphone of the array. The positive y-axis points forward through the left- most line of microphones, the z-axis is vertical and the x-axis orthogonal to these two axes, roughly coinciding with the first microphone in each row.

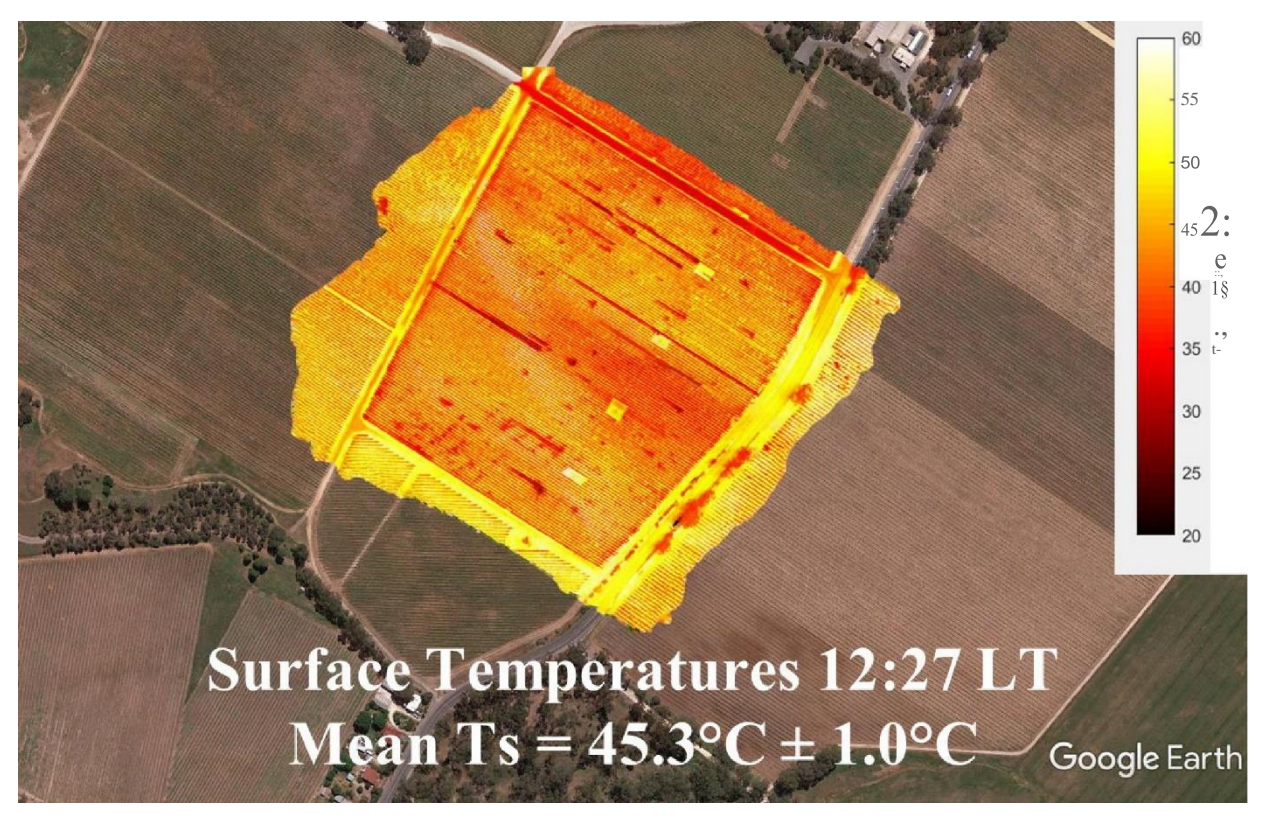
The AAT and UAV/LIDAR measurements show correspondence accuracies of around 0.5°C for temperature and 0.3m/s for each component of wind velocity, respectively. This compares very favourably to other interinstrument atmospheric comparisons, such as LIDAR vs. SODAR and is within the measurement errors of the system. The correspondence also accords with the performance envelope determined using the LES data set. Optimisation of the procedures used in the AAT and a more detailed analysis of this data continues.

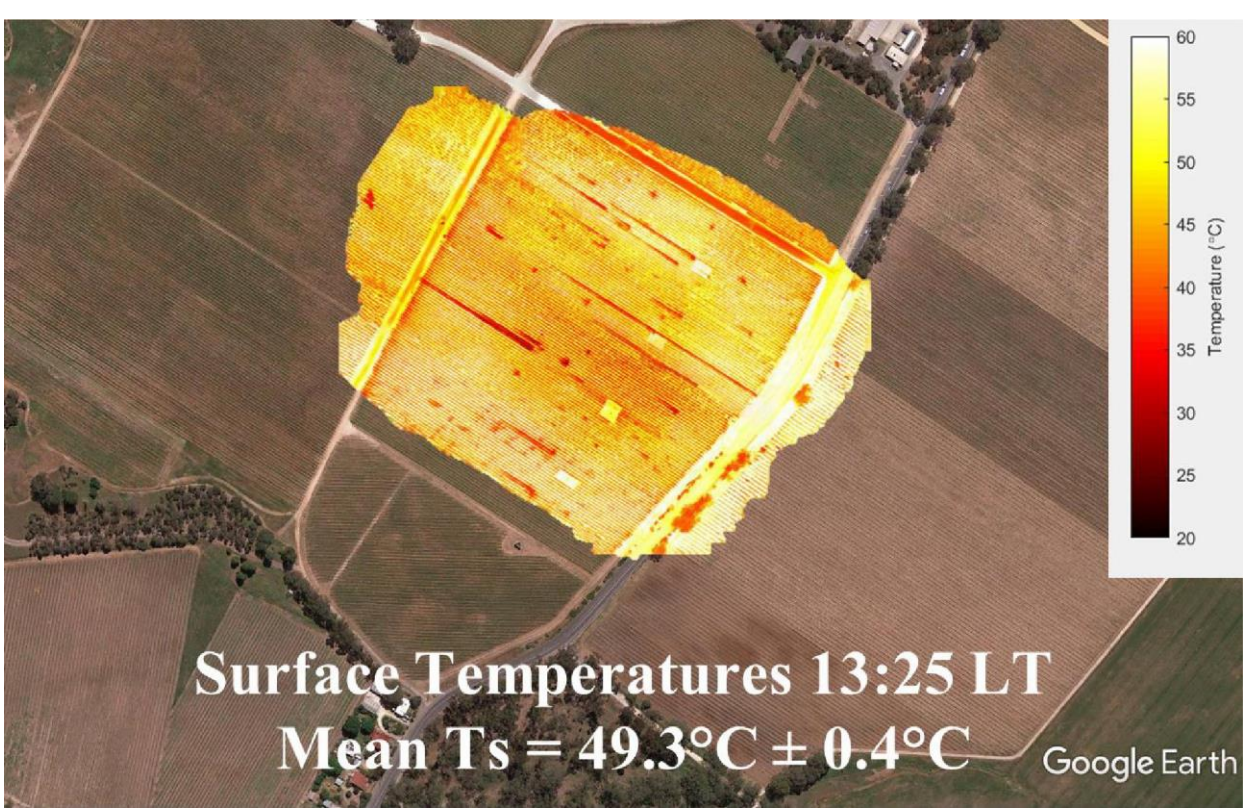
# 4 Field measurements

#### 4.1 Heat stress easurements









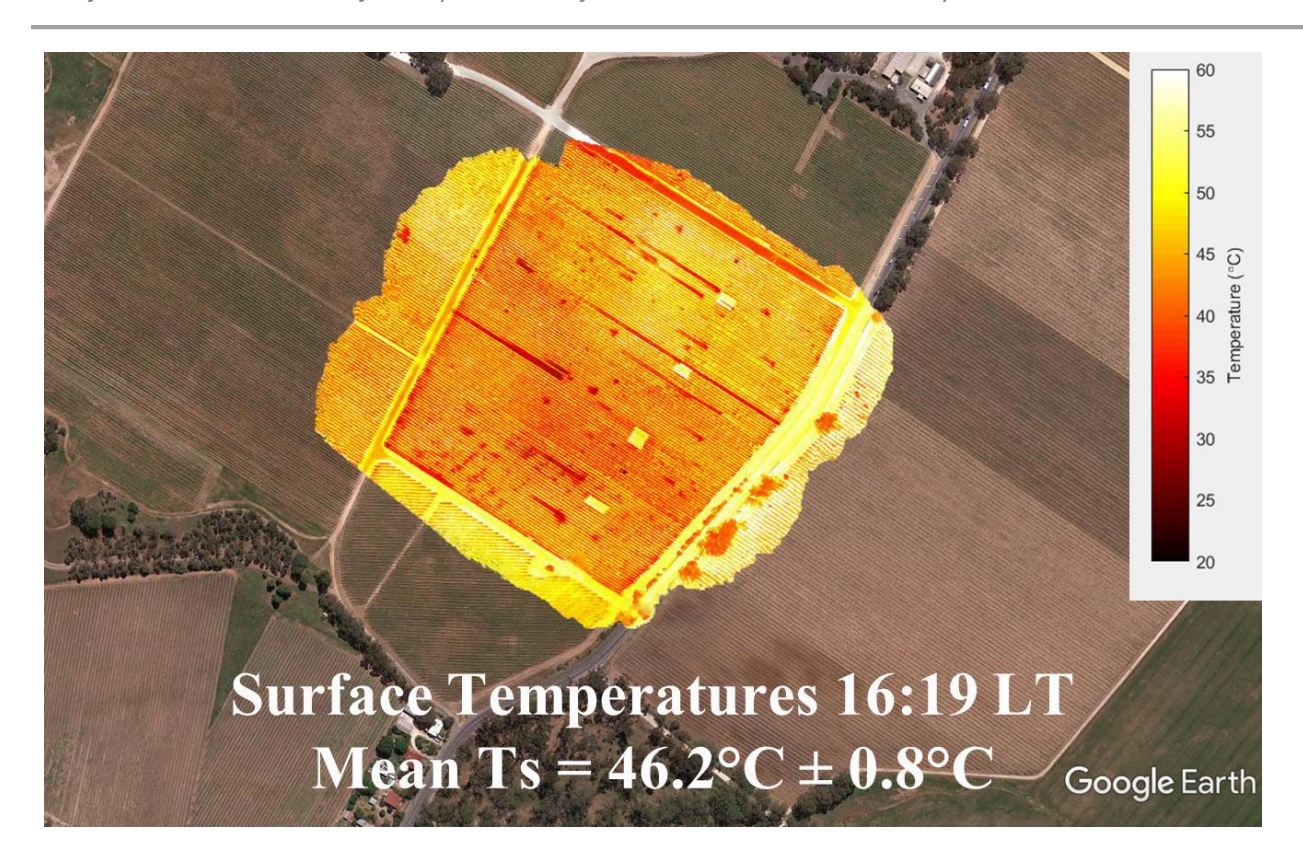
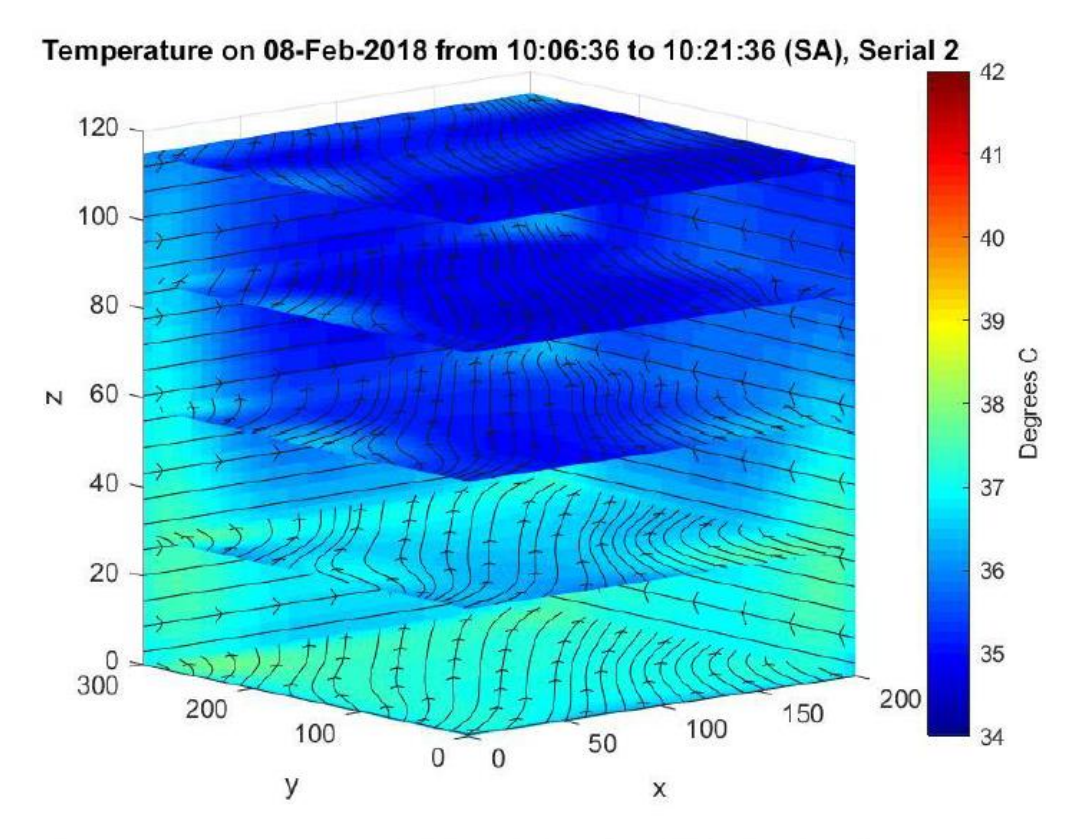
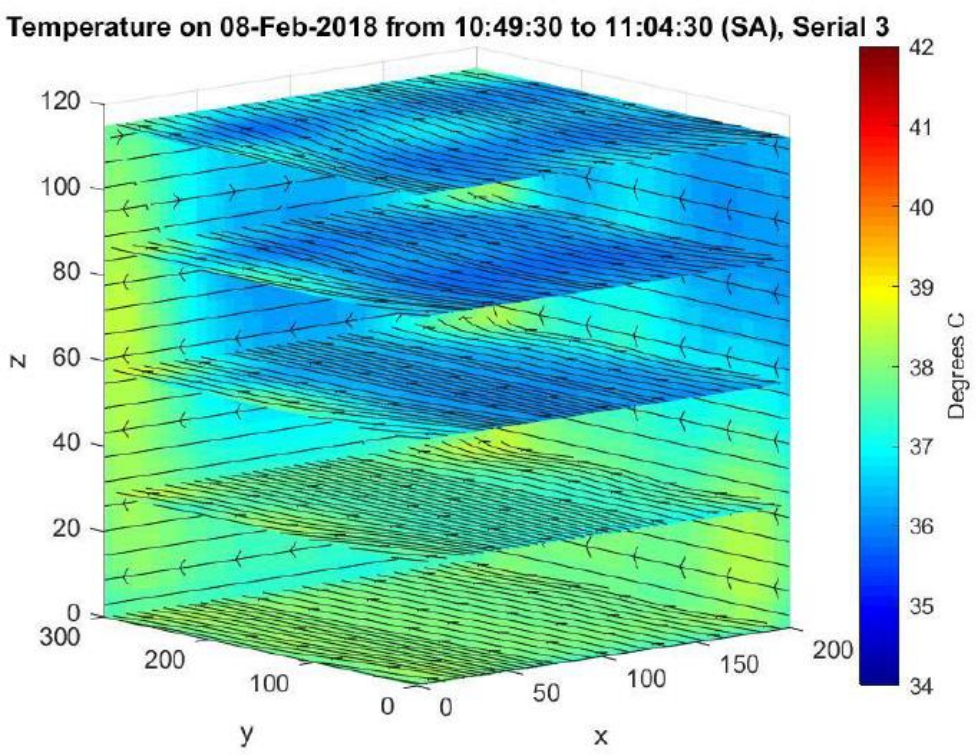
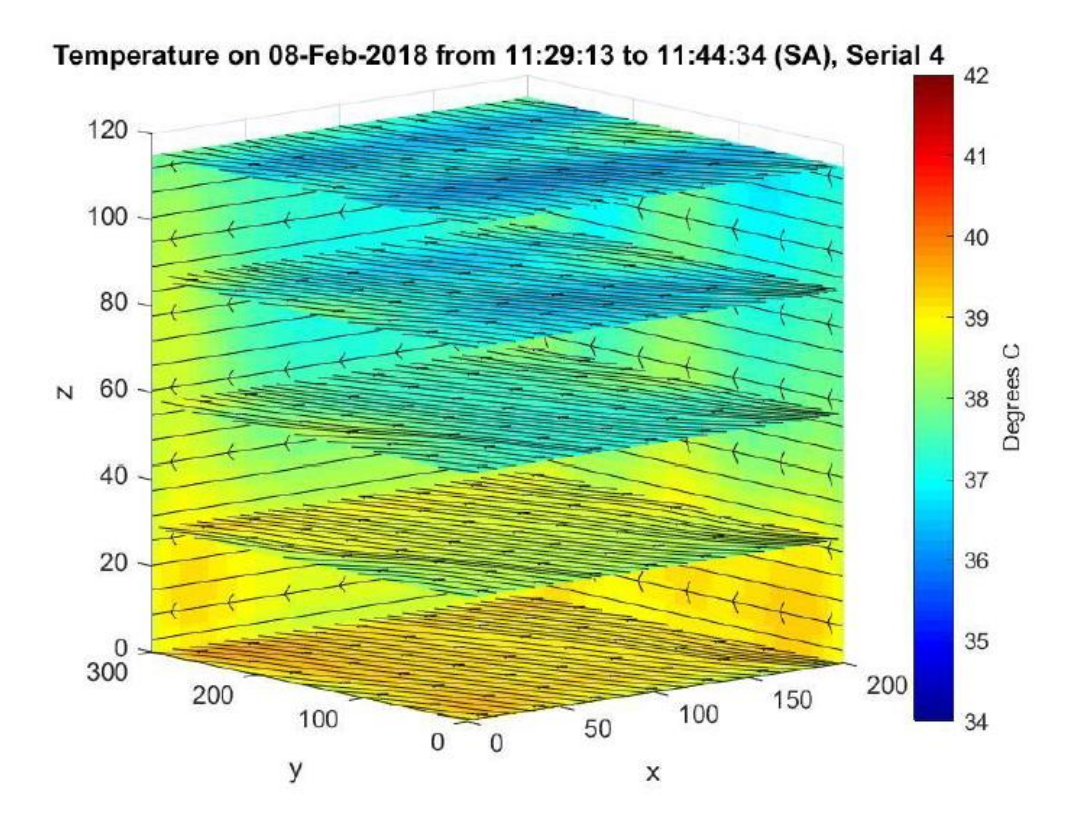


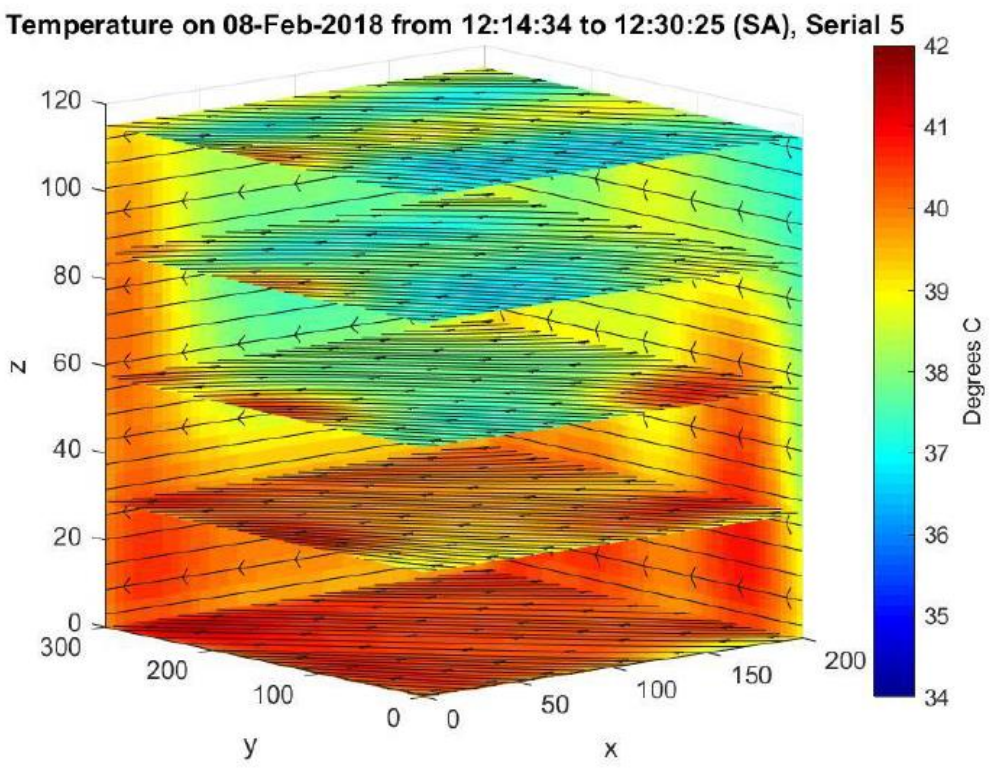
Figure 20: Thermal maps of the Jacob's Creek vineyard superimposed onto a Google Earth image

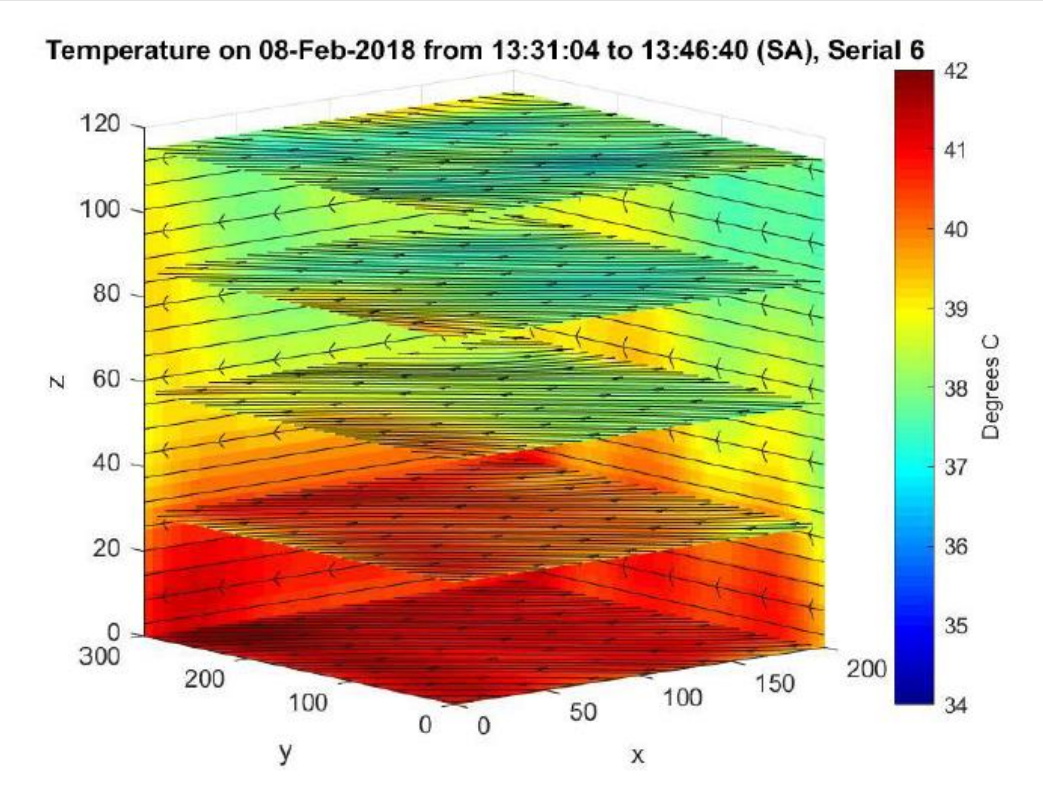
Heat stress measurements were conducted on days for which maximum air temperatures exceeded 40°C. Trials were conducted at a Shriaz vineyard at Jacob's Creek, Rowland Flat. The results below, which show orthographic projections of thermal maps of surface temperature obtained using the LWIR payload and 3D temperature and wind velocity profiles, are for a day with maximum temperature 42°C.

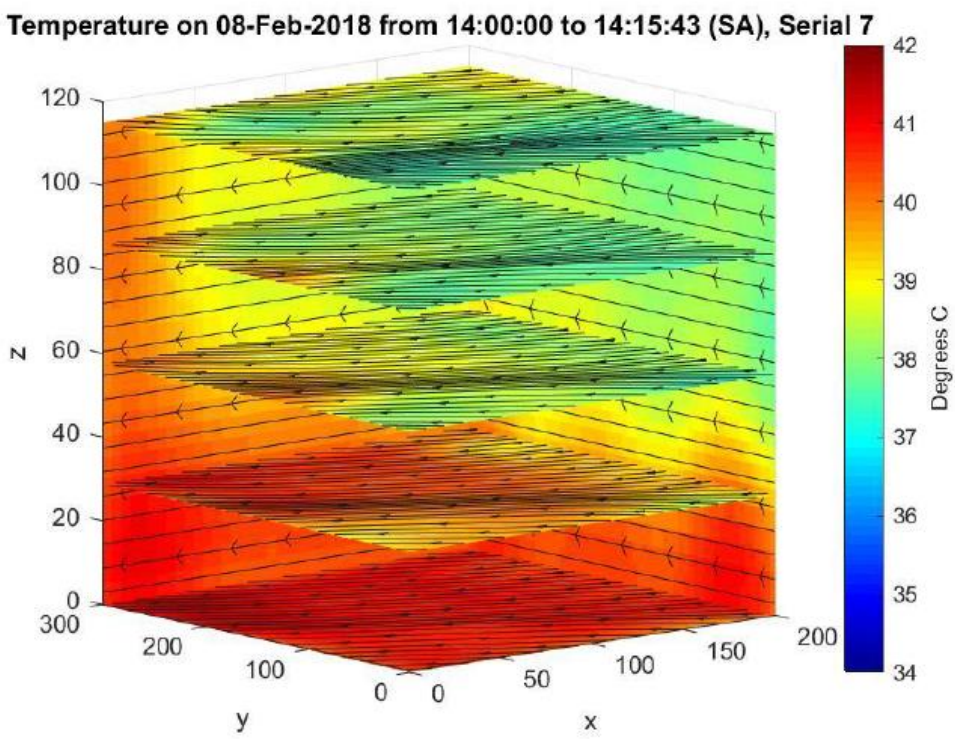


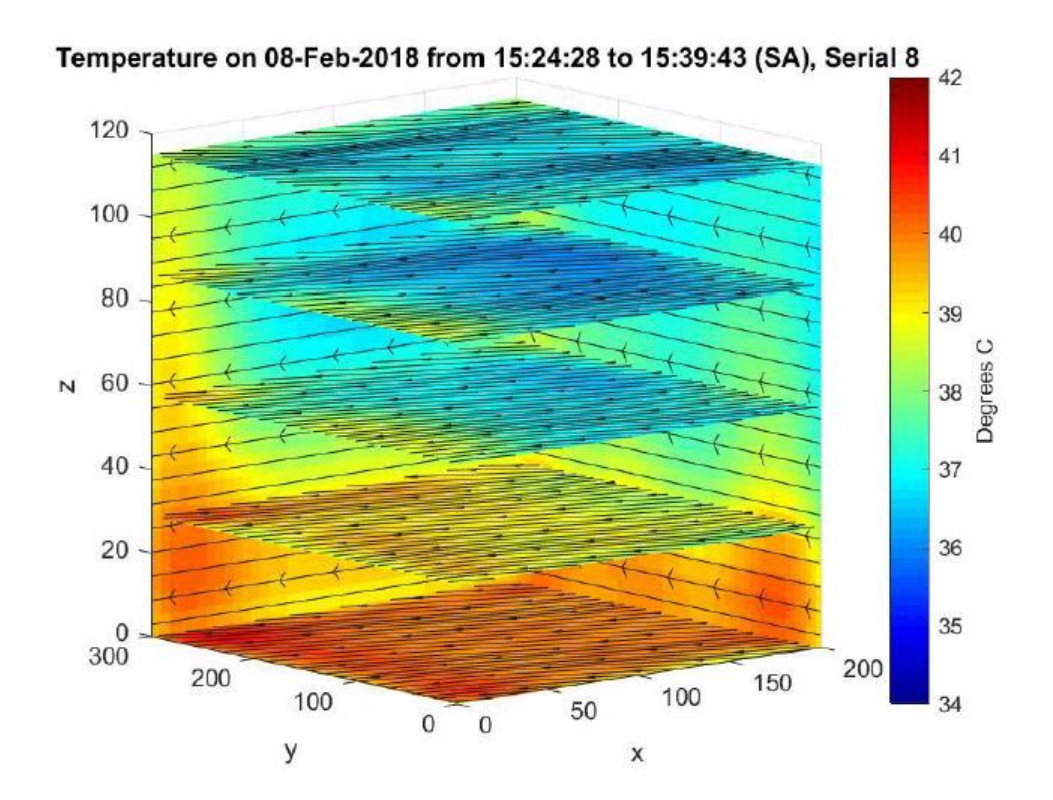


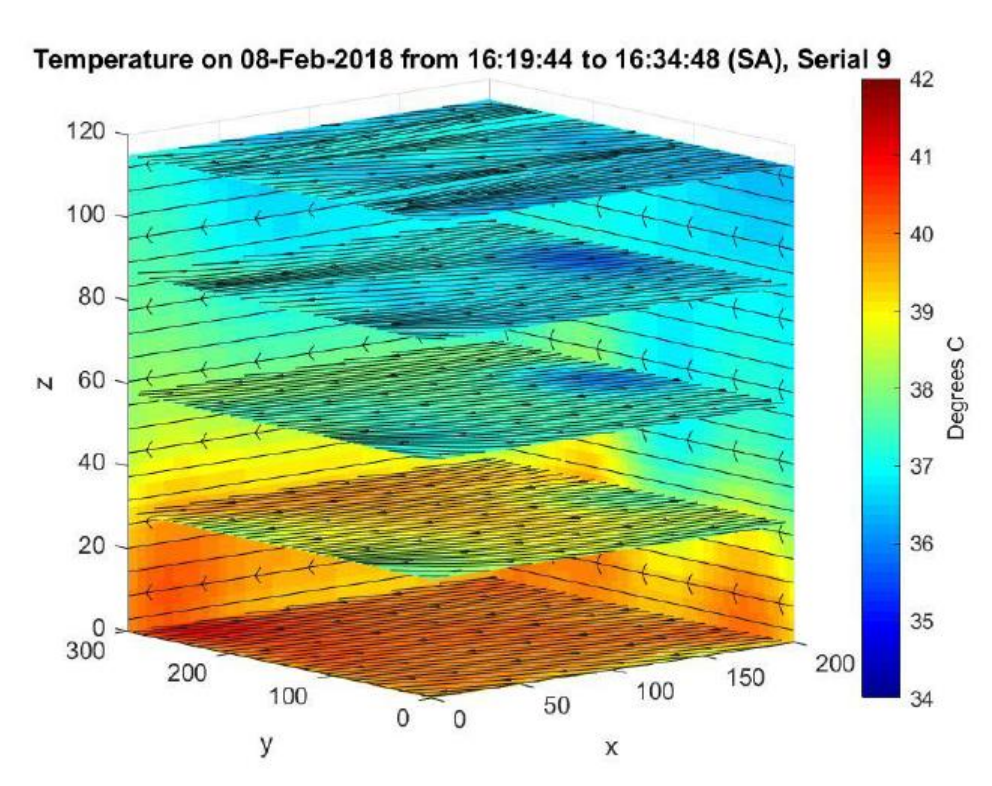


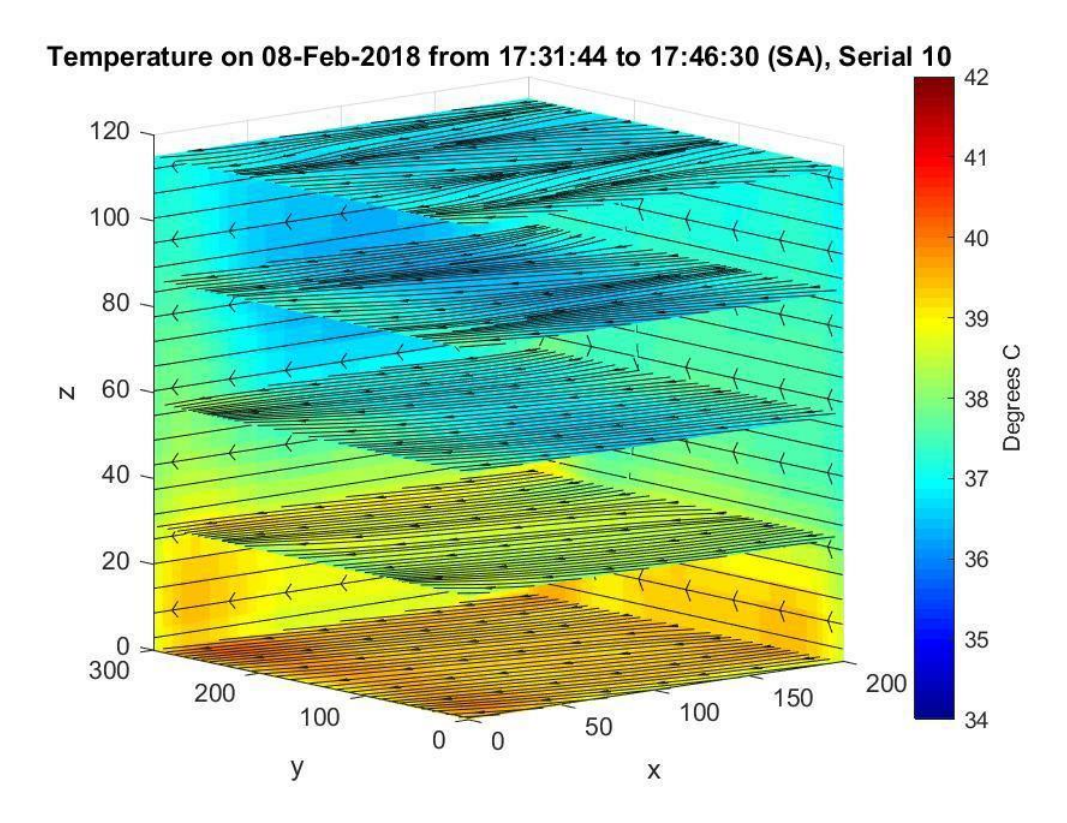




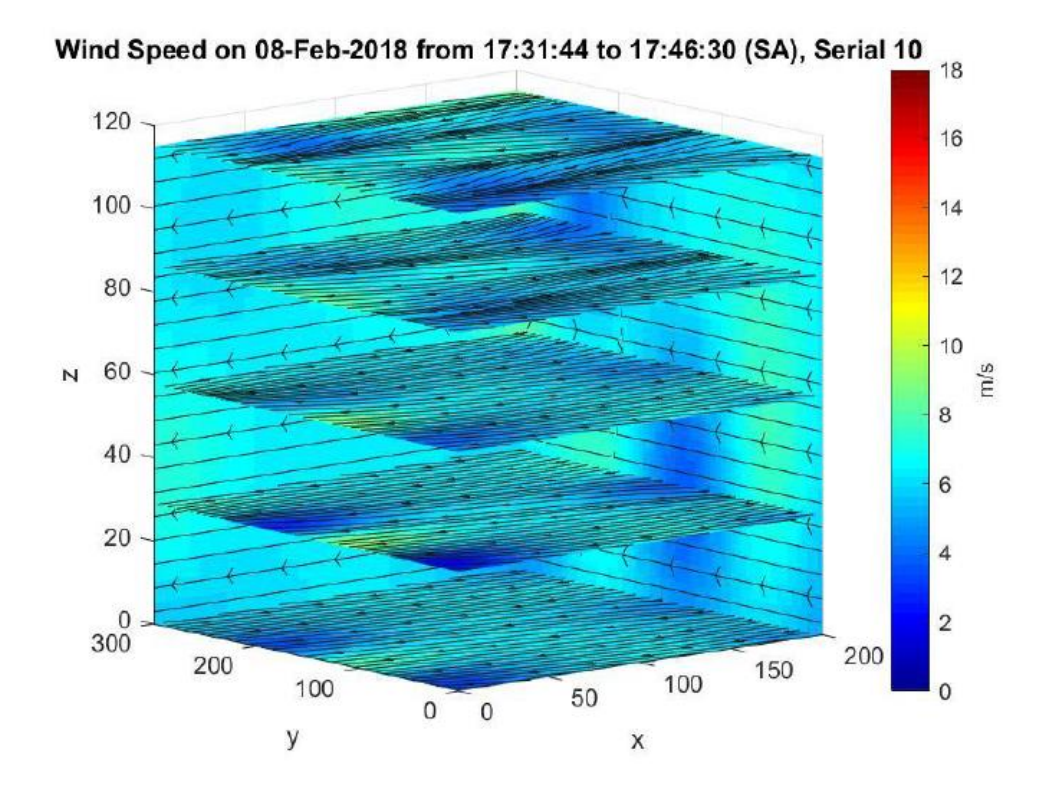


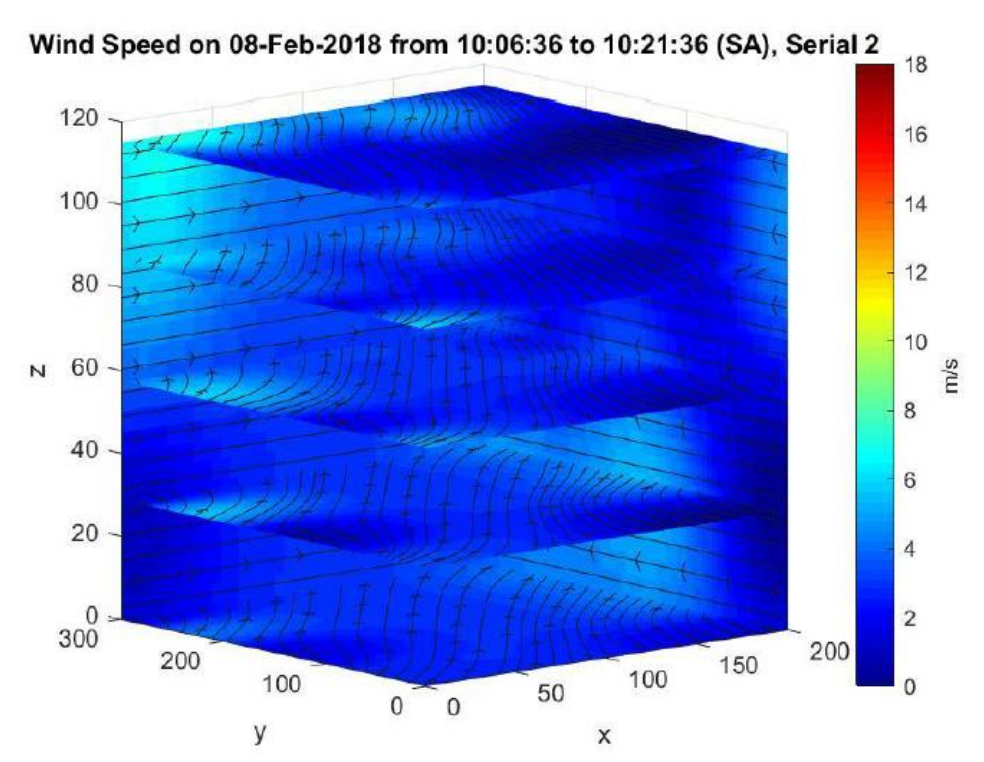


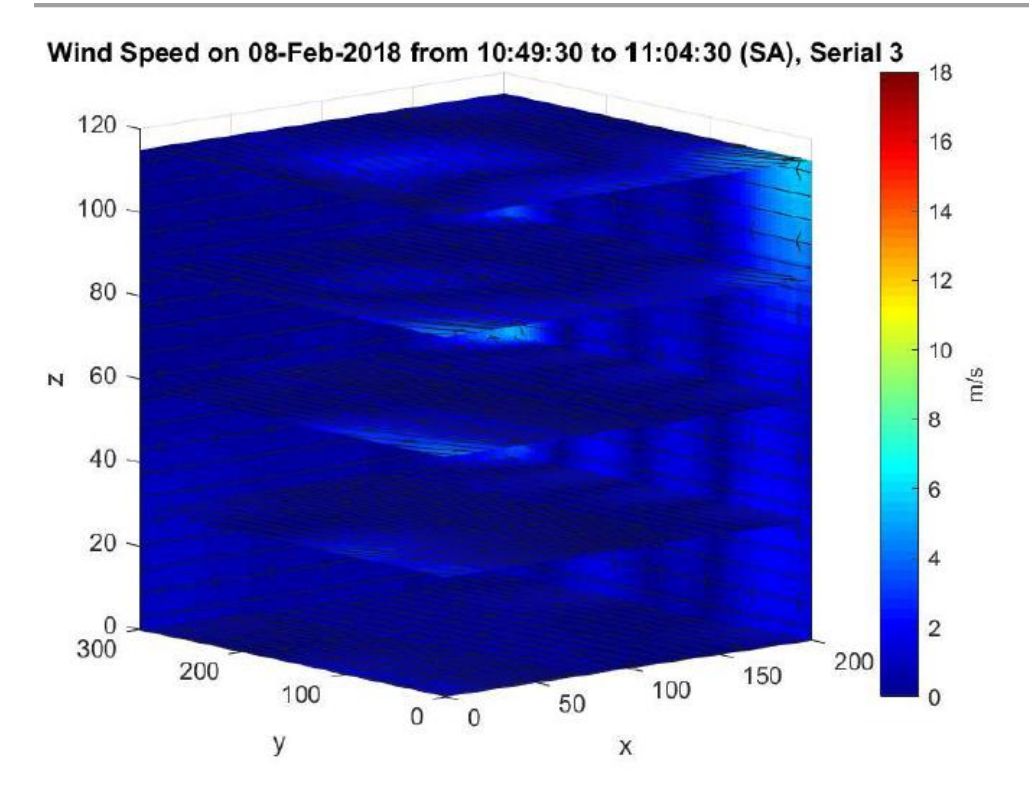


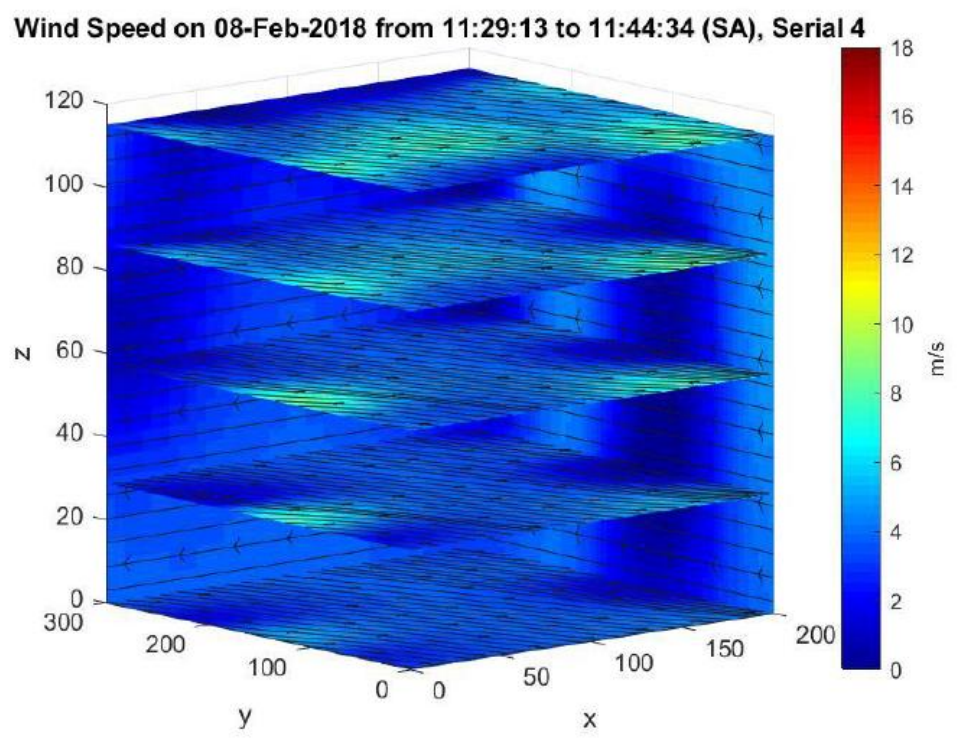


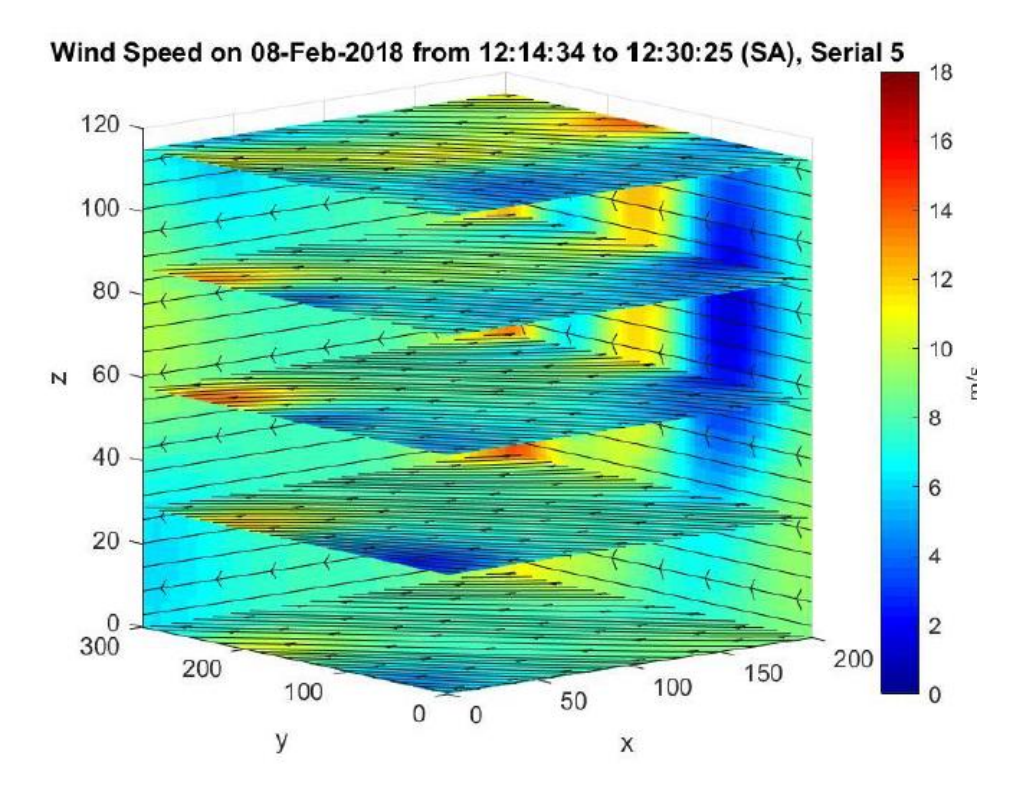
**Figure 21:**Three-dimensional temperature profiles above the vineyard. Each image shows the 3D temperature profile at a different time of day, colour-coded in accordance with the bar on the right of each image. The arrows indicate the wind direction in each slice/plane of the atmosphere.

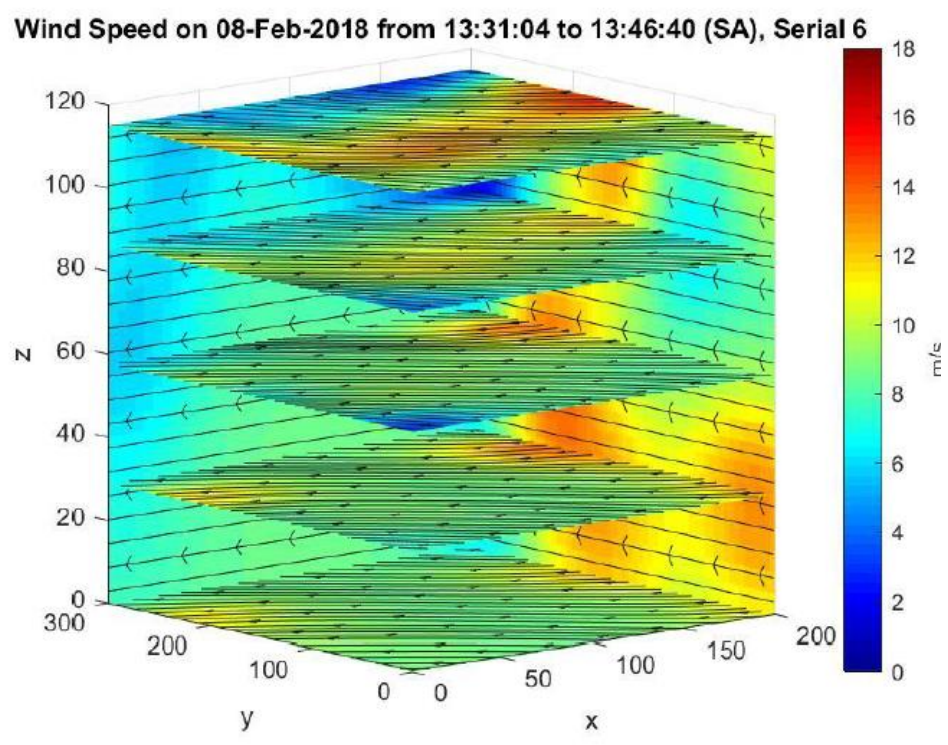


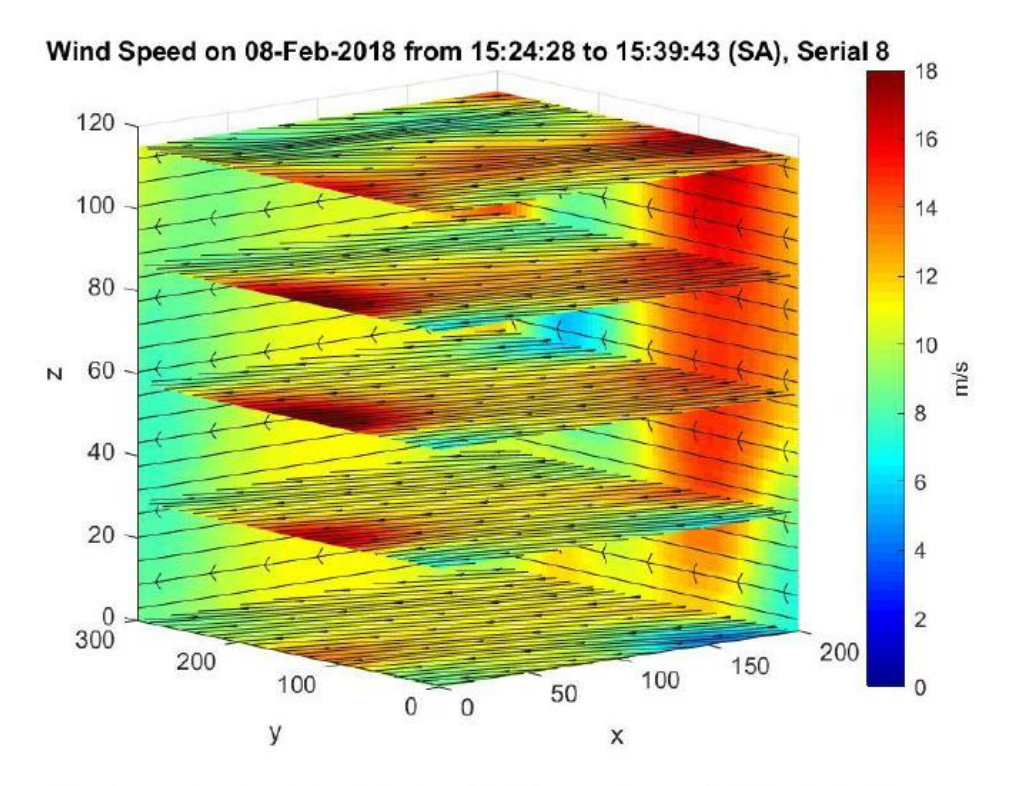


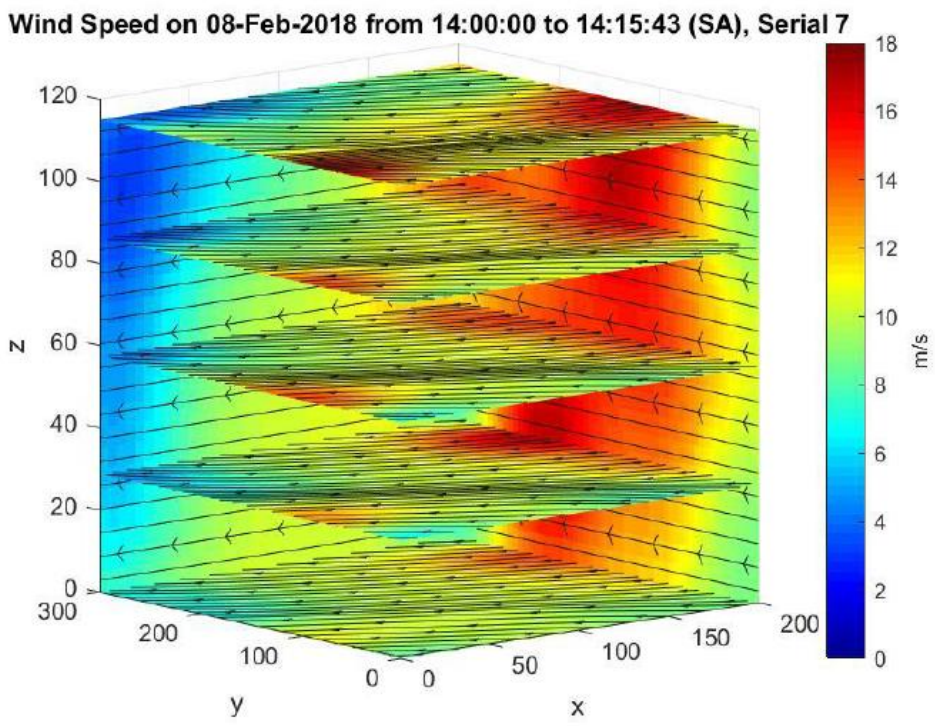


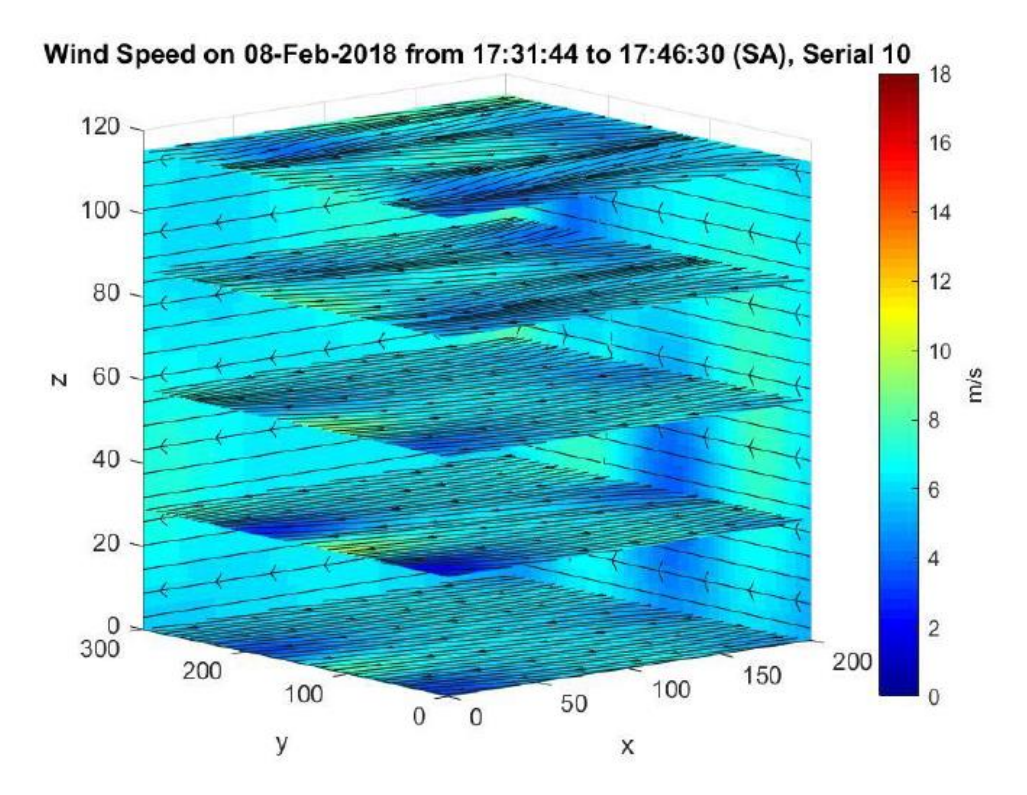












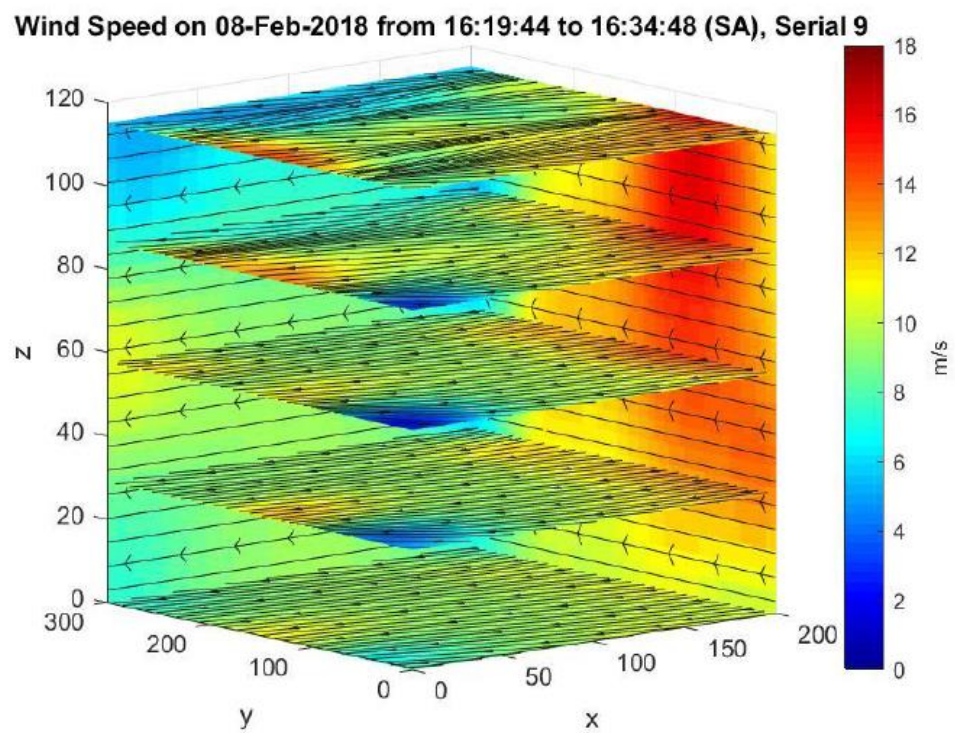


**Figure 22**: Three-dimensional wind speed profiles. Each image shows the 3D wind speed profile at a different time of day, colour-coded in accordance with the bar on the right of each image. Arrows indicate wind direction in each slice/plane

The spatial resolution of the thermal camera provided a ground sampling distance of about 10cm. The vine canopies were approximately 1.5m high. They are not pruned, and terrain undulates slightly over the roughly 10Ha area of the test site, varying by around 12m from lowest to highest points. The surface temperatures of the (non-plant) material in the vineyard routinely exceed 60°C; and there is considerable variation across the vineyard. Irrigation ruptures and poorer performing vines are readily visible. At the hottest part of the day vine temperatures reach 40°C.

Under these harsh conditions, irrigators have traditionally relied on local or regional weather stations to estimate crop evapotranspiration (ET), the volume of water lost from a vineyard that needs to be replaced via irrigation. However, the detailed spatial and temporal knowledge of micrometeorological information now available as a result of this project enables us to compute theoretical grapevine water status and thus (potentially) optimise water application requirements.<sup>4</sup>

In order to compute these parameters, the temperature balance between the vines (leaves) and the atmosphere must be determined. This balance is largely regulated by the transpiration rate and hence stomatal conductance. Leaves interact with their environment through energy exchange processes. This allows vines to optimise their metabolic functions, and when there is an imbalance leaf temperature changes until a new equilibrium is achieved.

Leaf temperature is thus a function of the interaction of several factors/processes: air temperature, absorbed/re-emitted solar radiation,, and the processes of convection and transpiration [39, 40]. The basic components of the plant energy balance can therefore be divided into: absorption of shortwave solar radiation by leaf tissues; net absorption and emission of long wave radiation from the sky and terrestrial infrared radiation); heat exchange via convection and conduction between the (physical contact of) leaf surfaces and the surrounding air; and evaporative cooling due to leaf transpiration, i.e. through the movement of water by diffusion from the inner leaf surfaces, through the stomatal pores, to the atmosphere (the phase transition from liquid to gaseous water causes cooling).

Some results for the Jacob's Creek trial are shown below. These estimates of ET are achieved through computation of net solar load, vapour pressure, and sensible and latent heat flux using the well-known Penman-Monteith Equation [41, 42]. One of the key benefits of the technique developed under this project is that wind profiles need not be estimated from point measurements 2m above the ground and surface temperatures are measured directly.

It is noteworthy that—as the energy exchange due to transpiration is influenced by stomatal conductance, the difference in water vapour pressure between the leaf and air, and the boundary layer conductance— it is possible to compute stomatal conductance as a function of vineyard geography using the technology developed under this project. This becomes possible because we are able to observe or estimate so many of the factors that impact stomatal conductance, e.g. related transpiration rates, as well as environmental factors such as air temperature, solar radiation, and wind speed. We are also able to compute indices such as the Crop Water Stress Index (CWSI) to provide an indication of relative stomatal conductance.

Some results for a heat stress trial conducted at Jacob's Creek, Rowland Flat are shown below.

39

<sup>&</sup>lt;sup>4</sup> Noting that capitalising on the microclimatic information now available would require a sophisticated irrigation system capable of supplying water differentially across the vineyard.

<sup>&</sup>lt;sup>5</sup> A data set was obtained under a collaboration with Adelaide University, but this is still to be fully analysed.

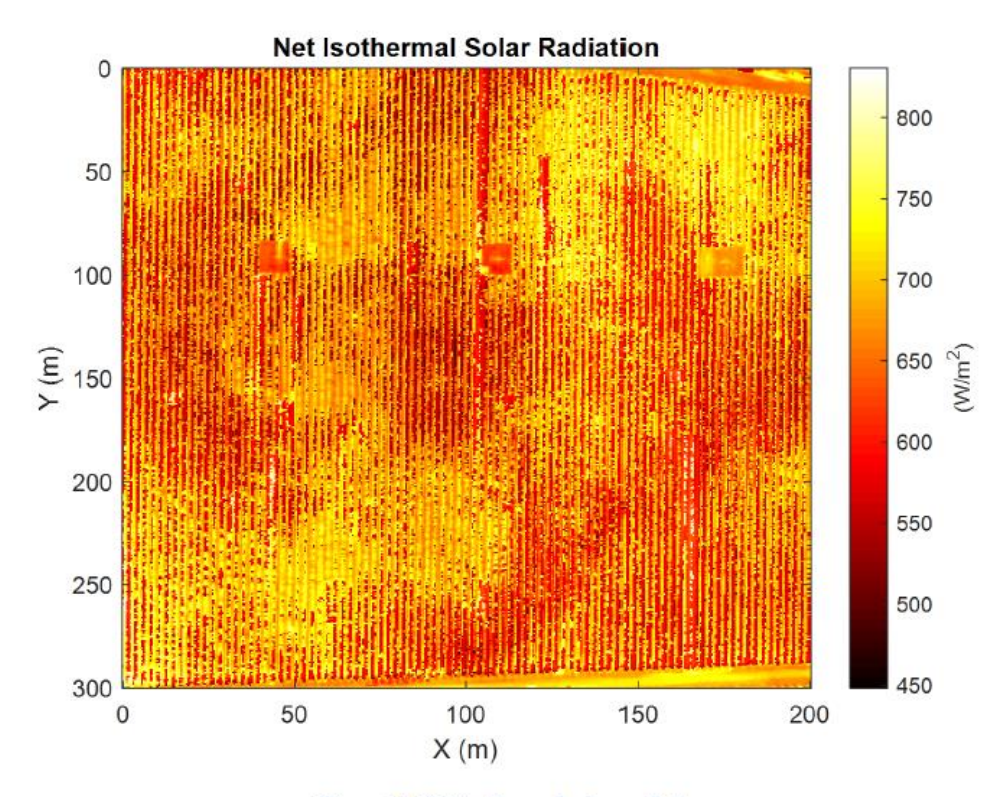
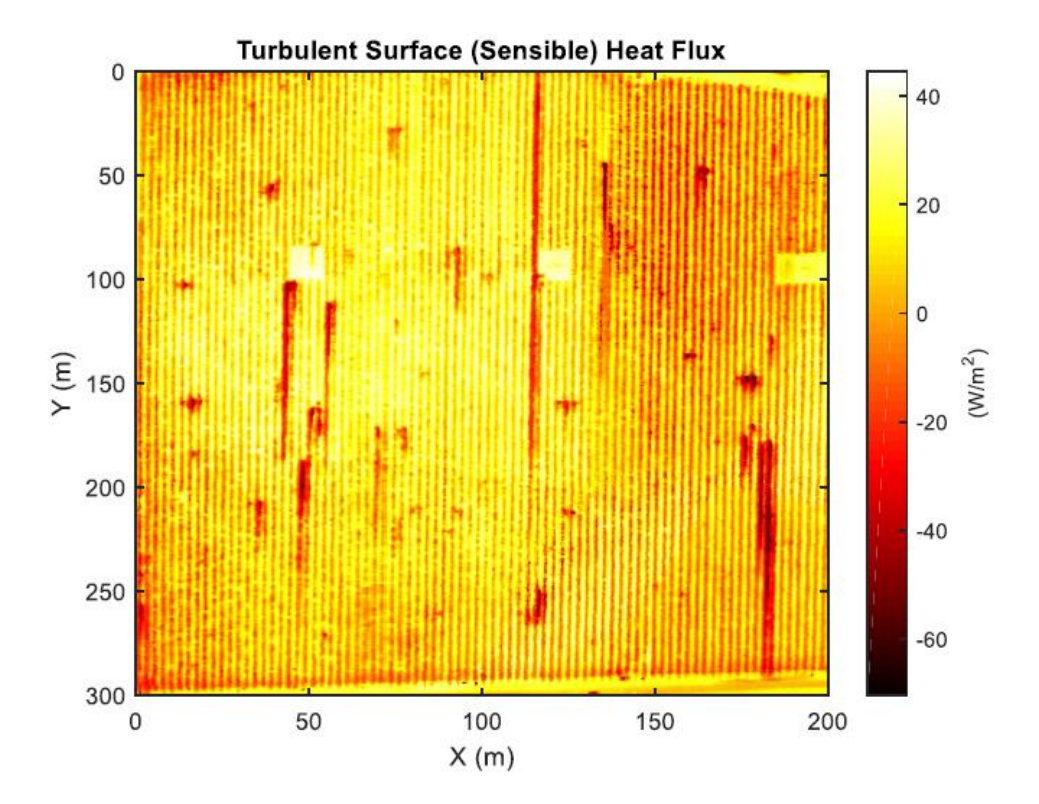


Figure 23: Net isothermal solar radiation



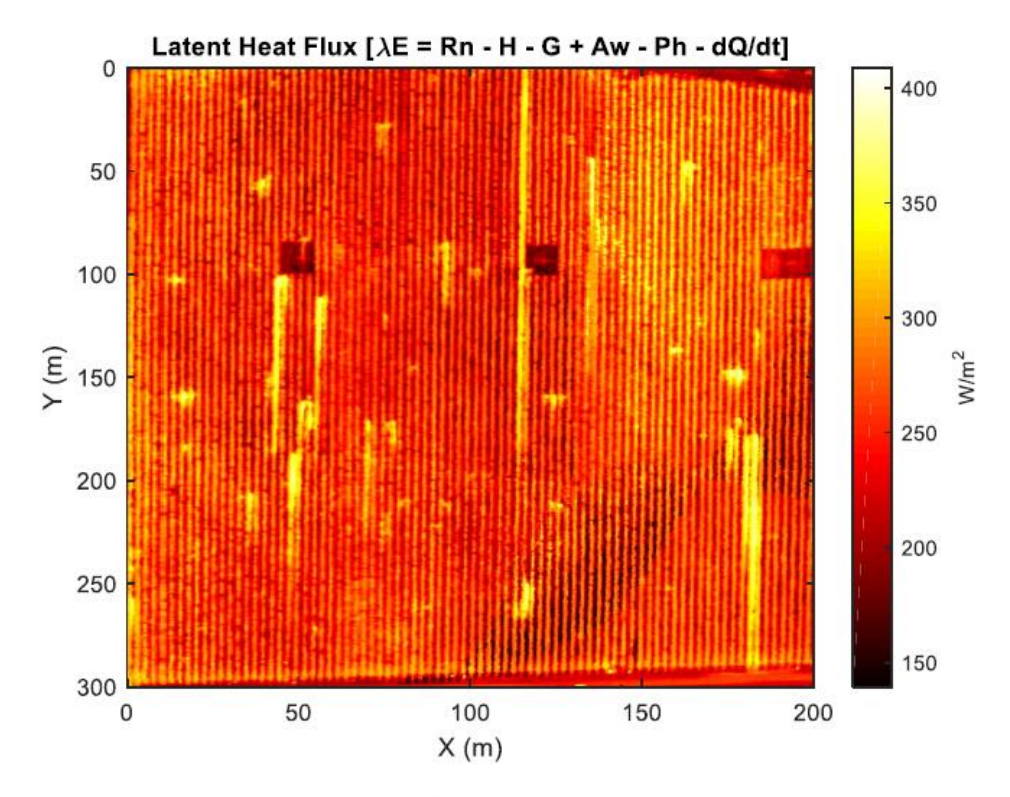
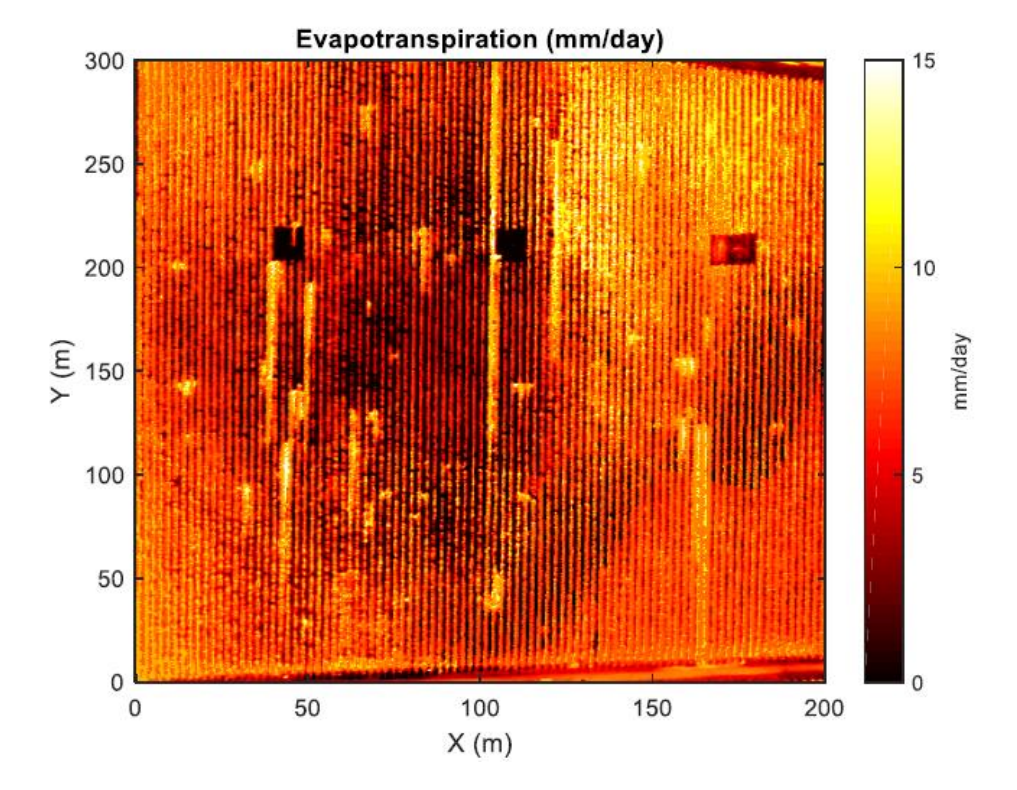


Figure 24: Sensible and latent heat flux



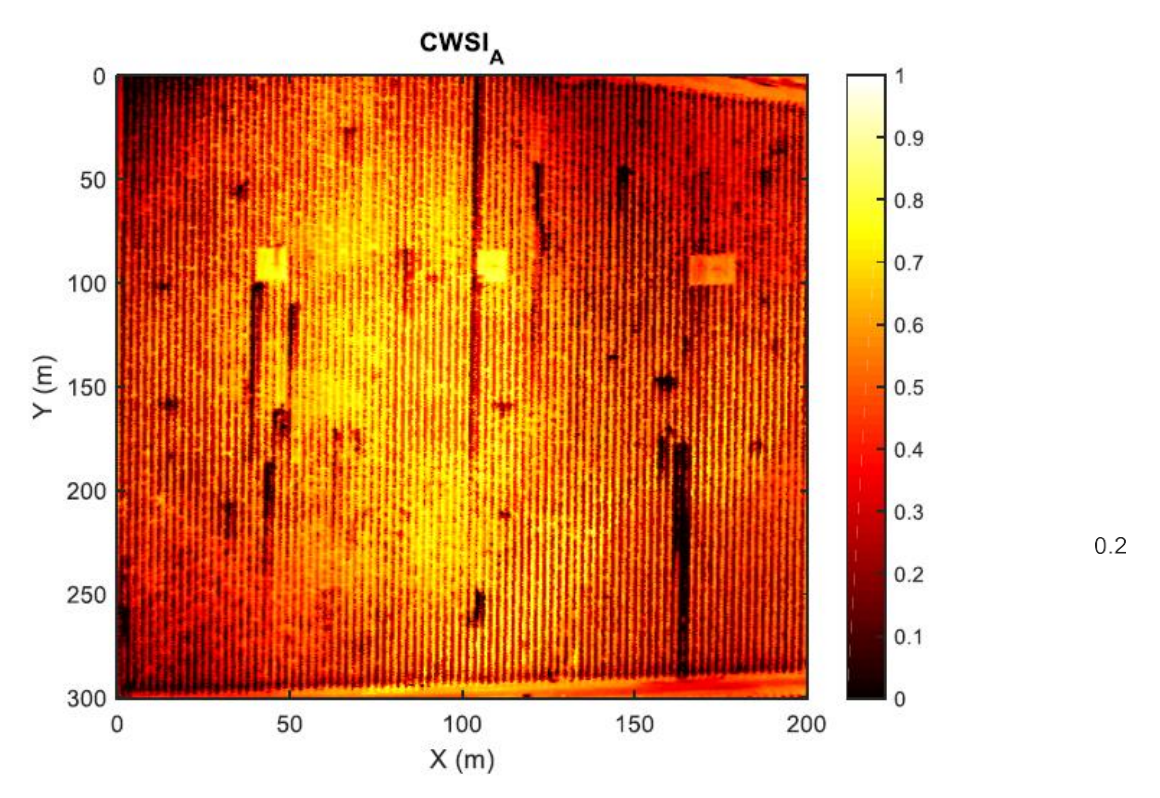


Figure 25: Evapotranspiration rates and crop water stress index

Another advantage of the UAV-based thermography is that—as abiotic and biotic stressestypically result in a decrease in photosynthesis and transpiration—it can be used to detect changes in the physiological status of the plants, thereby revealing spatial heterogeneity that can occur at the individual leaf level [43]. This would allow for rapid measurement of relative temperatures of the canopy and could augment the techniques developed for determining plant vigour (see Section 4).

## 4.2 Frost event measurements

There are two types of frost event: advection frost and radiation frost. Advection frost events are very rare in wine-growing regions of Australia and occur when cold air moves into a region and replaces the warmer air present prior to the change in weather. Such events are associated with moderate to strong winds, no temperature inversion,<sup>6</sup> and low humidity. During these events temperatures often fall below 0°C and remain there for prolonged periods.

Radiation frosts are much more common occurrences, particularly nocturnal ones. Characterised by clear skies, low wind speeds, and temperature inversions, radiation frosts occur because heat is lost in the form of radiant energy, i.e. more heat is radiated away from a vineyard than is received by it, so the temperature drops. Air temperature cools faster near the radiating surfaces (the ground and vines), causing a temperature inversion to occur, i.e. temperature increases with height above ground.

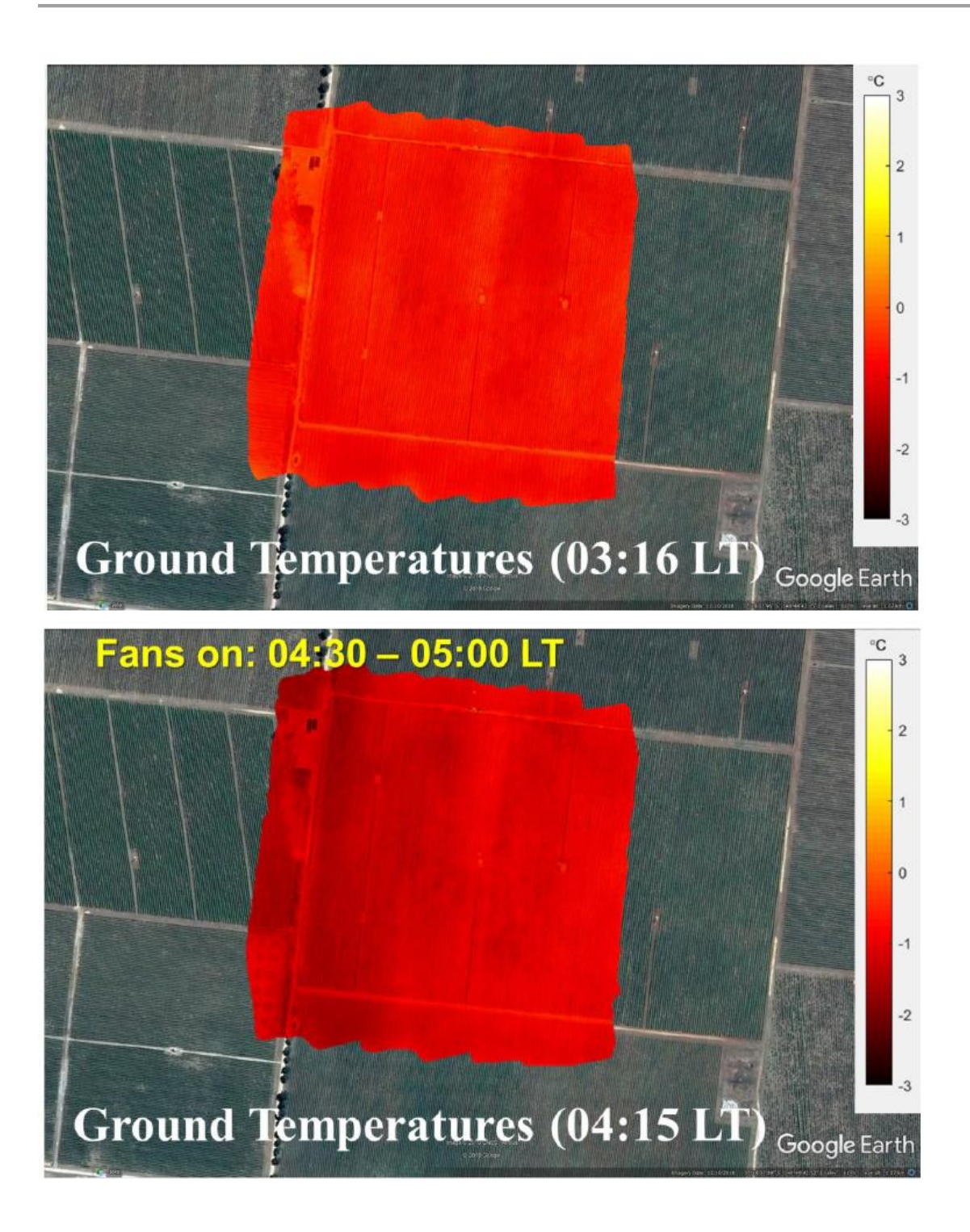
Energy is gained by downward radiation from the sky, by conduction of heat upward through the soil, and by convection of warmer air to colder plants. Wind is a factor because it increases the amount of energy transferred from the air to the vines; and a wind of about 2m/s produces enough convective heat transfer to balance the heat losses. This is the goal behind frost fan protection. Latent heat is only a factor when water is present, so it is generally ignored except when irrigation techniques are used for frost protection.

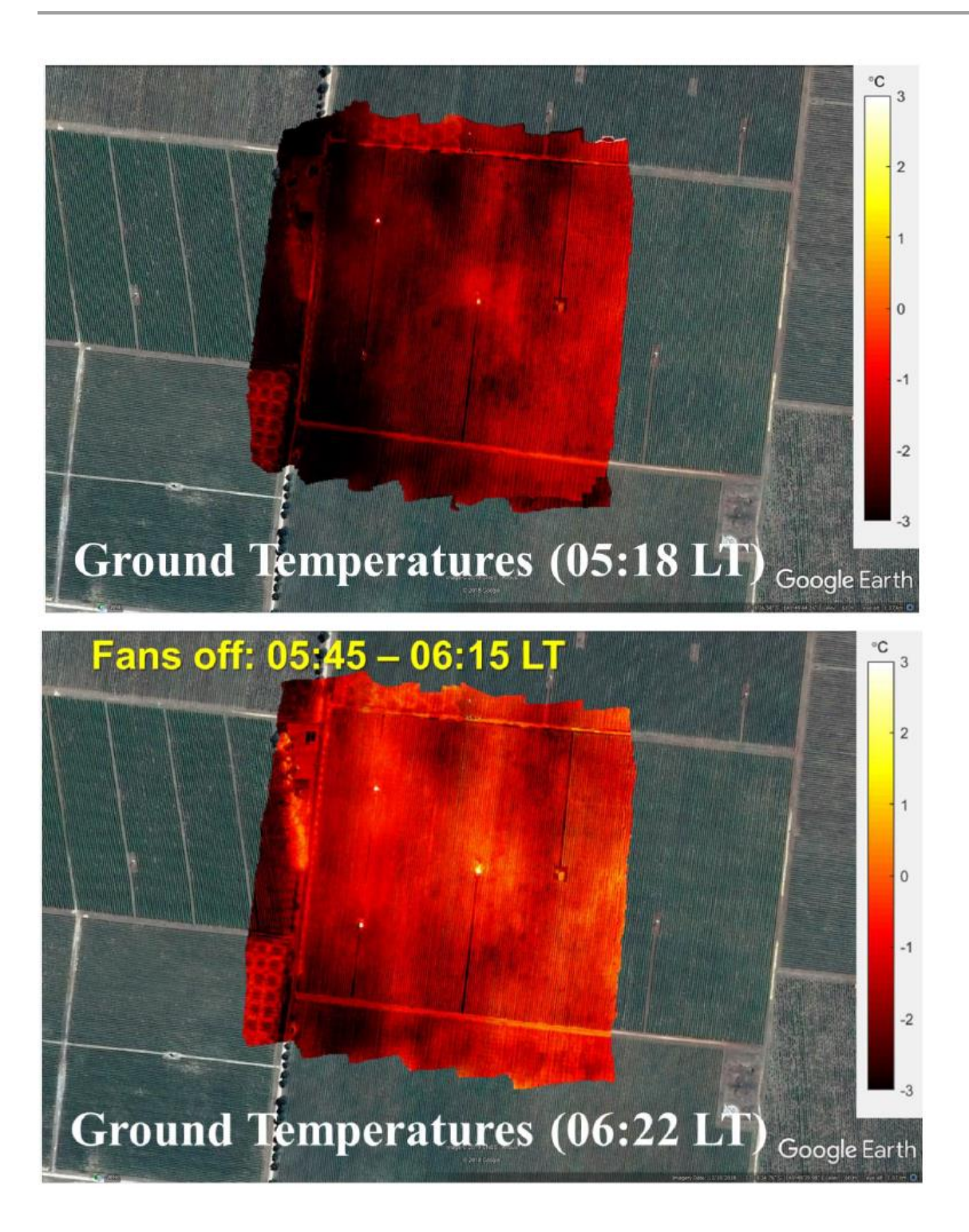
Two frost events were observed in at Wynn's, Coonawarra. During the first event air temperatures fell to around 0°C but frost did not form on the ground or on the vines. During the second event, air temperatures fell to about the same level, but frost did form on the ground. As the vines were close to bud burst during the second event, however, the vineyard managers operated the frost fans to protect the plants from damage. The data for the second event is shown here in three sequences of images (Figure 26, Figure 27, and Figure 28). By way of contrast, the atmospheric data from the first event, which shows a stronger inversion forming, is shown in Figure 29 and Figure 30. It is also notable that, although the data set is smaller, stronger wind conditions around 100m are prevalent, which may well have prevented the formation of frost crystals on the ground surfaces, i.e. the elevated winds provided protection by increasing the downward sensible heat flux density. In other words, they mixed warmer air from higher in the atmosphere with colder air closer to the ground. Examination of such events would not be possible without the technology developed under the program or the establishment and maintenance of masts, which are both very costly and would interfere with meteorological conditions.

The frost fans observed in this imagery are two-blade fans. Their location can be seen in each image as a group of three slightly lighter (hotter) pixels in the centre of the vineyard. They are particularly prominent in images three and four in the sequence, which were taken while the diesel generators driving them were operating. It is apparent, particularly from images three and four, that the fans have provided beneficial impact to the surface temperatures of the vineyard, but that their effectiveness in this regard varies as a function of distance from the fan.

43

<sup>&</sup>lt;sup>6</sup> A temperature inversion is a reversal of the normal behaviour of temperature in the atmosphere near the Earth's surface: a layer of cool air at the surface is overlain by a layer of warmer air. Under 'normal' conditions air temperature usually decreases with height, whereas with an inversion (until the inversion layer is reached) temperature increases.





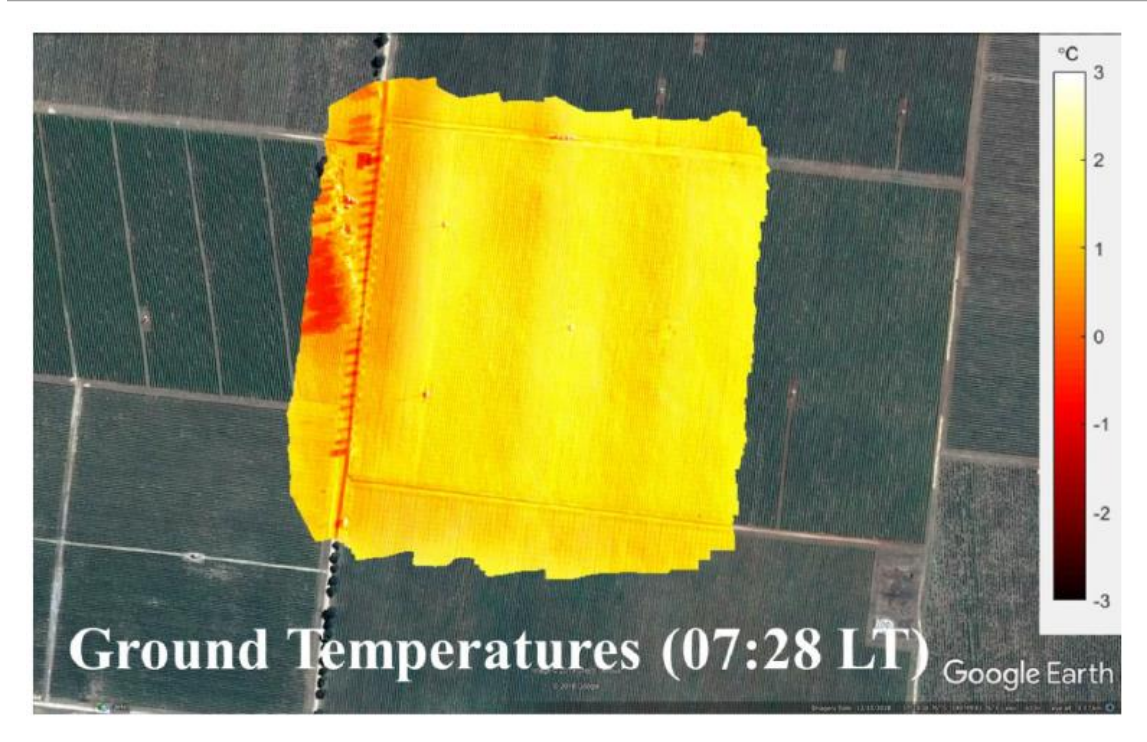
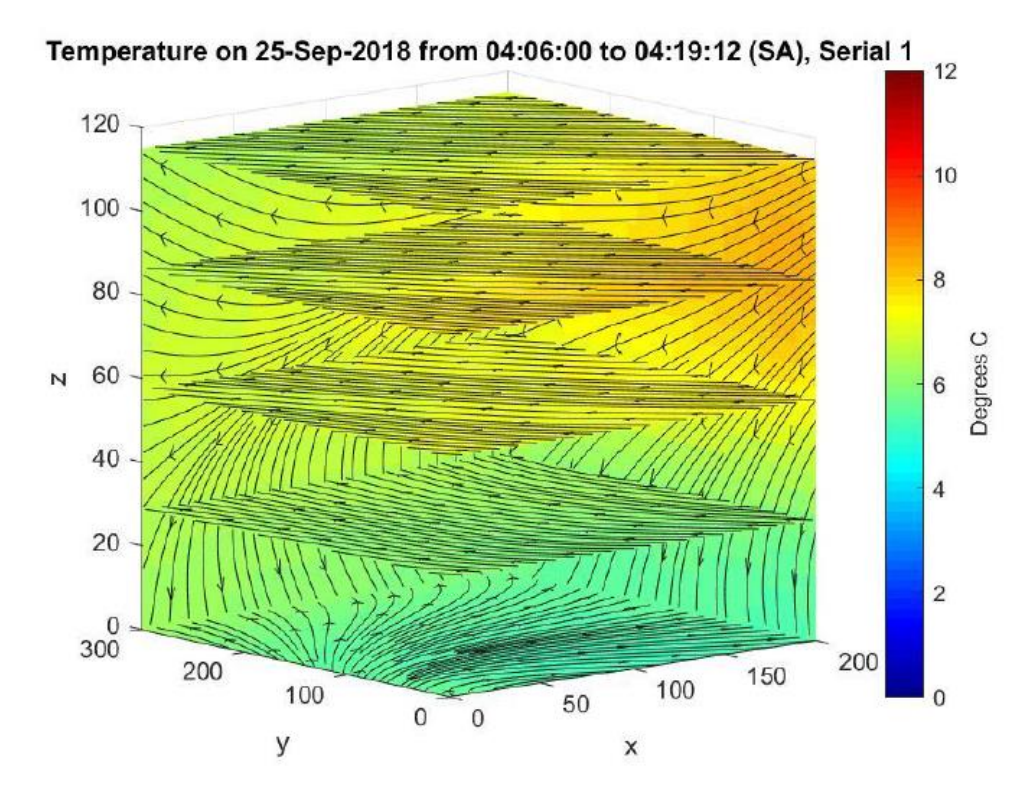
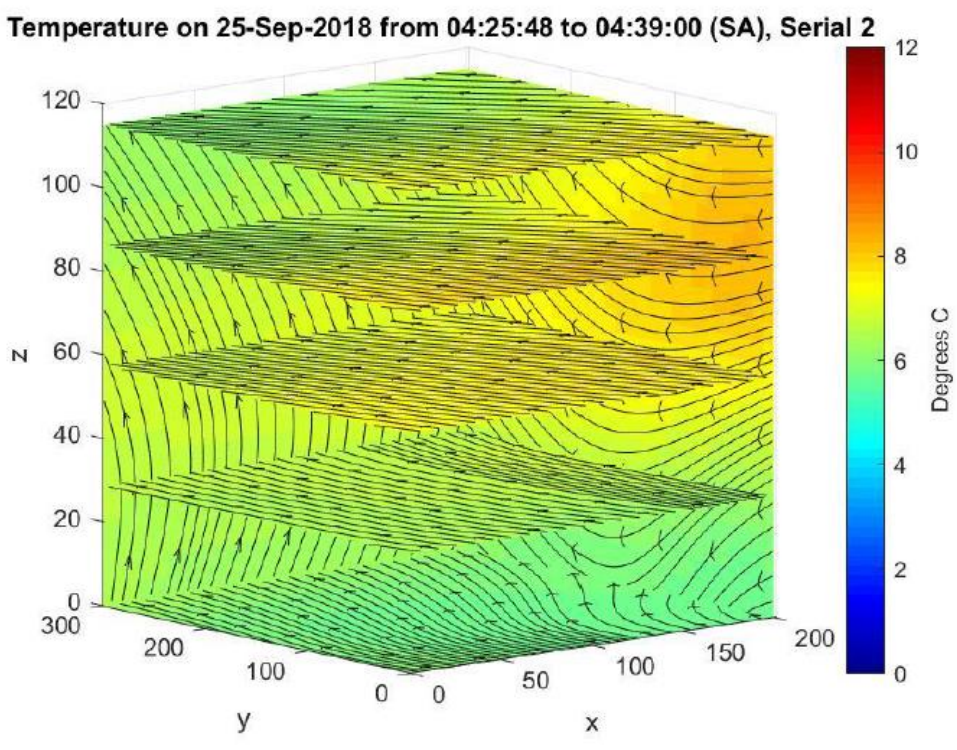


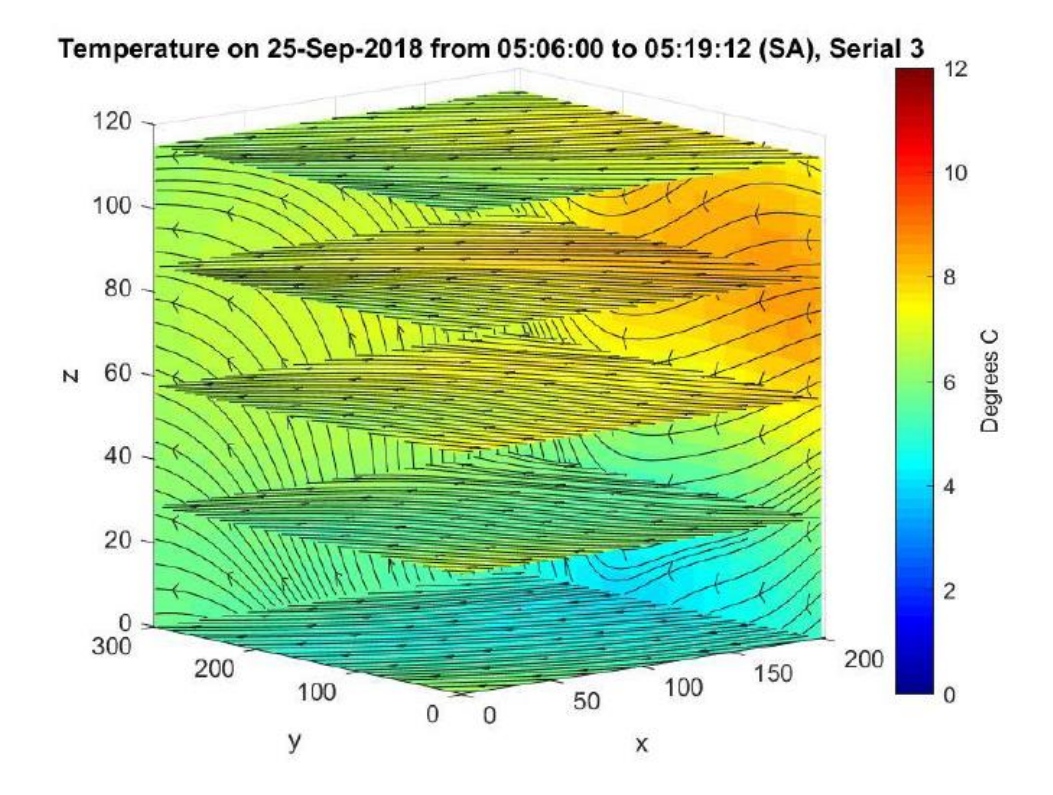
Figure 26:Surface temperatures measured during a Frost event at Wynn's Coonawarra. The local time at which the flights took place are shown on each image and the temperatures are colour-coded in accordance with the bar in the right.

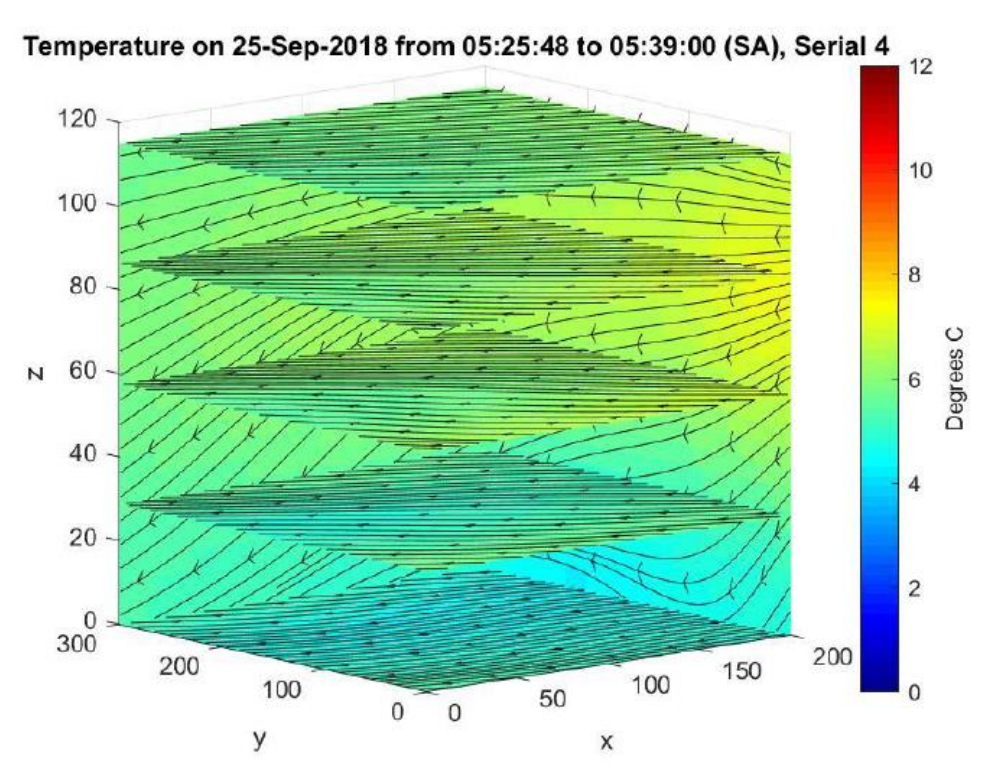
It is noteworthy that a slight elevation in surface temperature persists even post-dawn (image five in the sequence). However, it is not known what the impact of such an effect might be on plant development at this stage of its growth, if anything.

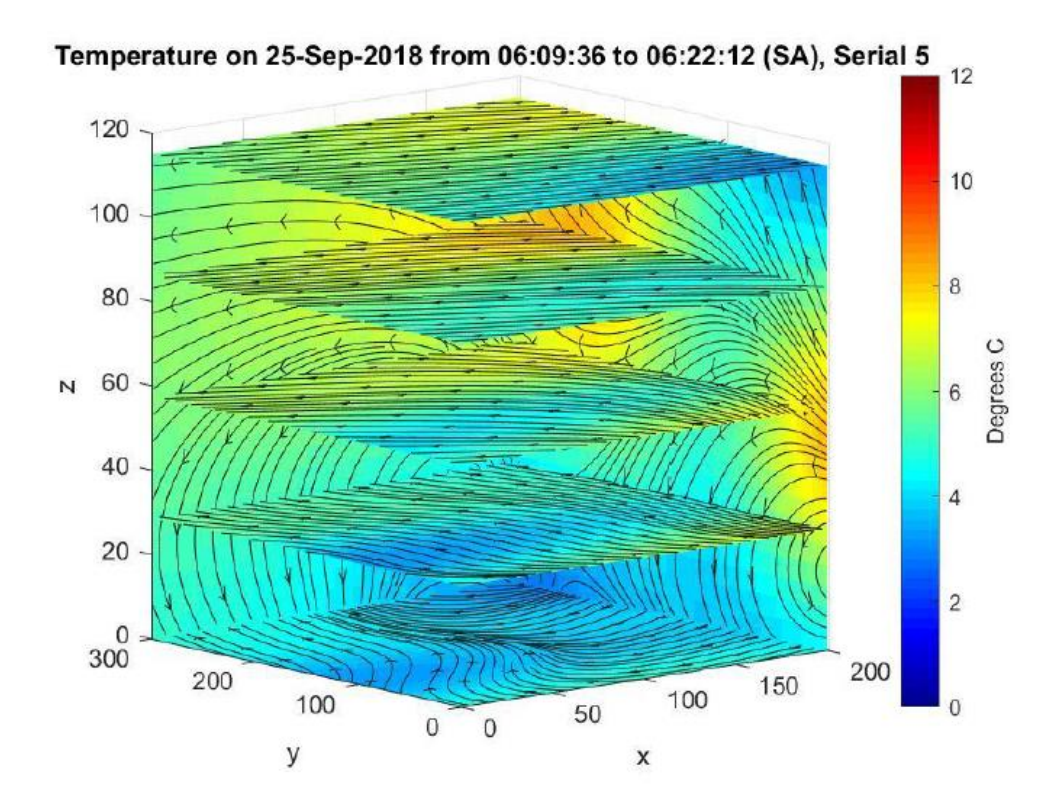
The effectiveness of irrigation frost protection techniques, which were also activated, can also be seen in image sequences three and four. These are the regular patterns of lighter (warmer) temperatures in the lower and upper left of these two images.

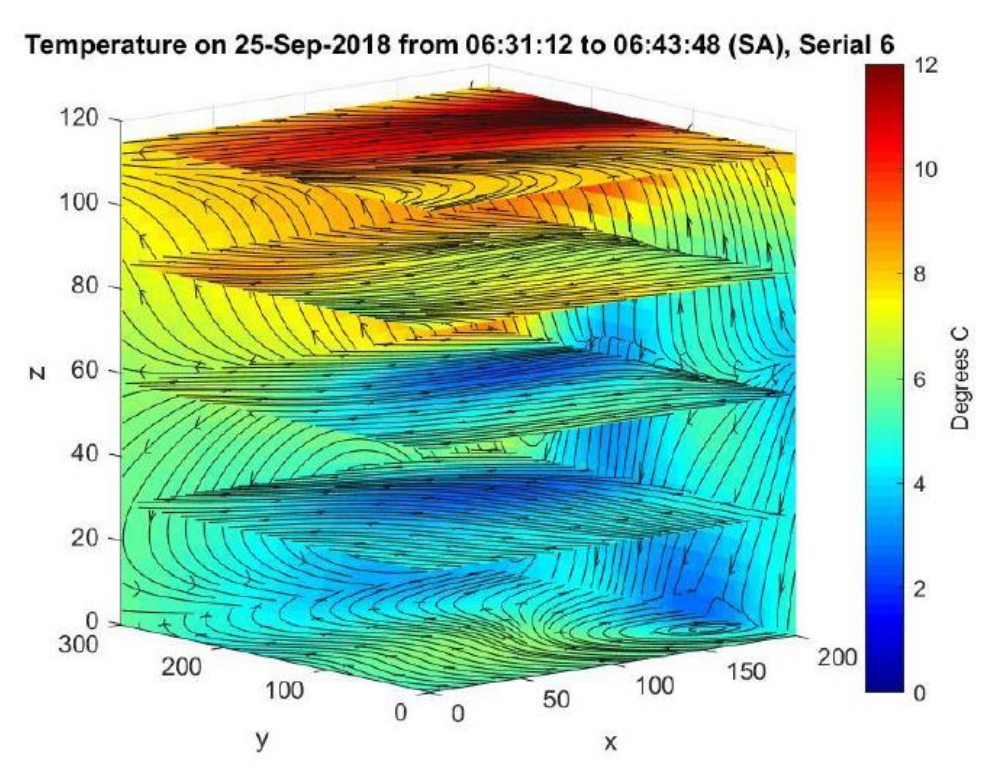


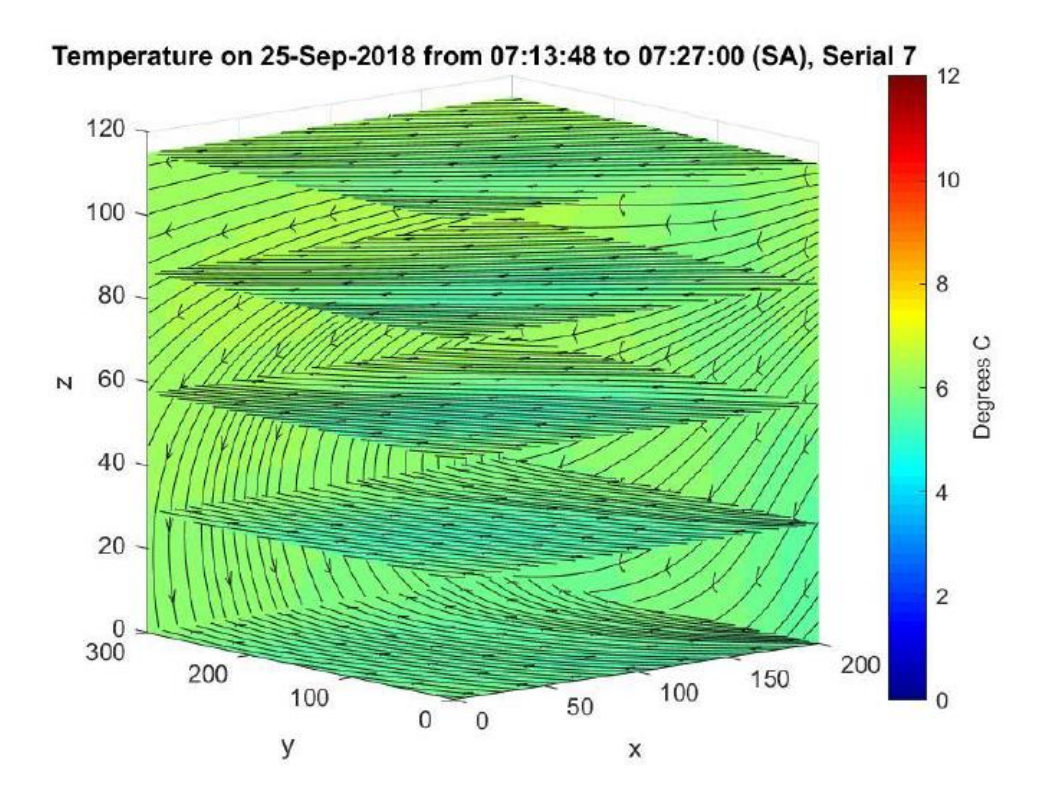












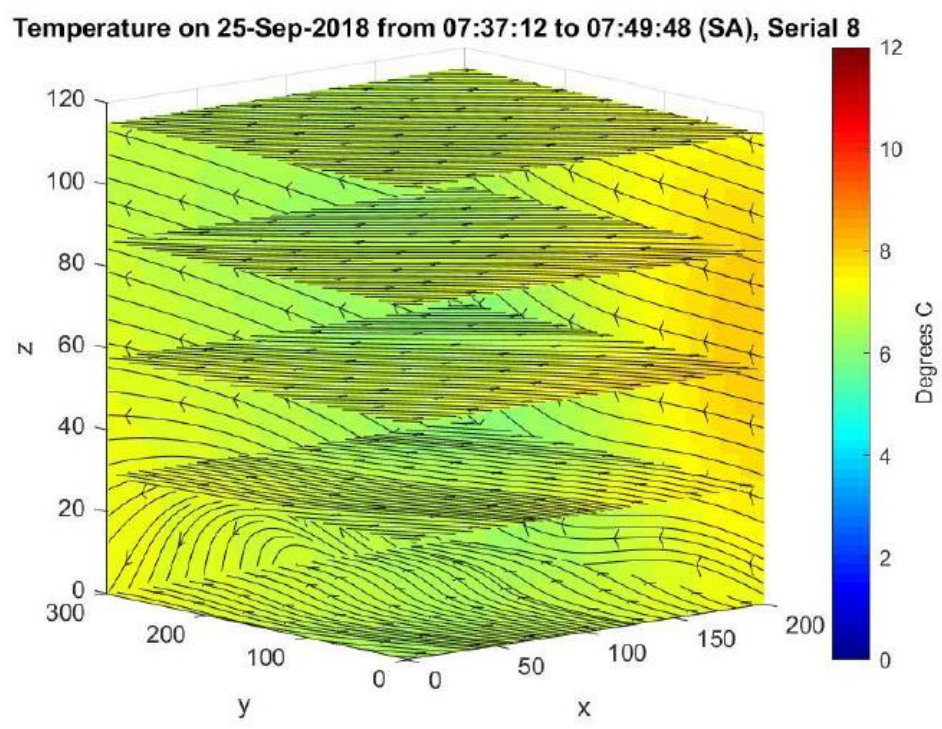
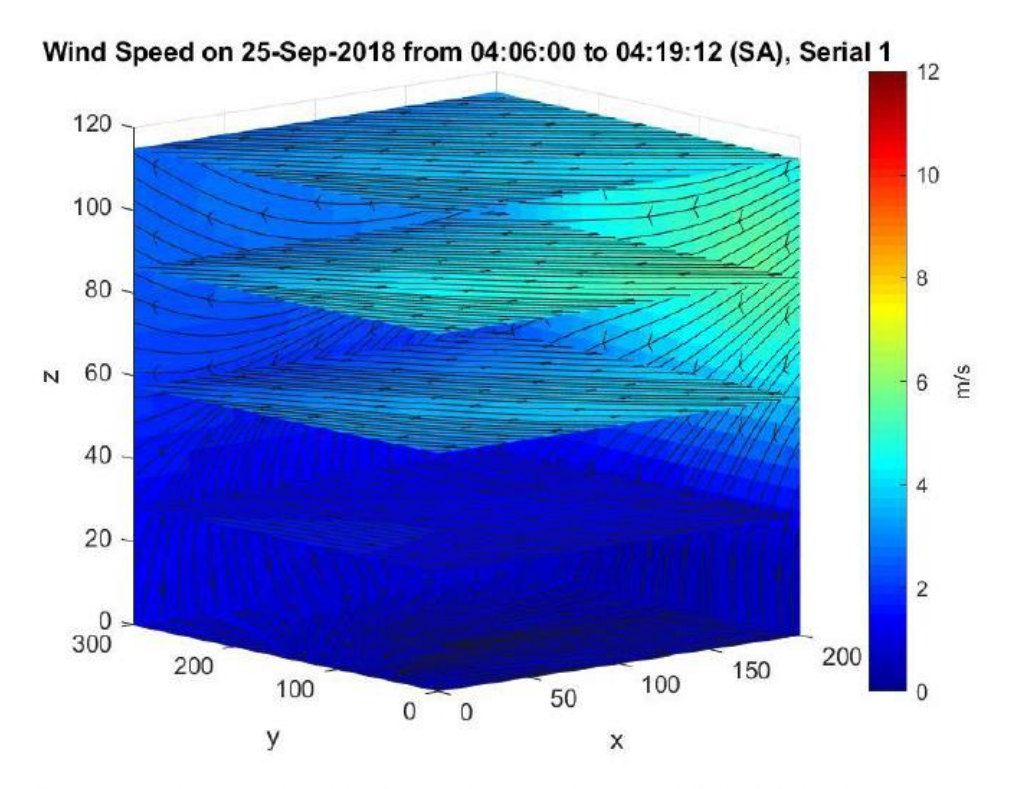
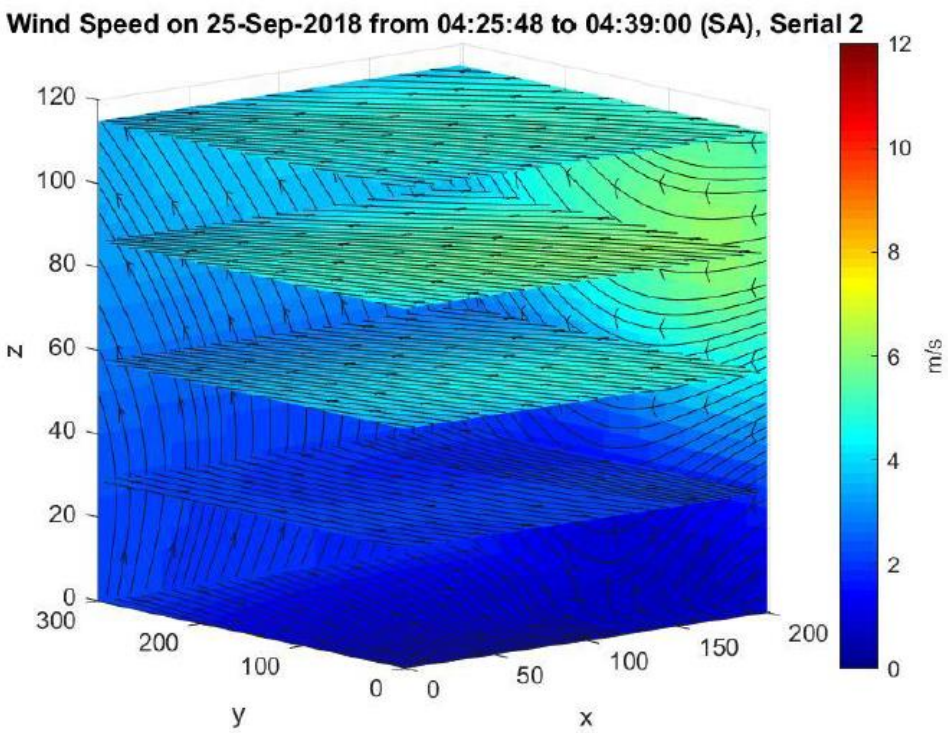
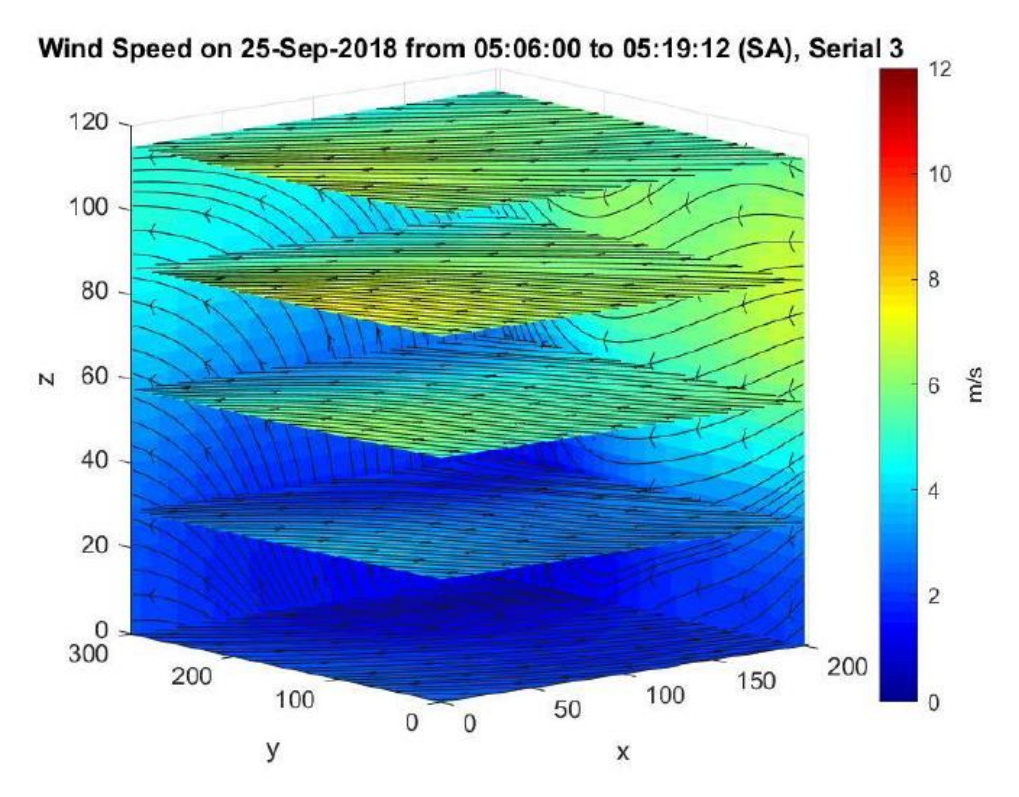
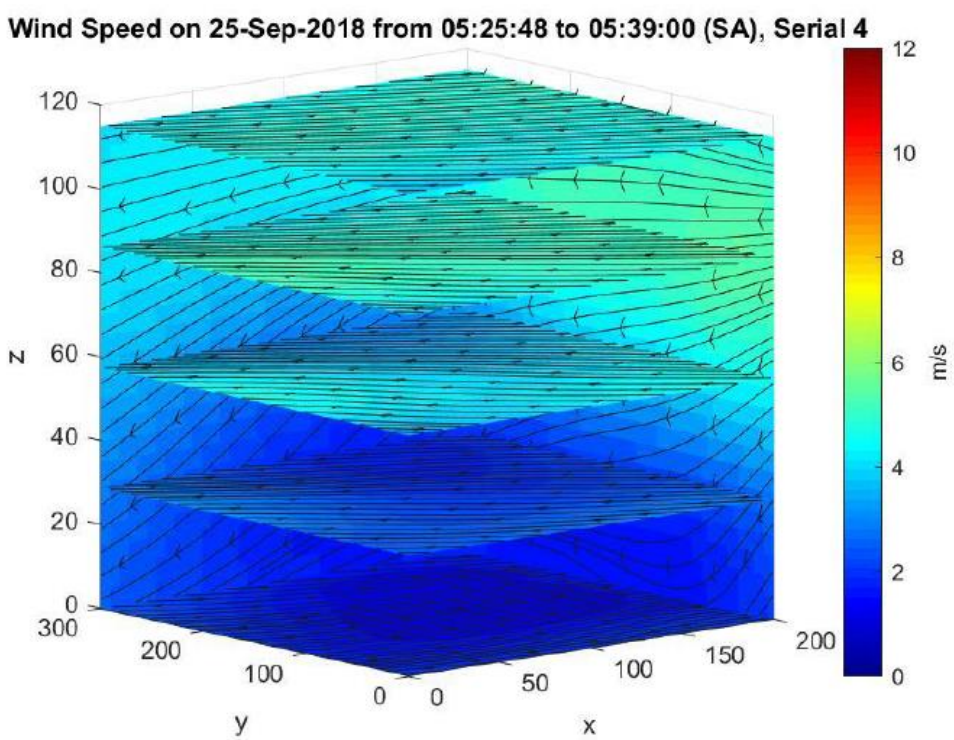


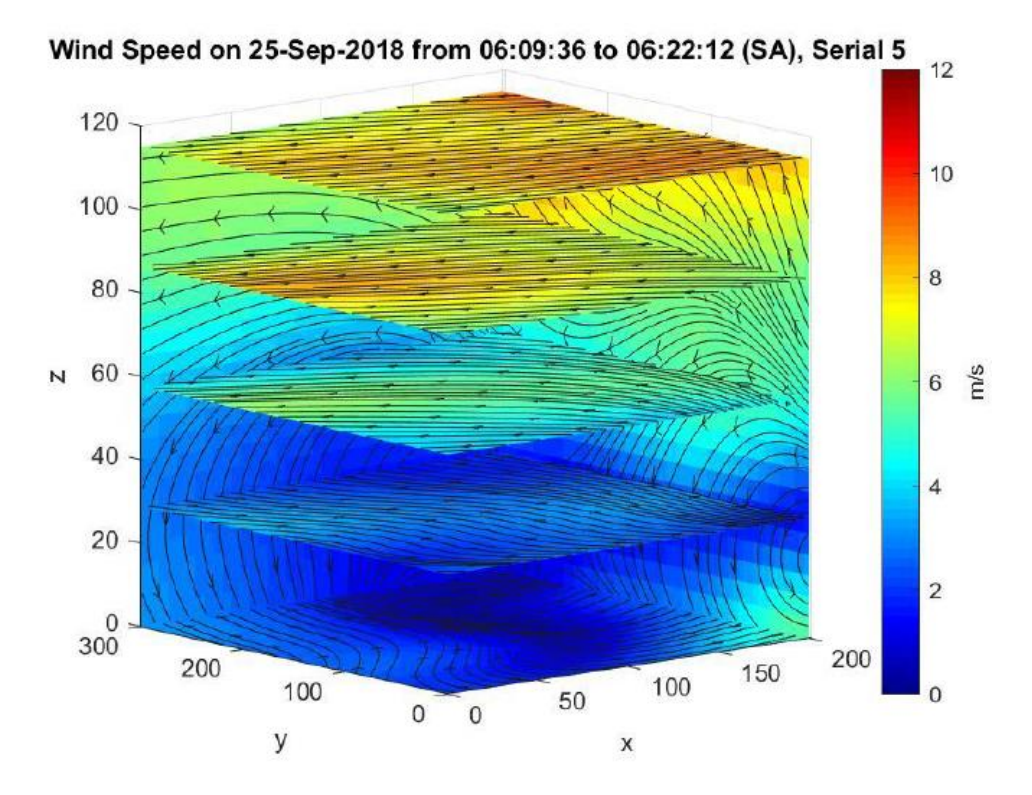
Figure 27: 3D temperature profiles measured during a frost event in Coonawarra. Each image shows temperature for a different time of day, colour-coded in accordance with the bar on the right. Arrows indicate wind direction

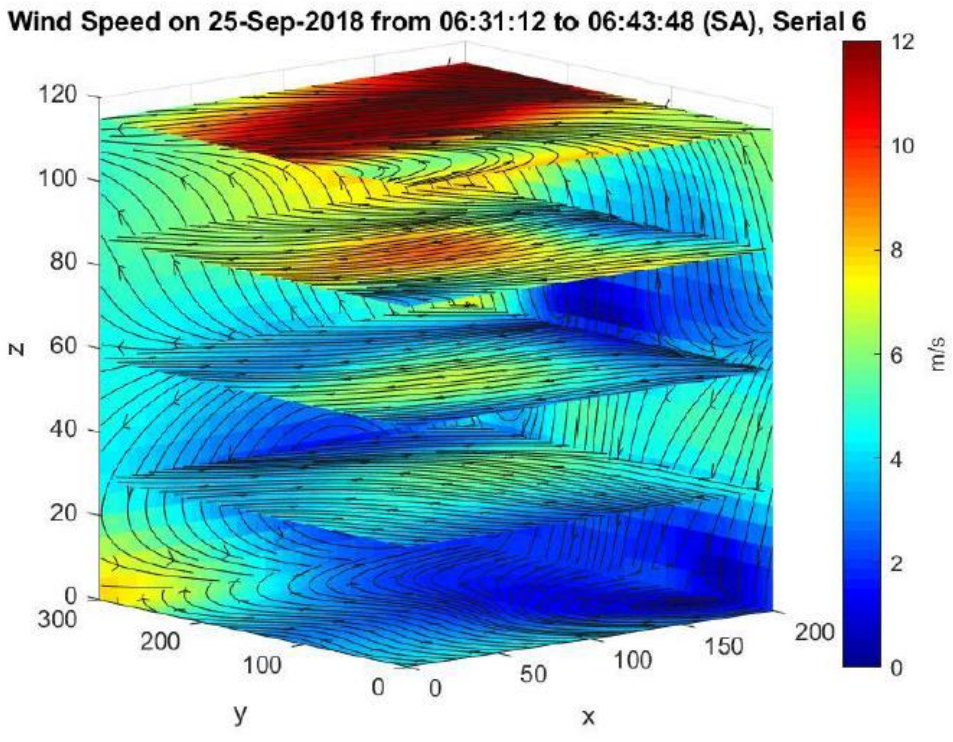


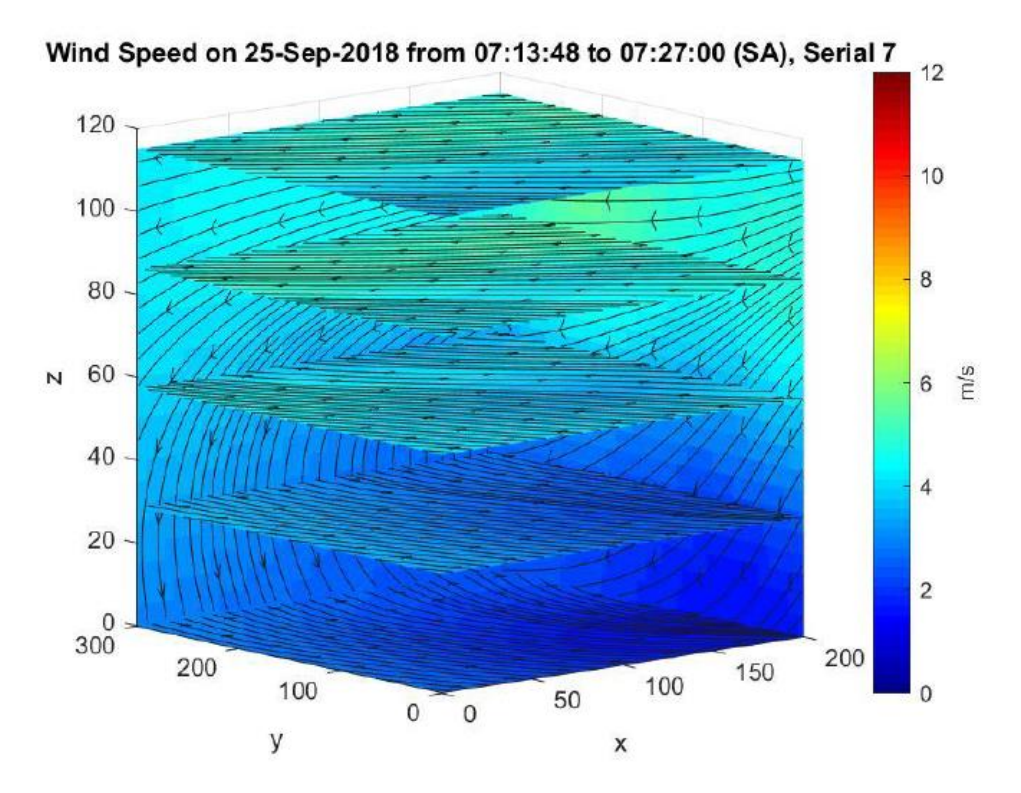


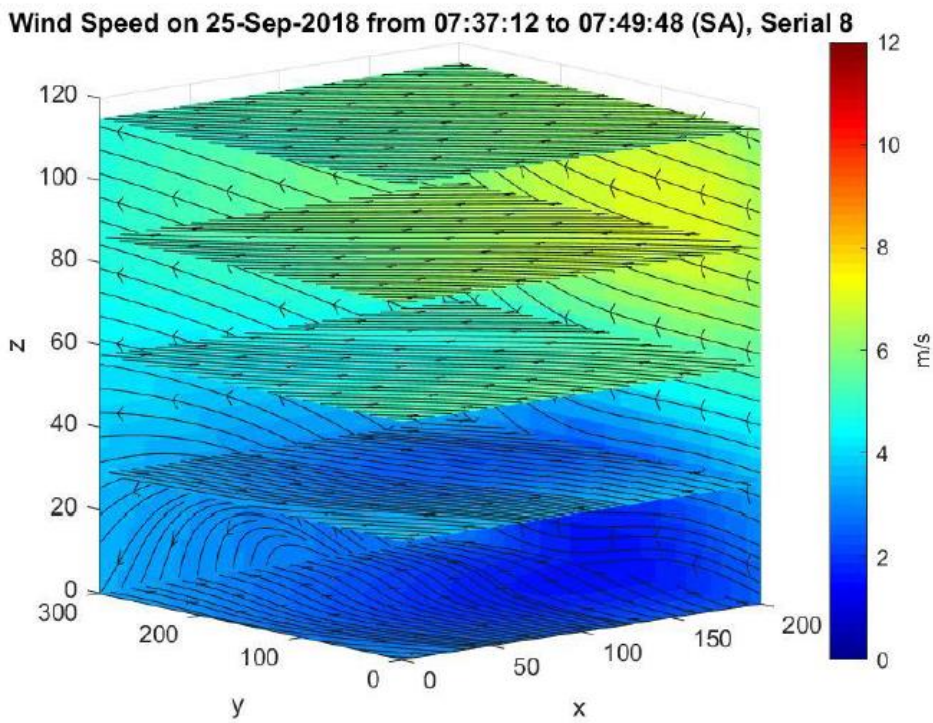




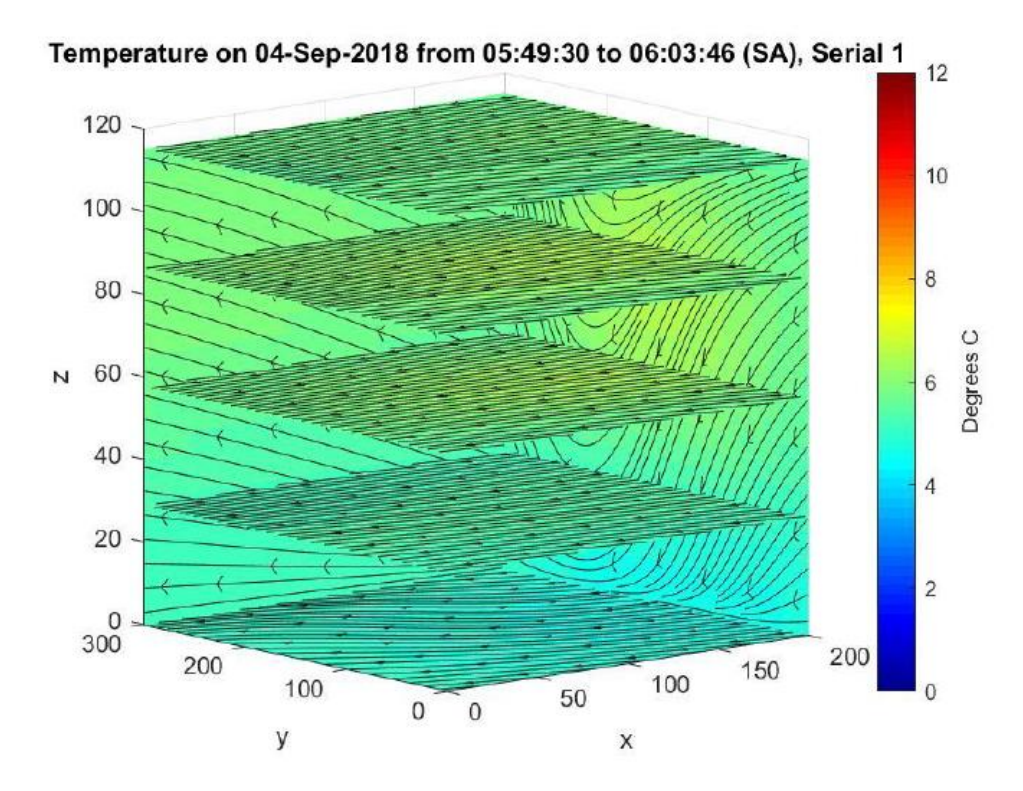


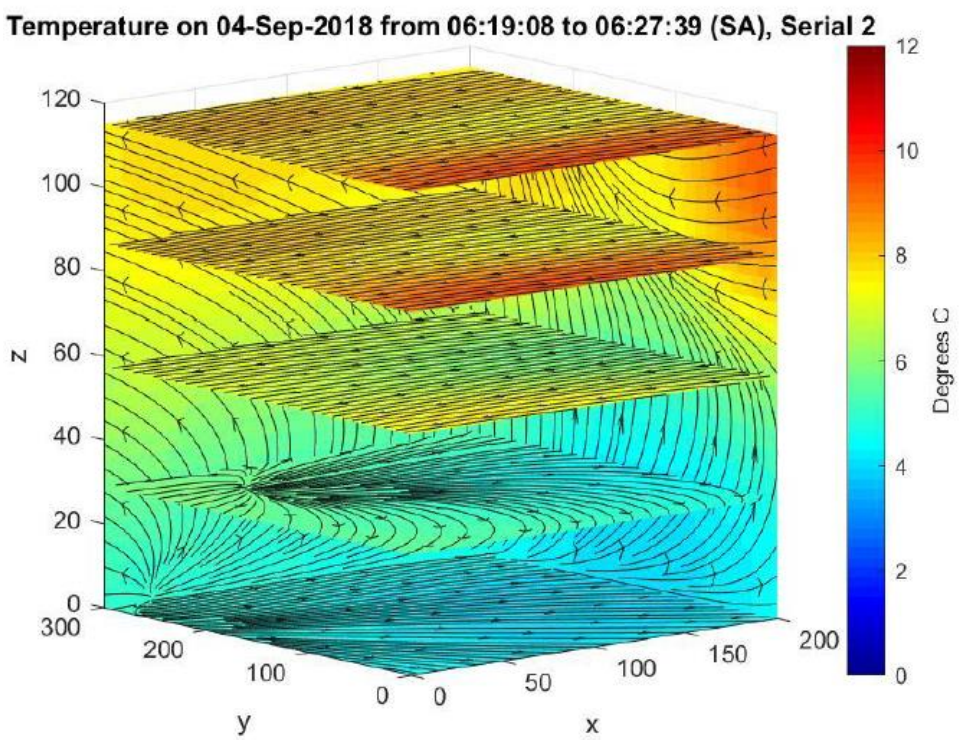


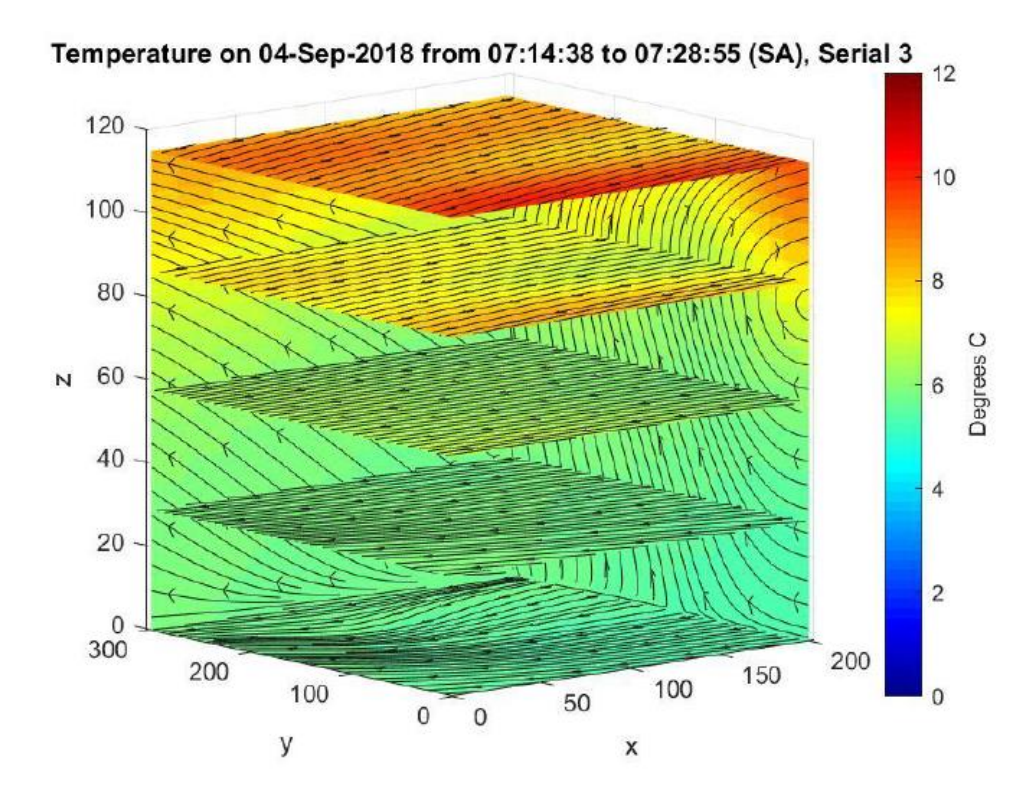




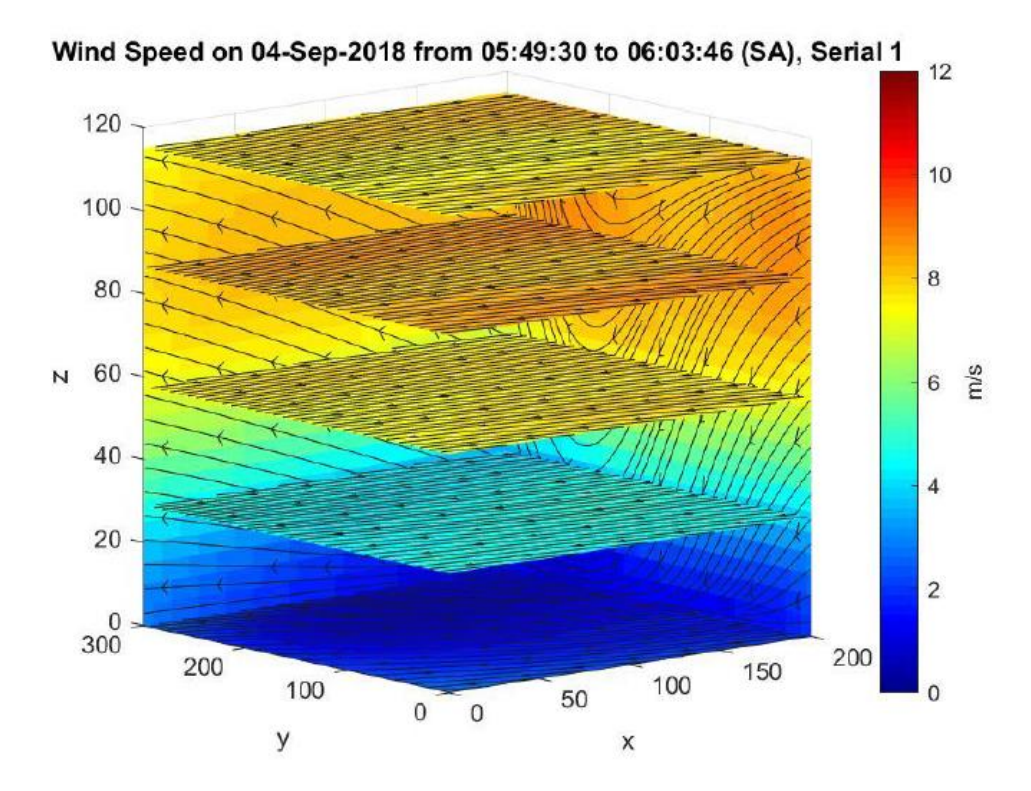
**Figure 28:** 3D wind speed profiles measured during a frost event in Coonawarra. Each image shows wind speed for a different time of day, colour-coded in accordance with the bar on the right. Arrows indicate wind direction.

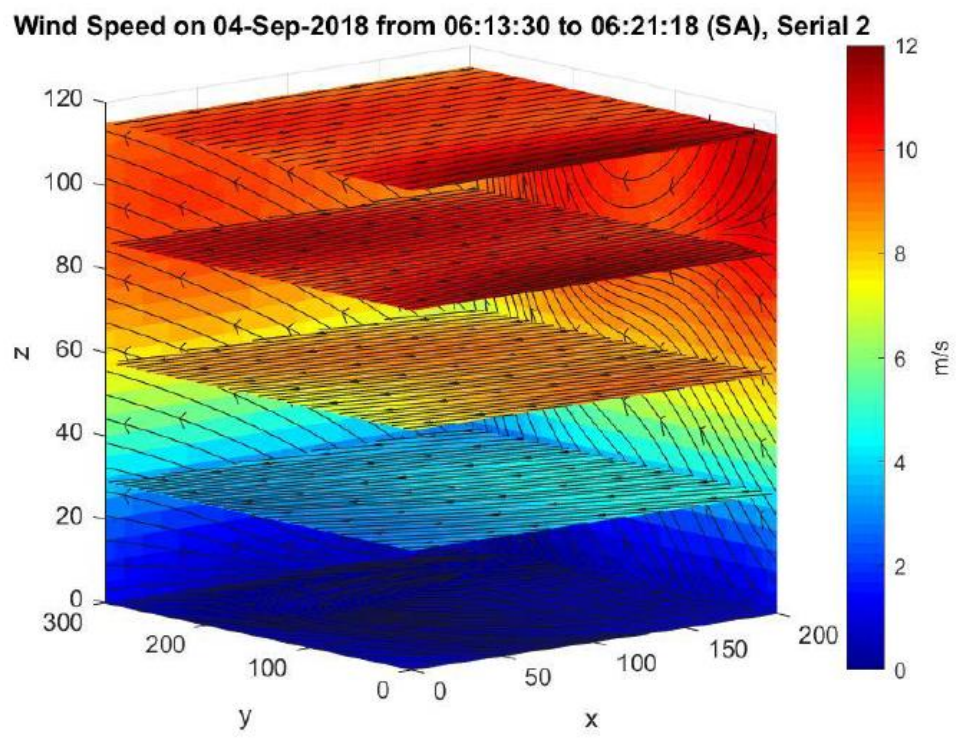






**Figure 29:** 3D temperature profiles measured during a frost event in Coonawarra. Each image shows temperature for a different time of day, colour-coded in accordance with the bar on the right. Arrows indicate wind direction.





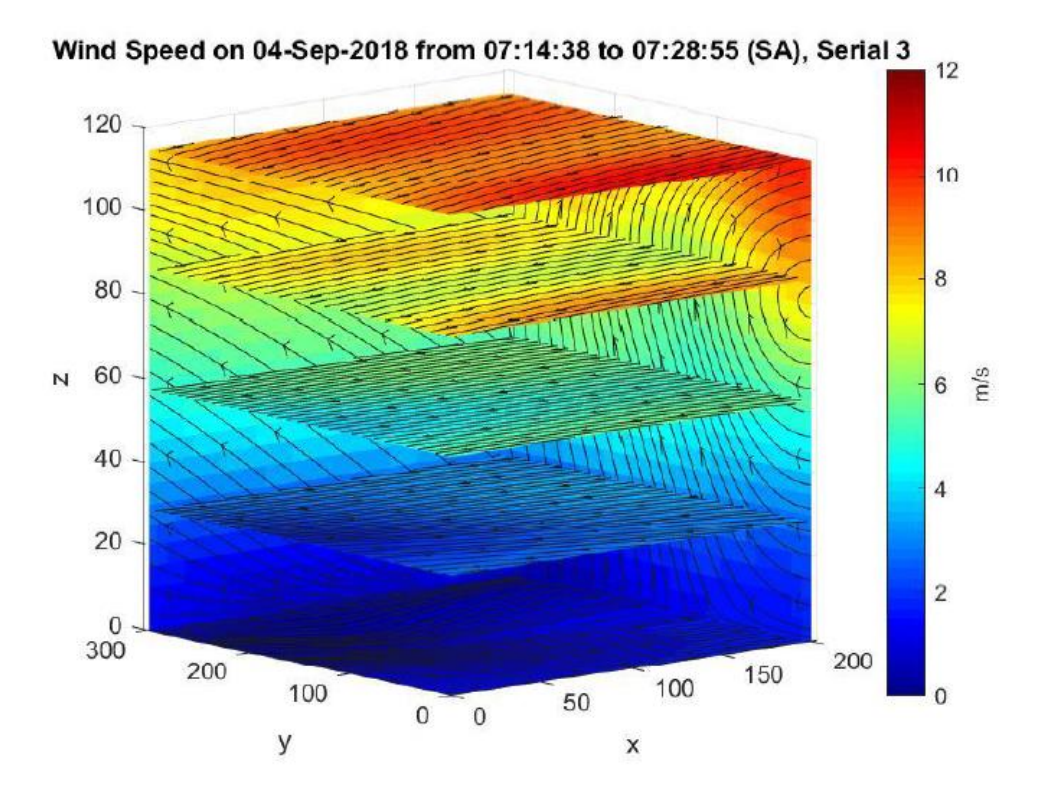


**Figure 30:** 3D wind speed profiles measured during a frost event in Coonawarra. Each image shows wind speed for a different time of day, colour-coded in accordance with the bar on the right. Arrows indicate wind direction.

## 5 Determination of vineyard properties

This component of the technology development was not covered within the milestone schedule is reported due to its potential utility to users. It was developed as a result of the need to determine the differing irradiance properties of the vineyard material. It offers an algorithm that can be used for estimating the structural characteristics of vineyards from remotely sensed dense point clouds (DPC). It requires input of only a single parameter, readily determined by an untrained operator. The algorithm does not require training on specific data sets and is insensitive to complex colour, contrast and lighting variations typically found in the real world. It also copes with noisy and imperfect point clouds generated by sub-optimal UAV flight and camera configurations, as well as the uneven spatial performance of SfM algorithms. It was evaluated under intentionally complex and sub-optimal conditions over a vineyard where green grass is sometimes present between the vines. Its performance strongly suggests it is suitable for application in vineyard decision support tools.

**Introduction:** A key issue in characterisations of vineyard properties is isolation of pixels belonging to the vine rows from those belonging to the spaces in between and elsewhere. Difference in spectral properties between these domains were first attempted by applying a threshold to vegetation indices computed from multi-sensor images [14, 44]. Other researchers have applied Fourier transforms to the red band of the red-green-blue (RGB) classification of images [45-47]. Unfortunately, complex lighting conditions, such as poor contrast, shadow, and glare—as well as the need for spectral contrast between the green of vine rows and the presence of grass between rows—has limited the performance of such methods.

To overcome such shortfalls, a photogrammetric technique known as Structure from Motion (SfM) [28-30] is often used to obtain DPC from the overlapping nature of multiple VIS/RGB images obtained by a UAV. This has been applied to vineyards [48] and other crops [49] to obtain 3D models of terrain and extract fractions of vegetation cover; and to estimate vineyard structure [1]. Unfortunately, while these approaches can discriminate between vines and grass between rows, existing algorithms are sensitive to even slight illumination variations common in real world settings. Additionally, in order to obtain good performance, current techniques need flight configurations and camera settings that are optimised [1].

Methodology: Simple UAV flight paths were executed with aerial observations of the test site made in both the RGB and LWIR components of the electromagnetic spectrum. 3D DPC were generated using SfM and the underlying topography of the surface terrain identified and excised. To enhance computational speed, a Kd-tree [50] partitioned the DPC by recursively splitting it into binary clusters. This allowed a nearest neighbour search to be quickly executed using a bounded data query [51], from which the surface topography was statistically determined. This topographic model was then used to normalise the DPC to a reference surface, whereupon Lloyd's classification algorithm [52] was applied to a combination of height, hue, saturation and irradiance (the latter measured by the LWIR sensor). The clusters were associated using Gaussian probability density functions (PDFs). Finally, the macro-structure and spatial properties of the vineyard (vine vs. inter-row, row height, width, cover fraction and missing row segments) were mapped as spatial functions of vineyard geography.

An overview of the algorithm that computes vine structure is shown in Figure 31. As all mathematical techniques involved are well understood, wherever possible, only verbal descriptions of their function and references to source material is provided in this paper. This is simply to ensure concise narrative.

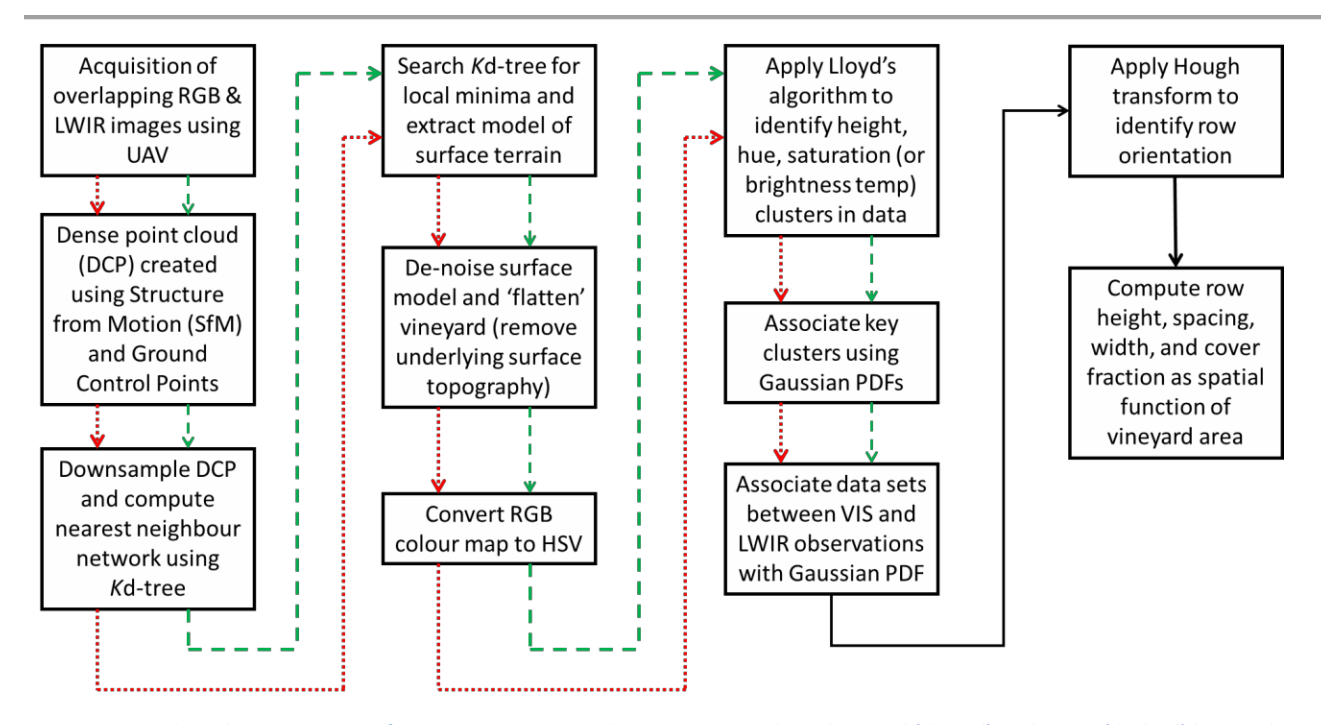


**Figure 31:** Algorithmic overview of vine macrostructure characterisation algorithm. Red (dotted) and green (dashed) lines indicate processes executed sequentially on both VIS and LWIR imagery. The black (continuous) line indicates processes executed on the joint imagery

*Image acquisition:* Field experiments took place at the Jacob's Creek vineyards in the Barossa Valley, South Australia. Visibility was clear, the sky cloudless and air temperatures ranged from temperate (25°C) at about 9.00am to very hot (43°C) at around 3pm local time. These conditions provide regions of dark shadowing, as well as zones of high irradiance and directionally dependent illumination and reflectance: a combination of circumstances that challenge many image processing techniques. Moreover, by judicious selection of observation sets, the thermal conditions were able to offer both a challenging test set for the LWIR data and sound ground truth.

The UAV with the thermographic payload overflew the vineyard at a constant forward horizontal velocity of 10m/s and altitude of 120m in a sequence of opposing parallel lines, oriented along vine row direction (roughly SE-NW). UAV position was determined using standard positioning service GPS (accuracy 3-5m), with altitude obtained using barometric pressure. Separation between each parallel path was about 70m. Images were collected at a rate of 10Hz, but only one in ten images was used, i.e. an effective update rate of 1Hz. SfM flight paths and camera settings were not optimised because, while several automated flight path planners exist for UAVs/SfM, they typically require specialised user knowledge, i.e. skill sets outside those of a vineyard manager. Their use would thus require time-consuming setup and post-processing; and the overarching aim was to avoid the need for users to become expert in the design of UAV flight paths and SfM optimisation; and the goal was to develop an algorithm that was robustness to imperfectly acquired real world data sets, and insensitive to noisy, imperfect, and uneven performance of SfM.

The UAV carried the gimbal-mounted thermographic payload described earlier in this document, so it had a roughly 60° field of view, and about 85% and 50% overlap between images in the along- and across- track directions, respectively. This allows coverage of a 10Ha vineyard in about 3 minutes with a ground sampling distance of about 10cm. The vine canopies were approximately 1.5m high. They are not pruned, and terrain undulates slightly over the roughly 10Ha area of the test site, varying by around 12m from

lowest to highest points. Every tenth LWIR image was used to generate a DPC. Moreover, observations were taken at about 10.00am, providing only modest contrast between leaf and ground irradiances; and, as the sun has not yet reached its zenith, the vines create significant shadowing (cooler regions). Both circumstances were designed to challenge the vine segmentation algorithm.

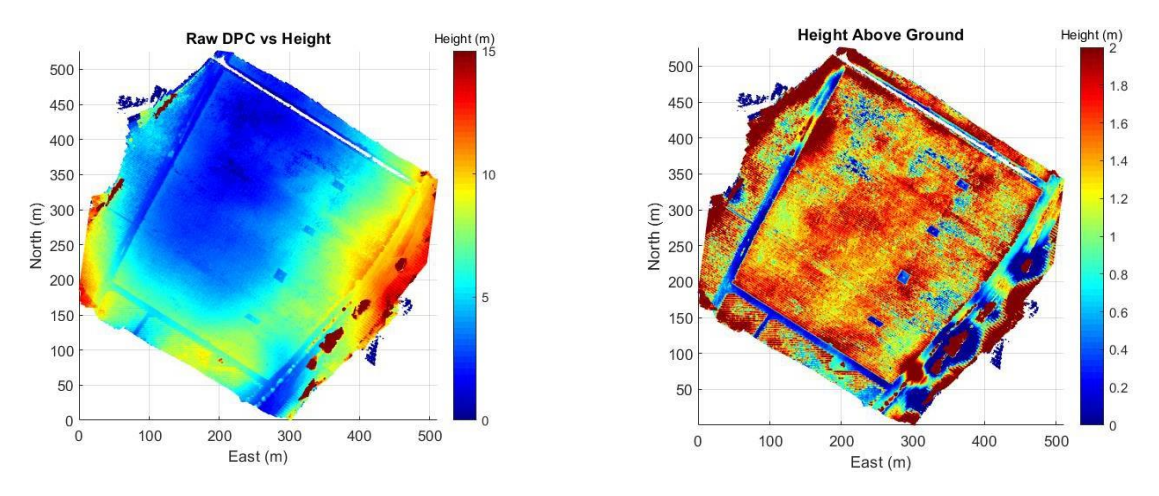


Figure 32: Variation of height for Jacob's Creek test site (left) prior to removal of surface topography and (right) afterwards (note change of scale between images)

The VIS DPC of the vineyard generated by SfM in this way contains around 35 x 10<sup>9</sup> points, which are randomly, but approximately homogenously, arranged throughout the 10Ha vineyard [Note: computation may be significantly enhanced, without great loss of accuracy, if the DPC is downsampled using interpolation based on grid averaging]. The LWIR DPC was also generated using SfM, with the image stack colour-coded according to temperature. The lower resolution of the LWIR imager results in a noisier and more distorted DPC as—in addition to generating camera location and orientation—the SfM process also estimates distortion created by the camera lens, which is more difficult for an LWIR sensor [53].

Compute model of surface terrain (nearest neighbour network using Kd-tree): As the underlying topography of the terrain varies in altitude by approximately 12m over the vineyard, in order to use height as a discriminator for vine vs. inter-row material (both of which can be similar in colour), the surface topography must first be identified and vine height computed relative to this. Furthermore, as SfM can be an imperfect, noisy technique, vineyards with more subtle topographic variations generally represent greater challenges for height identification algorithms. This is because noise or inaccuracies in the DPC represent larger errors in relative terms, presenting greater challenges for clustering and association algorithms later in the processing chain.

To ensure computational tractability, data is down-sampled by a factor of 100 and a Kd-tree [54] used to partition the DPC by recursively splitting it into clusters. This allows a k-nearest neighbour (k-NN) search to be quickly evaluated on sub-blocks of the data using a query bounded by a circle of radius 5m. This in turn enables the approximate surface topography to be determined by finding the local minimum for each point queried in the k-NN search. The influence of outliers is minimised using a technique devised by [55].

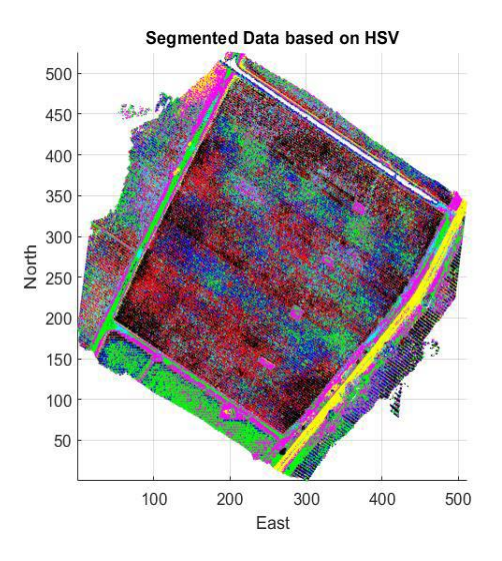
After resampling back to original ground resolution using 2D spline interpolation, with Golay filtering [56] applied to reduce noise, the complex 3D reference ground plane is subtracted from the original DPC height data to normalise ('flatten') the point cloud (Figure 4 right). Points lower than 0m are set to this value. It

is recognised that grass growing between the rows may result in an elevated reference plane, and thus lower estimates of vine heights in some regions of the vineyard.

Cluster vineyard properties using Lloyd's algorithm: In addition to normalising vineyard height, prior to clustering the colour properties of the VIS DPC are transformed from RGB to hue-saturation-value (HSV). The 2D circular scale of hue and saturation better enables colour properties to be associated than the linear RGB representation. The value component of the HSV scale is ignored as the degree of illumination can vary dramatically across a strongly sunlit vineyard. In the case of the LWIR sensor data, surface temperature is colour coded from minimum to maximum and thus clustered in terms of its HSV representation (with its value component again ignored).

Lloyd's algorithm, also known as k-means clustering, is then applied separately to the normalised height, irradiance and HS values of the two DPCs. Lloyd's algorithm is an iterative, data-partitioning (sometimes also referred to as unsupervised machine learning) technique that assigns observations to one of k clusters defined by centroids, where k is chosen before the algorithm starts. We typically used k = 7 for each category, finding results to be largely insensitive to values higher than this.

Lloyd's algorithm operates as follows: (i) point-to-cluster-centroid distances for all observations to each centroid are computed; (ii) each observation is associated to the cluster with the closest centroid [note: observations can be individually assigned to a different centroids if the reassignment decreases the sum of the within-cluster, sum-of-squares point-to-cluster-centroid distances]; (iii) the mean of the observations in each cluster is computed to obtain k new centroid locations; (iv) steps (i) through (iii) are repeated until cluster assignments do not change, or the maximum number of iterations is reached. Figure 5 shows the outcome of the algorithm, colour-coded by cluster.



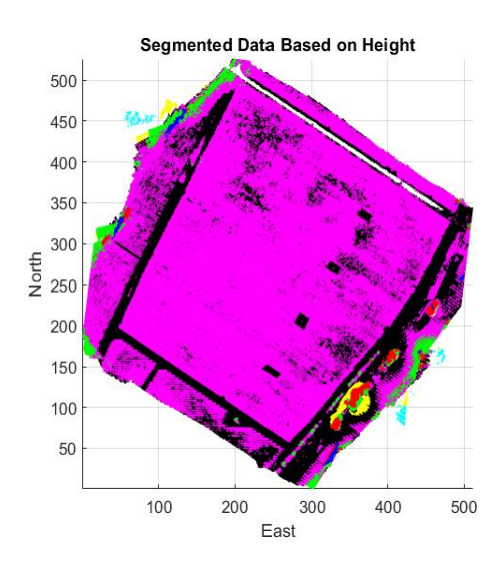
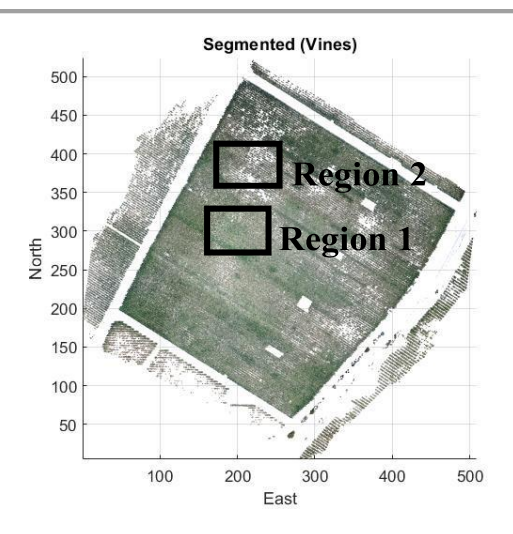


Figure 33: Outcome of Lloyd's classification, colour-coded (left) by HSV and (right) height. Colour represents elements of the DPC identified with each cluster.



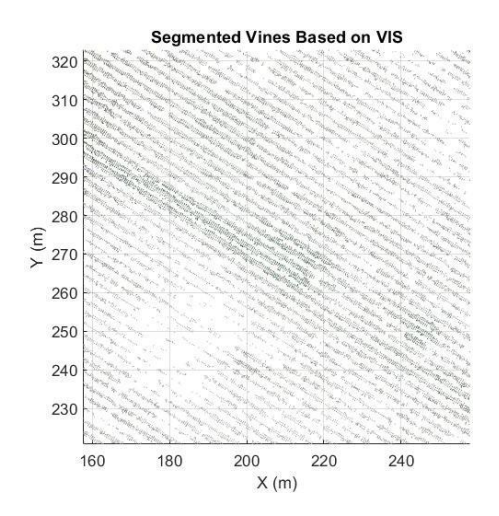


Figure 34: Result of vine identification algorithm using VIS data alone (left) and (right) close-up of Region 1.

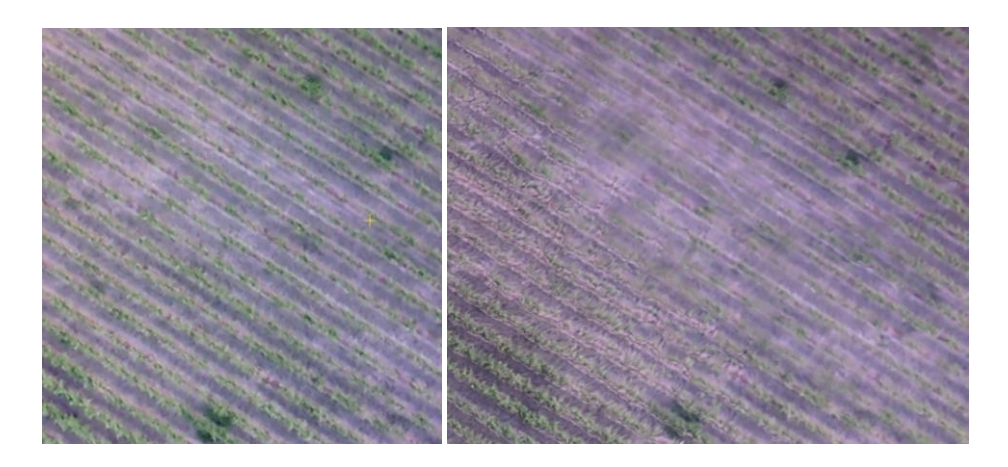
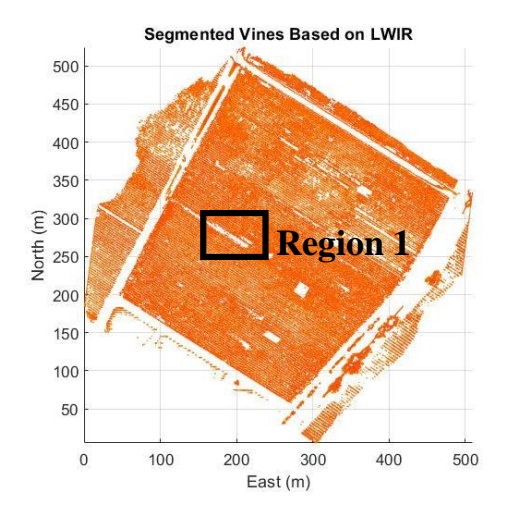


Figure 35: Expanded view of the raw imagery (left) and DPC (right) of Region 2 (Figure 6)



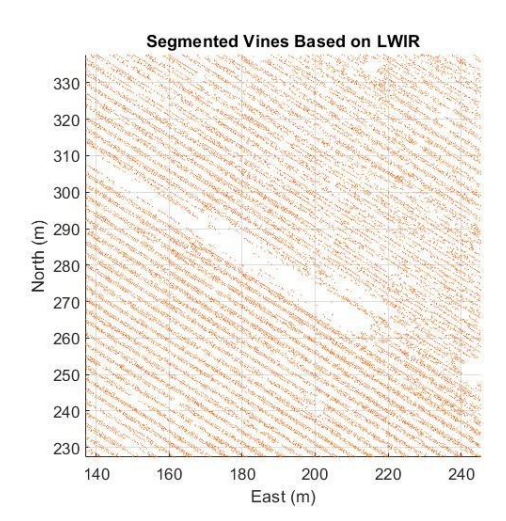


Figure 36: Vine identification based on LWIR data alone for the entire vineyard (left) and an expanded area (right)

| Ise o | f Unmanned Air Vehic       | es for Far  | lv Detection o | f Fxtreme   | Weather Events    | in Vine   | vards |
|-------|----------------------------|-------------|----------------|-------------|-------------------|-----------|-------|
|       | i Ollillallica Ali vellici | .5   OI LUI | I Detection o  | I LALICITIC | VVCGLIICI LVCIICS | III VIIIC | yuius |

Associate clusters using Gaussian PDFs: It is clear from the above images that, on its own, k-means clustering does not successfully identify vineyard properties in terms of either height or colour. We thus apply a priori knowledge to the height data, assuming that vines are less than 2m tall. The results of the height clustering are therefore ordered from smallest to tallest and the most significant cluster with a Lloyd's centroid less than 2m assumed to be that most likely to contain the bulk of the points containing vine foliage. Based on Bayesian association, the colour (irradiance) cluster most associated with this height cluster is then declared the most likely vine colour (irradiance).

A series of Gaussian PDFs are then established such that  $p(v_{VIS}) = e^{-\alpha^2/\mu_H^2} e^{-\beta^2/\mu_N^2}$  where  $p(v_{VIS})$  the probability that any given VIS point is a vine,  $\alpha$  and  $\beta$  are the point-to-centroid distances in the height and colour clusters, and  $\mu_H$  and  $\mu_C$  are the mean point-to-centroid distances obtained for the height and colour clusters declared in the previous paragraph. The process is then repeated for the LWIR DPC and  $p(v_{LWIR})$  computed.

The VIS and LWIR clusters, which are co-registered to the same coordinate system, are fused using a joint PDF,  $p(v_{loint}) = p(v_{VIS}) + p(v_{lWIR}) + p(v_{lWIR})^2/\sigma_d^2$ , where  $X_{VIS}$ ,  $X_{lWIR}$  are coordinates of the

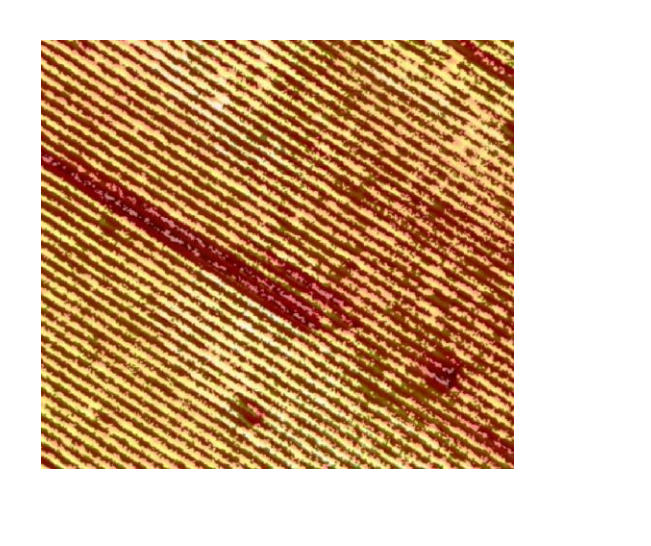
points identified as vines using the VIS and LWIR data sets, respectively, and  $\sigma_d$  the root mean square value of the vine width derived from the VIS data.

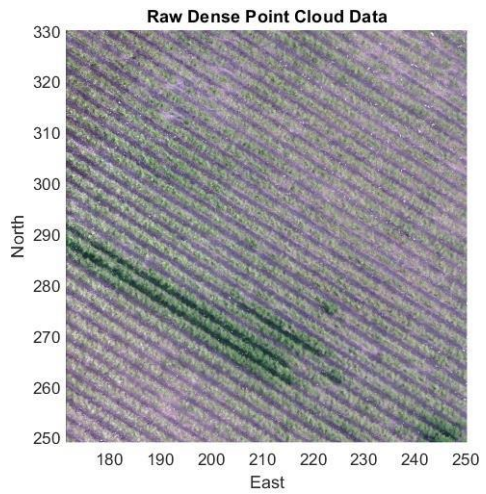
A threshold,  $p(v_{Joint})_T$ , is set, such that joint probability estimates,  $p(v_{Joint}) > p(v_{Joint})_T$ , are declared vine material. This is the only parameter that need be set by a user, and which is readily adjusted based on objectively viewing the degree of contamination by the background, i.e. roads, trees, bushes, etc.

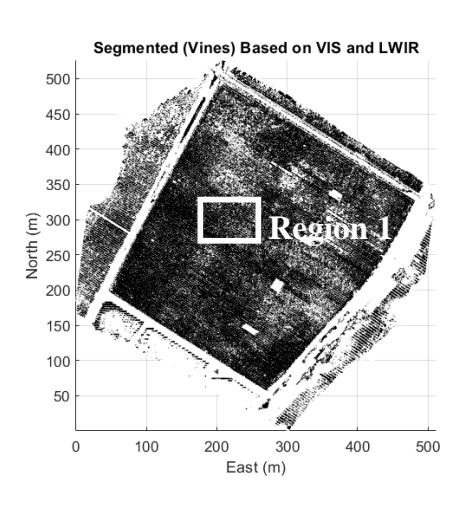
Assessment of segmentation performance: The results of the approach when applied only to the VIS DPC are shown in Figure 34, with an expanded view (Region 1) of an area where an irrigation pipe has ruptured shown in Figure 34, right. This region has a combination of significant green inter-row material, much more vigorous vine growth, shadowing caused by extended vine growth, and varying hue from strong sunlight. Despite this, the algorithm has correctly identified only vine material.

There are also patches of vineyard where the algorithm has failed to correctly identify vine material, e.g. Region 2. While the algorithm suggests a complete absence of vine material, a better interpretation is that the plant density has fallen below a threshold ground resolution required by the SfM. This is confirmed by examination of the raw imagery (Figure 35), which shows the sparsity to be largely due to poor performance of the SfM (noting it was intentionally provided imagery gathered under sub-optimal conditions to show performance under these circumstances). The image on the left of Figure 35 shows an expanded view of the raw VIS imagery observed onboard the UAV. This shows the vine material in this region, albeit thinner than in other areas of the vineyard. The image on the right of Figure 35 shows SfM output, where distortions in the resultant DPC have obscured the sparser vine material and resulted in a much flatter 3D structure than truly exists. As a result, these sparser segments of the vineyard have been identified as ground material.

The results of LWIR-only segmentation are shown in Figure 36. As with VIS-only outcomes, due a combination of poor height determination by the SfM and slightly cooler surface temperatures in the more densely vegetated areas, performance is imperfect in areas such as Region 1.







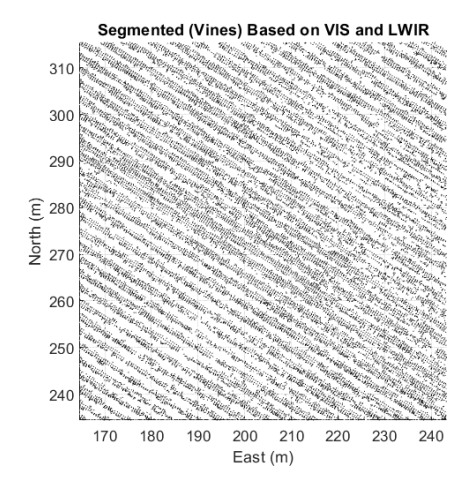
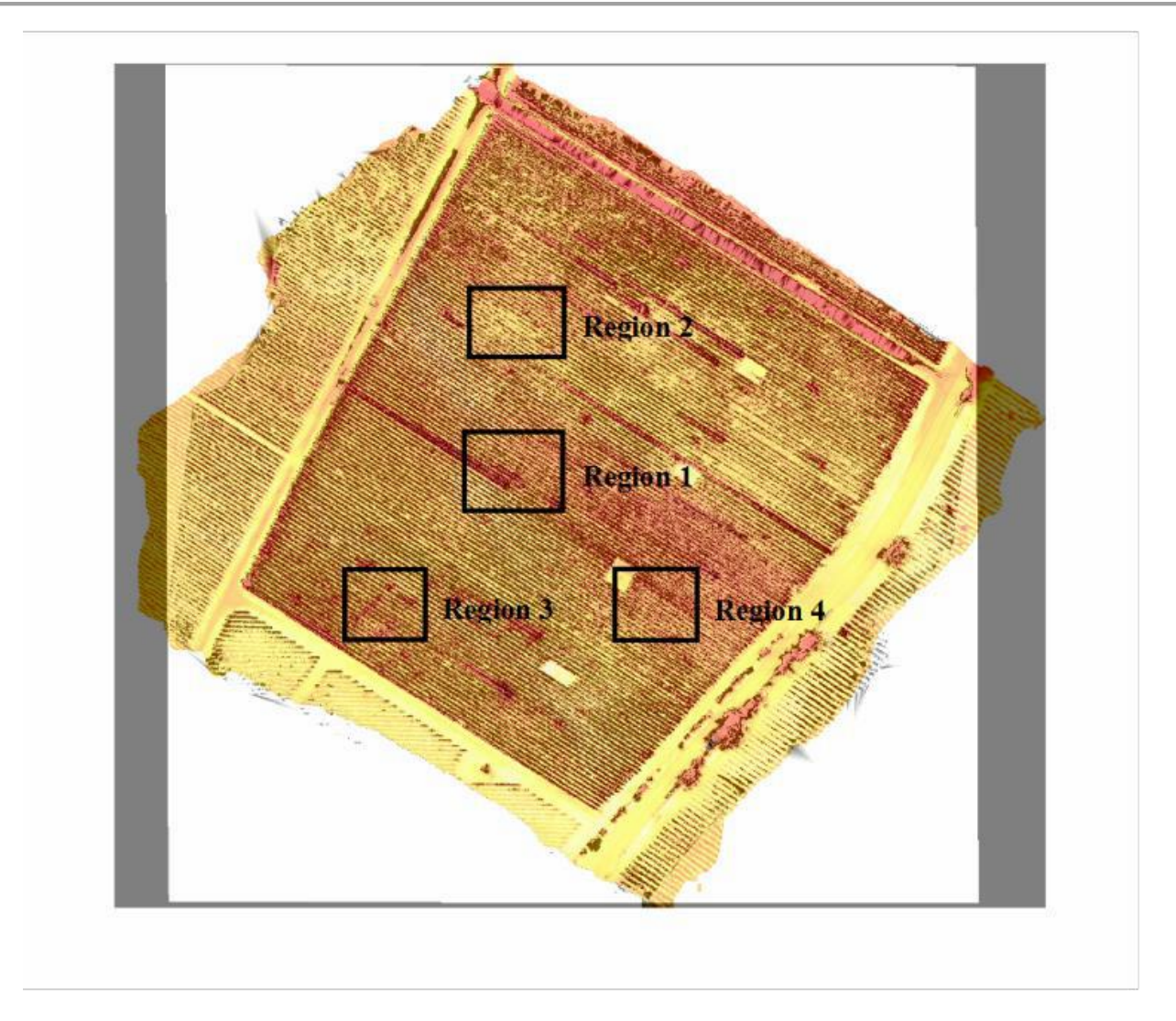


Figure 37: Result of vine identification algorithm using VIS and LWIR data (left) and (right) expanded view of Region 1



**Figure 38:** Superposition of vine segmentation and LWIR observations with a selection of regions that are expanded below for more detailed scrutiny of performance

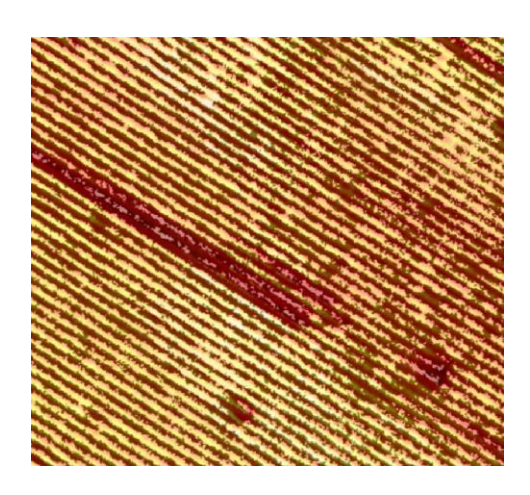
The vine segmentation and ground truth DPCs were then co-registered and superimposed onto one another for visual examination (Figure 38). There are small registration errors apparent in the super- position, particularly in the along row direction. Nevertheless, it is clear, even from this busy image, that the vine segmentation algorithm has successfully identified only vines over most of the vineyard. Closer inspection of an expanded region (Figure 39) confirms the technique's capacity to discriminate between the dense vine foliage where irrigation has been damaged and grass is growing strongly between rows (Region 1, Figure 38).

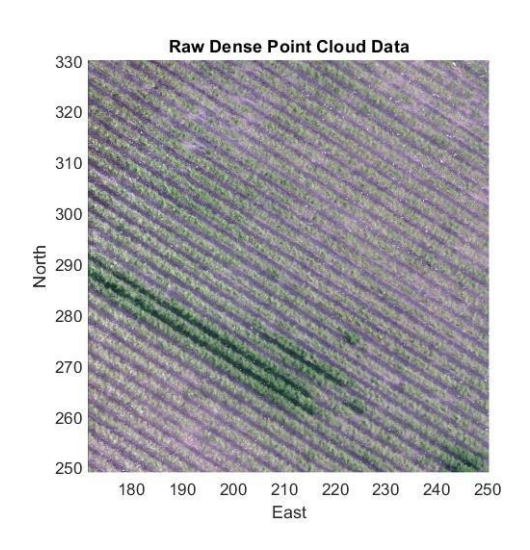
Similarly, the segmentation has successfully dealt with shadowing in both the VIS and LWIR data. Figure 40 (left) shows an expanded view of Region 2 from Figure 38: an area that appears to be only sparsely populated with vines based on the VIS DPC. Figure 40 (right) shows another expanded section of vineyard where the algorithm has had to deal with complex lighting and high foliage density.

A more holistic validation of the segmentation algorithm was evaluated over the entire vineyard by contrasting the identified vine material against thermal imagery. The ground truth data was observed on

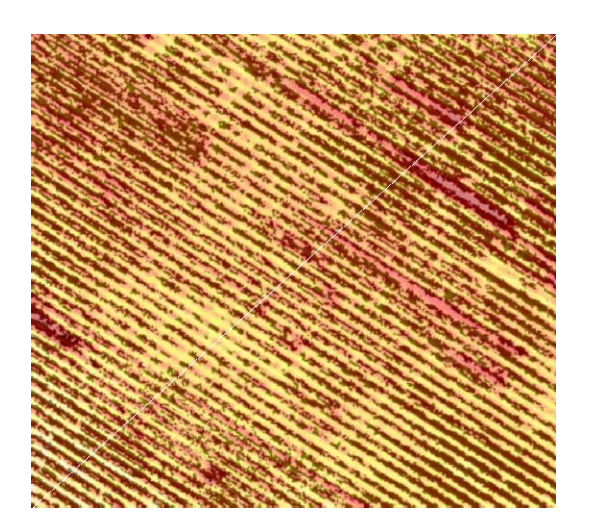
a day for which air temperatures reached about 43°C. As ground brightness temperatures typically reach up to 60°C, but the vine leaves transpire (and their surface temperatures only reach about 40°C), the vines are clearly visible against the background.

Unfortunately, regions in which irrigation infrastructure has broken, areas shaded from the direct effects of the sun and areas with sparse vine density but irrigated also have surface brightness temperatures around 40°C. A data set observed close to local noon (when the sun was near its zenith) was selected (a) to minimise the effects of shadowing and maximise the effects of contrast and (b) because this was prior to the cycle of irrigation, minimising any evapotranspiration effects in sparse vine regions.





**Figure 39:** Expanded views of "Region 1" in Figure 10 (left) and the corresponding VIS DPC (right). In the left-hand image, the superimposed black dots indicate segments identified as vines, whereas yellow and red colouring below these dots indicate higher (likely between row material) and lower (likely vine material) ground temperatures, respectively



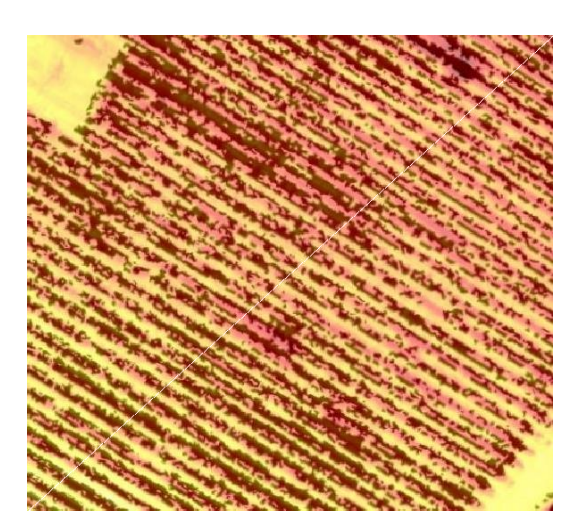


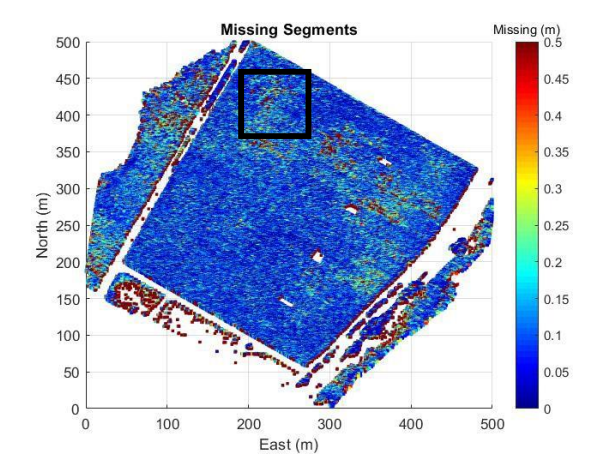
Figure 40: Expanded views of "Region 3" (left) and "Region 4" (right) of Figure 38

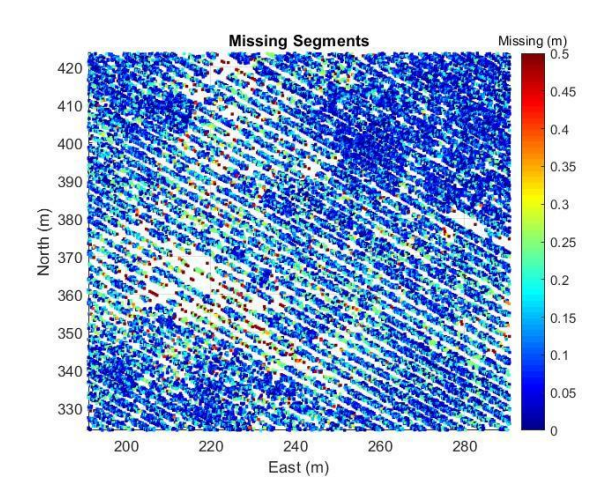
**Hough Transform:** Using the identified vine locations, some useful parameters such as those identified by [1] may now be computed, e.g. row width, height, spacing, cover fraction and missing segments. In order

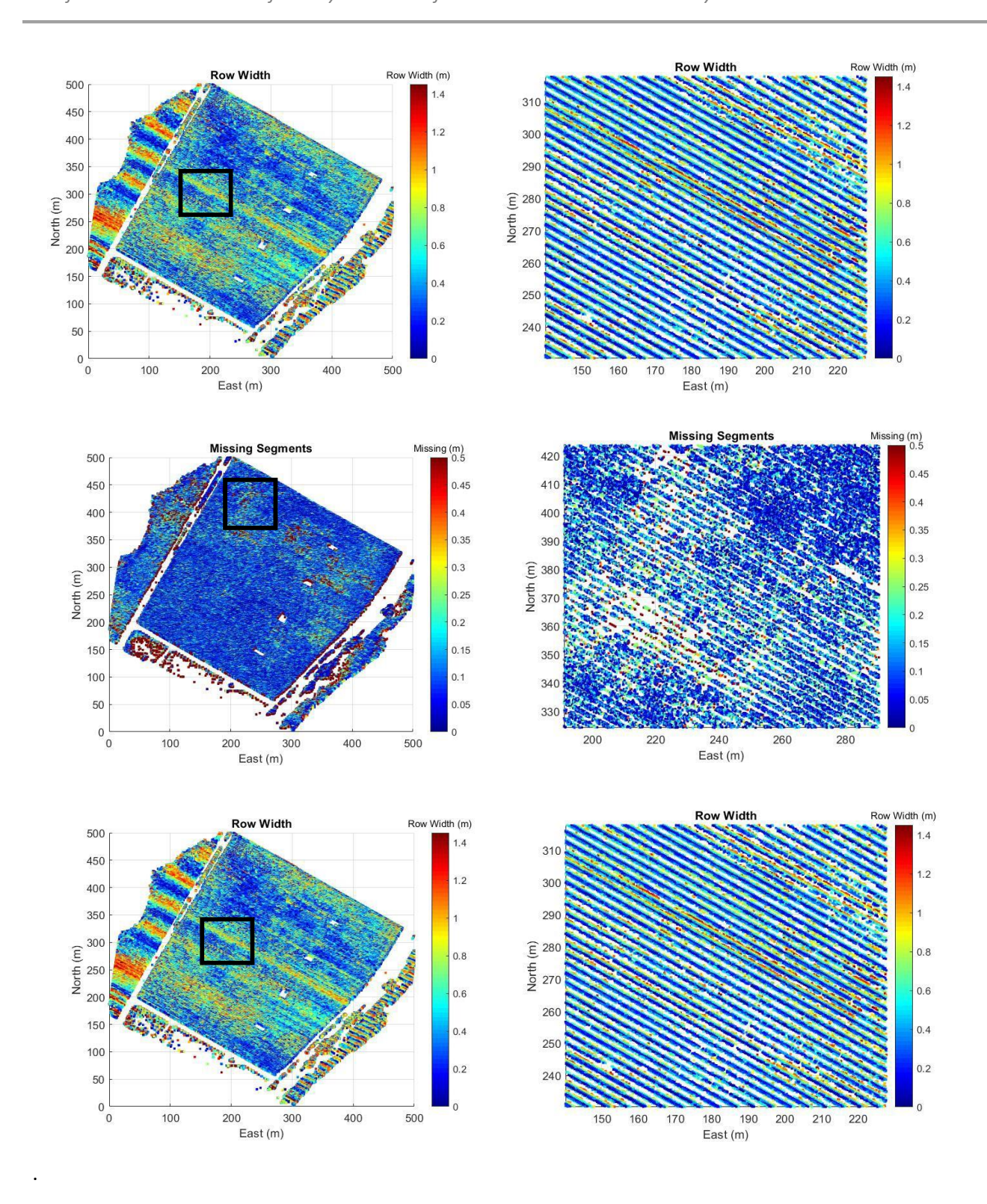
to do this, however, the exact orientation of the vine rows must first be identified. This can be achieved manually, by visually determining row orientation, or automatically, using a Hough transform [57]. This transform uses a parametric representation of a line,  $\rho = x \cos \theta + y \sin \theta$ , where  $\rho$  is the distance from the origin of the DPC to the line along a vector perpendicular to the line, and  $\theta$  is the angle between the x- axis and this vector. The Hough transform is used extensively in image processing to identify continuous point sets that constitute lines in data. Consequently, as vine rows are typically arranged as a set of parallel lines, the method readily identifies row orientation.

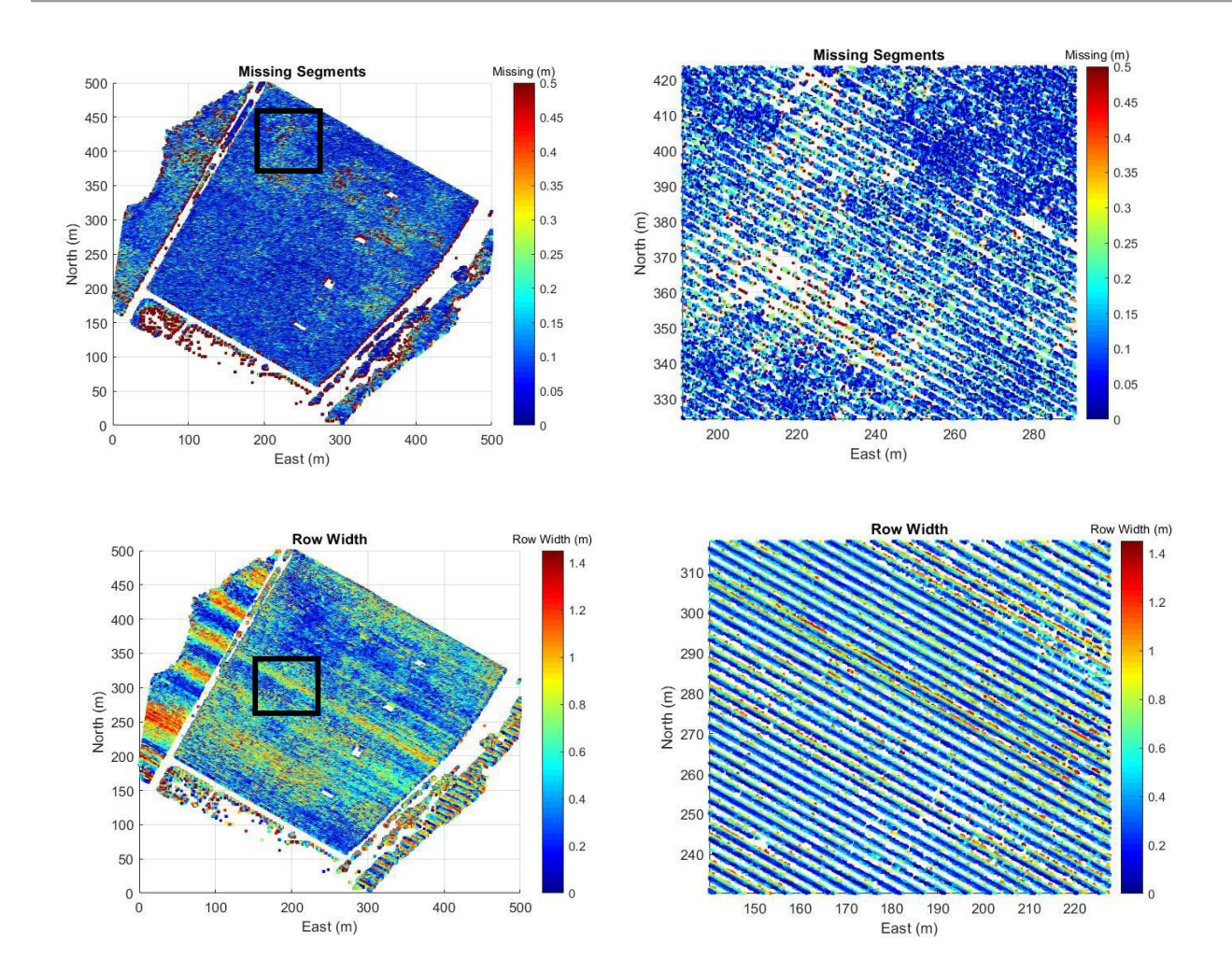
In general, however, a Hough Transform will not successfully determine orientation where vines are planted along iso-altitude curves. Under such circumstances, rotation angles should be computed manually, or the location of the vine rows computed as a function of vineyard geography using an alternative technique. One simple approach is to identify a small section of vine (in the along-row direction) at the left or right extreme of a vineyard, compute the across-row median and row separation, and perform the property identification calculations below for a short vine segment; and then repeat, having advanced to the next segment in the along-row direction (note: this increases the computational cost of the procedure).

**Crop row width:** Crop row width,  $Wc_{ij} = |x_i - x_{M_j}|$ , may be computed for each point in the DPC (Figure 41, upper) [Note: the calculations of row width associated with the vineyards NW and SE of the main 10Ha test site show erroneous values in Figure 41. This is because the row centroids,  $x_{M_j}$ , are computed for the 10Ha vineyard]. The elements of the DPC associated with each row may then be sorted into ascending order and along-row separation distances computed (Figure 41, lower). The more significant breaks in the vine rows are clearly visible. The enlarged view of the data in the right-hand image show gaps in the vines less readily visible in the entire DPC.









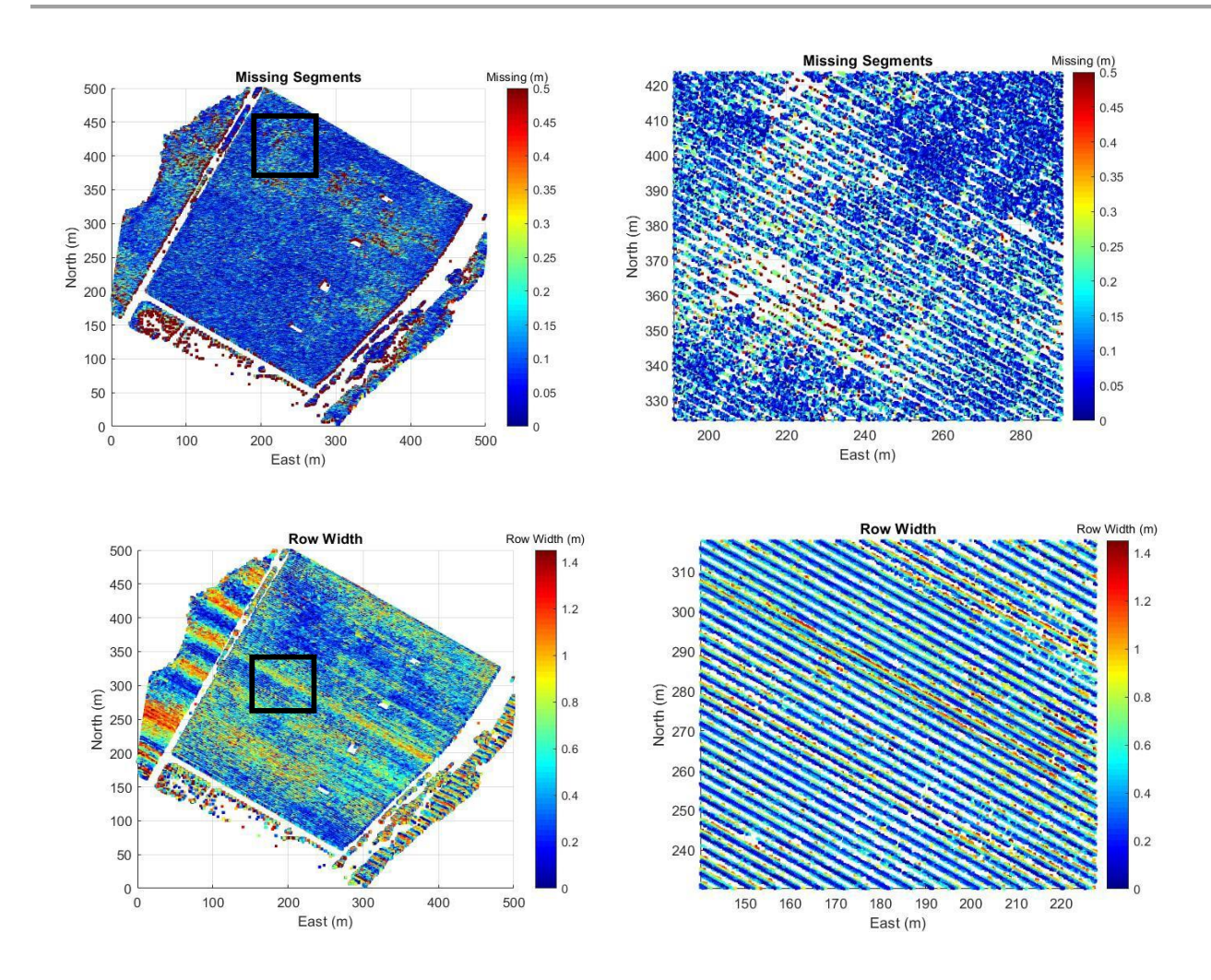


**Figure 41:** Spatial distribution of vine row width (top) and missing row segments (bottom) over vineyard (enlarged views on are shown on right)

The results for vine width estimated by the algorithm were compared to field measurements taken at around seventy points randomly selected throughout the vineyard (Figure 42). A comparison to row width vs stomatal conductance is shown in Figure 43. These measurements were conducted with Dr Vinay Pagay of Adelaide University.

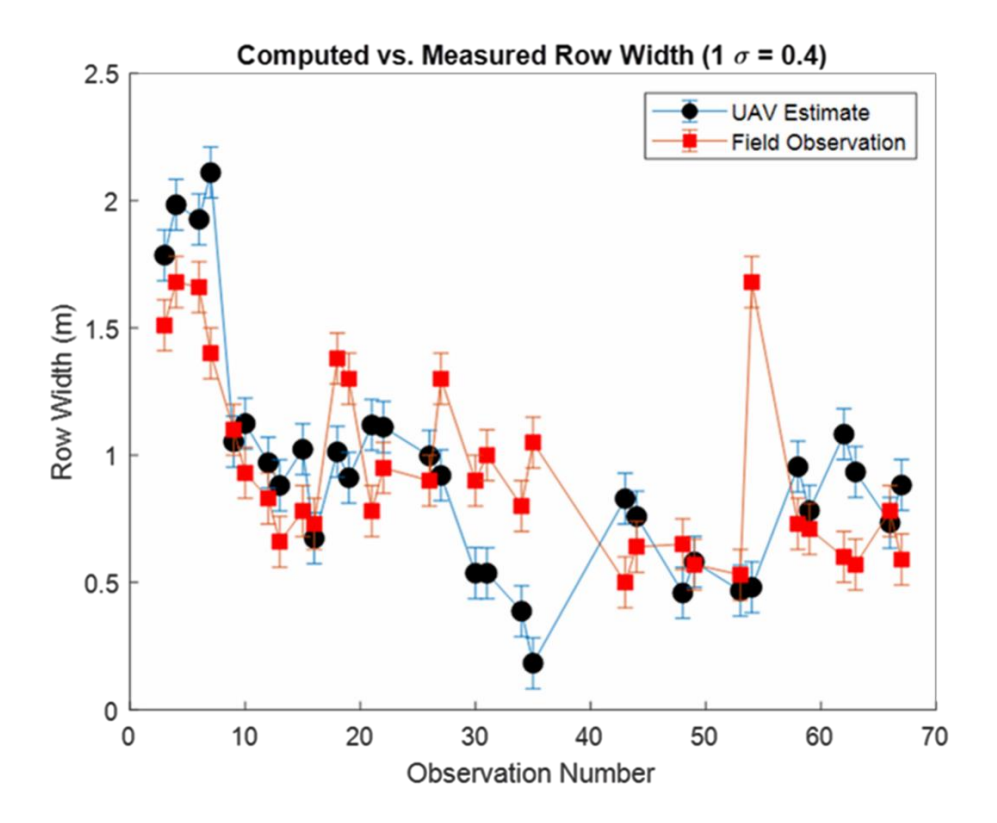


Figure 42:Computed vs. measured row width

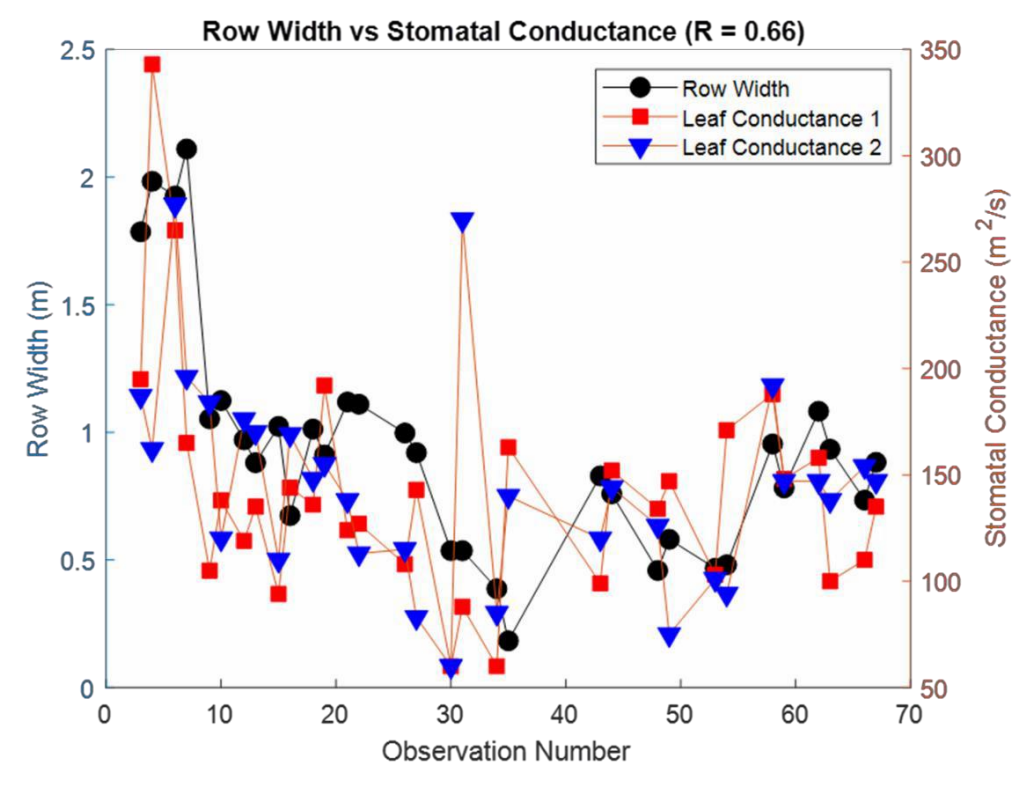


Figure 43: Row width (observed by UAV) vs. stomatal

#### 6 Project evaluation: potential for adoption and lessons learnt

Based on the trials experience gained during the project, there are two possible concepts of operations, one more commercially viable than the other.

The less commercially viable option centres on measurement, visualisation, and delivery of microclimatic conditions for a vineyard in near real time. The key impediments to realising this challenge commercially, however, are linked more to Australian federal UAV regulations and automation of the flying processes than to any technological deficiency of immaturity per se. For example, current air safety regulations apply to UAVs based on their weight; and any drone (plus its payload) weighing more than 2kg must be operated under a Remote Operations Certificate (ReOC) by a licenced operator. Consequently, a drone operator with a ReOC must be employed to operte the system as and when it is required to fly. The commercial rates for such personnel vary, but competent operators cost around \$1,500 per day. Also, unless retained under a suitable commercial arrangement, the operator would likely be required at short notice based on local meteorological measurements and/or predictions. This would impose considerable operational (and hence cost) overheads.

Furthermore, if multi-UAV techniques are not used, the ground sensor component must be deployed; and this takes time, approximately one day per 10Ha. Whilst not skilled work (the deployment needs are like those of an irrigation system), two people are generally required to test sensors. Alternatively, the ground component could be pre-deployed and left in situ for extended periods. This requires the equipment to be weatherproofed and imposes further (modest) cost.

The more commercially viable option for a concept of operations centres around measurement of events over a growing cycle, potentially over several cycles. This can be accomplished either through an extended deployment, which would require weatherproofing of the ground sensors, or a pre-planned deployment of the system throughout one or more years. The advantage of this approach is that for frost events the technology could be used to assess need for frost fans, optimise the location of frost fans, determine the impact of frost protection strategies, generate spatial maps of frost measured over time, and determine the propensity for atmospheric inversions in certain regions. Similarly, for heat stress events, the system can be used to calculate evapotranspiration and CWSI (both as a function of space/geography and time), the spatial variation of plant vigour, and how much irrigation is needed within a vineyard and where.

To substantially reduce costs, would be possible for the entire acoustic tomography system to be replaced with a single sonic anemometer (or several on a tower or distributed spatially). This would cost about \$5,000 per anemometer and a similar amount for a 10m tower. Approximations can then be made with respect to average vertical wind profiles based on Monin-Obukhov Similarity Theory (MOST). Atmospheric buoyancy criteria that permit sensible heat flux to be calculated can also be computed. However, any extrapolations drawn from such point observations would be vastly inferior to those based on AAT and shown in this report.

Under another project, UniSA has worked with a Sydney-based company, Midspar Systems, to miniaturise an acoustic tracking device that could be used in place of the ground sensor data acquisition system. The cost of this system is, however, around \$20,000 per unit, as opposed to about \$5k, not including the power supply and solar panels (noting each Midspar unit can sample 12 microphones as opposed to 7 for the UniSA systems). Moreover, the sensitivity of the Midspar system allows detection and tracking of the sound fields generated by the UAVs at much greater range (3km for petrol-driven UAVs).

Based on the analysis of the AAT, it is likely that the minimum practical ground sensor separation is about 50m, which is 49 sensors and 7 UniSA ground stations per 10Ha vineyard. Other drone systems could be employed, including fixed wing systems, to cover larger areas than this project attempted, but the cost of any such system would scale accordingly.

Payload miniaturisation is also a possibility for the thermographic drone, but the need for a sensor with high thermal accuracy pushes the cost of such a system up to around \$20,000. Less expensive thermographic systems are certainly available (circa \$5,000) but they have very low thermal and spatial resolution and would not deliver the capability demonstrated in this report.

#### 7 Concluding remarks and future work

This project has shown UAV-based acoustic atmospheric tomography (AAT) combined with thermography can be used to accurately estimate and visualise temperature and wind velocity across a vineyard block. During heat events this permits computation of plant stress factors like evapotranspiration (ET) and crop water stress index (CWSI). Similarly, during frost events the technology can provide high resolution thermal maps of the surface and air temperatures surrounding the vineyards as a function of geographic and temporal variation.

In both cases this permits evaluation of the effectiveness and/or need for mitigation strategies, such as frost fans, sprinklers, and irrigation, to be applied with greater discretion. However, as the technology is still in its infancy, the full value of the microclimatic information it offers is still being assessed. Regardless, initial conclusions suggest frost mitigation strategies based on air temperature measurements alone may be suboptimal; and the microclimatic conditions observed during heat stress events suggest opportunities for optimising irrigation, which is normally applied uniformly across a block. This would deliver water and energy savings.

In addition to the above, a technique for identifying and classifying vine properties such as row width, height, cover-fraction, and missing segments was developed. The genesis of this algorithm was as a bi- product of the need for the tomographic-thermographic data fusion routines to uniquely identify the thermographic (LWIR radiation) properties of the vineyard, i.e. the need to automatically separate vines from inter-row material as they have different emissivity. The algorithm offers users the ability to rapidly, efficiently and non-destructively visualise plant vigour as a spatial function of vineyard geography: the information may be integrated into decision support tools to improve management practices.

In the final analysis, the value proposition for a decision support tool based on remote sensing derives not from the capabilities of any given technology or sensor per se, but from a system's holistic potential to improve efficiencies and reduce fieldwork. In other words, when developing aids to support mapping and early identification of vineyard characteristics like disease, biophysical stress and equipment failures—for practical reasons—successful technologies should not critically rely on specialist users who are expert in the design or operation of the relevant software, mathematical techniques or manipulation of information sets. Nor should algorithms make use of machine learning approaches that require training on unique or hard-to-obtain data sets. They should intrinsically cope with sub-optimal equipment configurations and reasonable performance degradation in the processing chain. Ideally, users should need to supply only a few intuitive parameters. This technology has not yet reached a level of maturity that would allow non-specialist users to deploy and operate it in the field. However, in the right hands, it offers significant research potential for examination of vineyard blocks subject to weather stress events.

Potential follow-on work could entail use of the technology developed under this project to accurately determine ET across a vineyard block over a growing season. Such a goal would be achieved in two steps:

1) Estimation of seasonal crop coefficients: The spatial and temporal patterns of vine canopy development at key phenological stages from flowering to harvest would be determined using high resolution RGB/LWIR cameras flown onboard a UAV. Canopy width and height extracted from aerial this imagery would then be used to estimate the crop coefficient (note: crop coefficient is related to the area of exposed leaves). These remotely-sensed crop coefficients would be validated and refined using the

ground-based Paso Panel technique based on canopy light interception developed by the University of Adelaide.

2) Obtaining ET: AAT would be used to estimate reference ET (ET0) via temperature and wind speed measurements, with relative humidity and solar radiation provided by an on-site weather station. Using these environmental parameters, high spatial resolution ET0 would then be calculated via the Penman- Monteith equation for the vineyard. ET0 and crop coefficients determined in the first step will be used to calculate ET across the vineyard block and over the course of the growing season.

In addition, the thermal imagery obtained from the UAV-mounted infrared camera would be used to characterise patterns of water stress across the block and compared with the spatial and temporal patterns of the difference between irrigation applications and ET to estimate soil water deficits and hence vine water stress.

#### 8 Project media and publications

Preliminary Evaluation of Atmospheric Temperature And Wind Profiles Obtained Using Unmanned Aerial Vehicle Based Acoustic Tomography A. Finn, K. Rogers, J. Meade, J. Skinner, and A. Zargarian. Int. Arch. Photogramm. Remote Sens. Spatial Inf. Sci., XLII-2/W13, 283–287, https://doi.org/10.5194/isprs-archives-XLII-2-W13-283-2019, 2019

#### **Extraction of Vineyard Macrostructure From Sub-Optimal Sequences Of Aerial Imagery**

A. Finn, A. Melville-Smith, and R. Brinkworth. ISPRS Ann. Photogramm. Remote Sens. Spatial Inf. Sci., IV-2/W5, 103–110, https://doi.org/10.5194/isprs-annals-IV-2-W5-103-2019, 2019

**The sound of science** Anthony Finn. SPAA, Society of Precision Agriculture Australia, Precision Ag News, Volume 16, Issue 1, 2019

Accurate group velocity estimation for unmanned aerial vehicle-based acoustic atmospheric tomography Kevin J. Rogers and Anthony Finn. The Journal of the Acoustical Society of America 141, 1269 (2017); https://doi.org/10.1121/1.4976818

Spatio-temporal observations of temperature and wind velocity using drone-based acoustic atmospheric tomography Anthony Finn, Kevin Rogers, Joshua Meade, Jarrod Skinner and Amir Zhargarian. The Journal of the Acoustical Society of America 145, 1903 (2019); https://doi.org/10.1121/1.5101906

**Drones offer the chance of real-time micro-climate information** Nick Carne, Wine Australia Newsletter, 07 April 2017

**Drones showing their value in vineyards** Nick Carne, Wine Australia Newsletter, 08 June 2018

### 9 Intellectual property

A vine row identification technique was created to better estimate the emissivity used for the calculation of evapotranspiration.

#### References

- 1. Weiss, M. and F. Baret, *Using 3D Point Clouds Derived from UAV RGB Imagery to Describe Vineyard 3D Macro-Structure*. Remote Sensing 2017. **9**(1).
- 2. Zarco-Tejada, P.J., et al., Assessing vineyard condition with hyperspectral indices: Leaf and canopy reflectance simulation in a row-structured discontinuous canopy. Remote Sensing & Environment, 2005. **99**: p. 271–287.
- 3. Meggio, F., et al., Row orientation and viewing geometry effects on row-structured vine crops for chlorophyll content estimation. Canadian Journal of Remote Sensing 2008. **34**: p. 220–234.
- 4. López-Lozano, R., et al., *Optimal geometric configuration and algorithms for lai indirect estimates under row canopies: The case of vineyards* Agriculture, Forestry & Meteorology 2009. **149**: p. 1307–1316.
- 5. Holben, B.N. and C.O. Justice, *The topographic effect on spectral response from nadir-pointing sensors.* Photogrammetry, Engineering & Remote Sensing, 1980. **46**: p. 1191–1200.
- 6. Shepherd, J.D. and J.R. Dymond, *Correcting satellite imagery for the variance of reflectance and illumination with topography.* International Journal of Remote Sensing, 2003. **24**: p. 3503–3514.
- 7. Johnson, L., et al., *Remote sensing of vineyard management zones: Implications for wine quality.*Applied Engineering in Agriculture, 2001. **17**: p. 557–560.
- 8. Dobrowski, S.Z., S.L. Ustin, and J.A. Wolpert, *Grapevine dormant pruning weight prediction using remotely sensed data*. Aust. J. Grape Wine Res. , 2003. **9**: p. 177–182.
- 9. Smit, J.L., G. Sithole, and A.E. Strever, *Vine signal extraction—An application of remote sensing in precision viticulture*. . South African Journal of Enology & Viticulture, 2010. **31**: p. 65–74.
- 10. Fiorillo, E., et al., *Airborne high-resolution images for grape classification: Changes in correlation between technological and late maturity in a sangiovese vineyard in central Italy.* Australian Journal of Grape & Wine Research, 2012. **18**: p. 80–90.
- 11. Hernández-Clemente, R., R.M. Navarro-Cerrillo, and P.J. Zarco-Tejada, *Carotenoid content estimation in a heterogeneous conifer forest using narrow-band indices and PROSPECT + DART simulations*. Remote Sensing & Environment, 2012. **127**: p. 298–315.
- 12. Zarco-Tejada, P.J., et al., *Estimating leaf carotenoid content in vineyards using high resolution hyperspectral imagery acquired from an unmanned aerial vehicle (UAV)*. Agriculture Forestry & Meteorology, 2013. **171–172**: p. 281–294.
- 13. Rey, C., et al., *Multispectral imagery acquired from a UAV to assess the spatial variability of a tempranillo vineyard.* Precision Agriculture, 2013. **13**: p. 617–624.

- 14. Candiago, S., et al., Evaluating multispectral images and vegetation indices for precision farming applications from UAV images Remote Sensing, 2015. **7**: p. 4026–4047.
- 15. Lacar, F.M., M.M. Lewis, and I.T. Grierson, *Use of hyperspectral imagery for mapping grape varieties in the Barossa Valley, South Australia*, in *IEEE International Geoscience and Remote Sensing Symposium*. 2001: Sydney, Ausralia, 9–13 July. p. 2875–2877.
- 16. Ferreiro-Armán, M., et al., *Hyperspectral image analysis for precision viticulture*. Image Analysis and Recognition, ed. A. Campilho and M. Kamel. Vol. 4142. 2006, Berlin/Heidelberg, Germany: Springer. 730–741.
- 17. Zarco-Tejada, P.J., V. González-Dugo, and J.A.J. Berni, *Fluorescence, temperature and narrow-band indices acquired from a UAV platform for water stress detection using a micro- hyperspectral imager and a thermal camera.* Remote Sensing & Environment, 2012. **117**: p. 322–337.
- 18. Rouse, J.W., et al., *Monitoring the Vernal Advancement of Retrogradation of Natural Vegetation* 1974, NASA: Texas A&M University, College Station, TX, USA.
- 19. Finn, A. and S. Franklin, *UAV-based atmospheric tomography*, in *Australian Acoustical Society Conference*. 2011.
- 20. Finn, A. and K. Rogers, *The feasibility of unmanned aerial vehicle-based acoustic atmospheric tomography.* J Acoust Soc Am, 2015. **138**(2): p. 874-889.
- 21. Finn, A. and K. Rogers, *Improving Unmanned Aerial Vehicle-Based Acoustic Atmospheric Tomography by Varying the Engine Firing Sequence of the Aircraft.* Journal of Atmospheric and Oceanic Technology, 2016. **33**(4): p. 803-816.
- 22. Finn, A. and K. Rogers, *Acoustic Atmospheric Tomography Using Multiple Unmanned Aerial Vehicles.* IET Radar, Sonar & Navigation, 2016. **10**: p. 1541–1551.
- 23. Finn, A. and K. Rogers, *An Analysis of Unmanned Aerial Vehicle-Based Acoustic Atmospheric Tomography* in *Acoustics 2016*. 2016, Australian Acoustical Society: Brisbane, Australia.
- 24. Rogers, K. and A. Finn, *Three-Dimensional UAV-Based Atmospheric Tomography.* J. Atmos. & Oceanic Techn., 2013. **30**(2): p. 336-344.
- 25. Rogers, K. and A. Finn, *Frequency estimation for 3D atmospheric tomography using unmanned aerial vehicles*, in *Proc. IEEE 8th Int. Conf. Intell. Sens., Sens. Netw. Inf. Proc., 2013* 2013, IEEE. p. 390-395.
- 26. Skelton, P., R.S.A. Brinkworth, and A. Finn, *Real time visual rotational velocity estimation using a biologically-inspired algorithm on embedded hardware*, in *Digital Image Computing: Techniques and Applications (DICTA*). 2017: Sydney
- 27. Usamentiaga, R., et al., *Infrared Thermography for Temperature Measurement and Non-Destructive Testing.* Sensors, 2014. **14**(7): p. 12305-12348.
- 28. Longuet-Higgins, H.C., A computer algorithm for reconstructing a scene from two images. Nature, 1981.
- 29. Furukawa, Y. and J. Ponce, *Accurate, dense, and robust multiview stereopsis.* IEEE Transactions in Pattern Analysis & Machine Intelligence, 2010. **32**: p. 1362–1376.
- 30. Hartley, R., *In defense of the eight-point algorithm.* IEEE Transactions of Pattern Analysis & Machine Inteligence, 1997. **19**: p. 580–593.
- 31. Lowe, D.G., *Object recognition from local scale-invariant features*, in *IEEE International Conference on Computer Vision*. 1999. p. 1150-1157.
- 32. Bay, H., et al., *SURF: Speeded Up Robust Features*. Computer Vision and Image Understanding, 2008. **110**(3): p. 346-359.
- 33. Lawrance, N. and S. Sukkarieh, *Path planning for autonomous soaring flight in dynamic wind fields*, in *IEEE International Conference on Robotics and Automation (ICRA 2011)*. 2011: Shanghai, China, 2011.

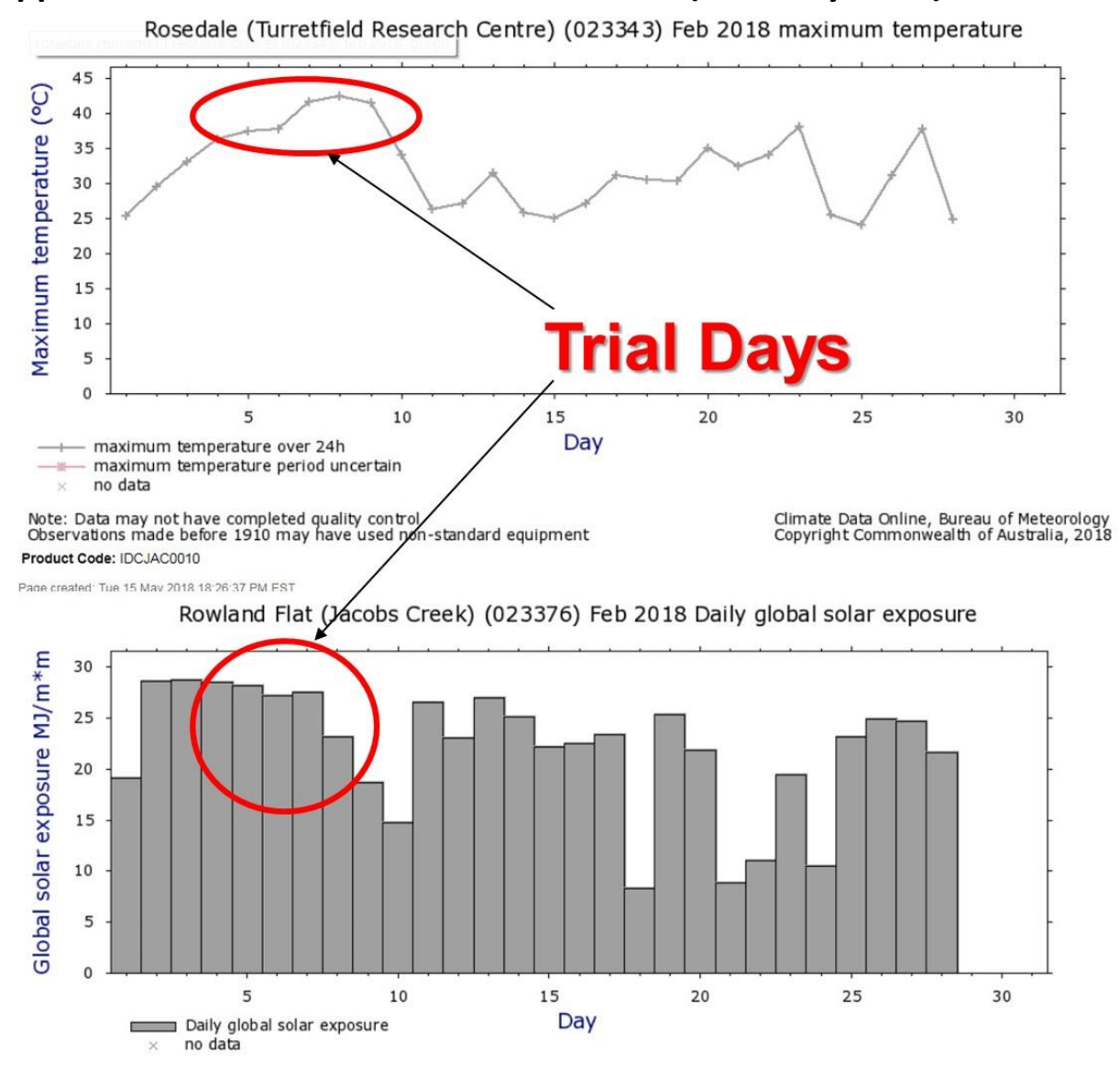
- 34. J. Langelaan, J.S., C. Montella, and J. Grenestedt, *Wind Field Estimation for Autonomous Dynamic Soaring*, in *IEEE International Conference on Robotics and Automation (ICRA)*. 2012.
- 35. Sullivan, P.P. and E.G. Patton, *The effect of mesh resolution on convective boundary layer statistics and structures generated by large-eddy simulation.* Journal of the Atmospheric Sciences, 2011. **68**(10): p. 2395-2415.
- 36. Rogers, K. and A. Finn, *3D UAV-based atmospheric tomography: Preliminary trials results.* Proc. Aust. Acoust. Soc. Conference, Victor Harbour, 2013.
- 37. Ostashev, V., et al., Source localization from an elevated acoustic sensor array in a refractive atmosphere. J. Acoust. Soc. Am., 2008. **124**(6): p. 3413-3420.
- 38. Ziemann, A., K. Arnold, and A. Raabe, *Acoustic tomography as a remote sensing method to investigate the near-surface atmospheric boundary layer in comparison with in situ measurements*. Journal of Atmospheric and Oceanic Technology, 2002. **19**(8): p. 1208-1215.
- 39. Brutsaert, W., *Evapotranspiration into the Atmosphere: Theory, History and Applications.* . Environmental Fluid Mechanics. 1984: Springer. 299.
- 40. Jones, H.G., *Plants and Microclimate: A Quantitative Approach to Environmental Plant Physiology*. Third Edition ed. 2015, Cambridge: Cambridge University Press.
- 41. R. Allen, L.P., D. Raes & M. Smith, *Crop evapotranspiration Guidelines for computing crop water requirements FAO Irrigation and drainage paper 56*. 1998, FAO Food and Agriculture Organization of the United Nations: Rome.
- 42. R. Allen, I.W., R. Elliott, T. Howell, D. Itenfisu, M. Jensen, *ASCE Standardized Reference Evapotranspiration Equation*. 2005, American Society of Civil Engineers. p. 1-55.
- 43. Jones, H.G., et al., *Thermal infrared imaging of crop canopies for remote diagnosis and quantification of plant responses to water stress in the field.* Functional Plant Biology, 2009. **36**: p. 978-989.
- 44. Puletti, N., R. Perria, and P. Storchi, *Unsupervised classification of very high remotely sensed images for grapevine rows detection.* European Journal of Remote Sensing, 2014. **47**: p. 45–54.
- 45. Wassenaar, T., et al., *Vineyard identification and description of spatial crop structure by per-field frequency analysis.* Int. J. Remote Sens, 2002. **23**: p. 3311–3325.
- 46. Chanussot, J., P. Bas, and L. Bombrun, *Airborne remote sensing of vineyards for the detection of dead vine trees*, in *IEEE International Geoscience and Remote Sensing Symposium*. 2005: Seoul, Korea. p. 3090–3093.
- 47. Delenne, C., et al., From pixel to vine parcel: A complete methodology for vineyard delineation and characterization using remote-sensing data. Computers & Electronics in Agriculture, 2010: p. 78–83.
- 48. Mathews, A. and J. Jensen, *Visualizing and quantifying vineyard canopy LAI using an unmanned aerial vehicle (UAV) collected high density structure from motion point cloud.* Remote Sensing, 2013. 5.
- 49. Bendig, J., A. Bolten, and G. Bareth, *UAV-based imaging for multi-temporal, very high resolution crop surface models to monitor crop growth variability.* PFG Journal of Photogrammetry, Remote Sensing and Geoinformation Science, 2013. **6**: p. 551–562.
- 50. Bentley, J.L., *Multidimensional binary search trees used for associative searching.* Communications of the ACM, 1975. **18**(9).
- 51. Elseberg, J., et al., *Comparison of nearest-neighbor-search strategies and implementations for efficient shape registration.* Journal of Software Engineering for Robotics, 2012. **3**(1): p. 2-12.
- 52. MacQueen, J., Some methods for classification and analysis of multivariate observations, in Berkeley Symposium on Mathematical Statistics and Probability. 1967, University of California PressBerkeley Symposium on Mathematical Statistics and Probability: Berkeley, California. p. 281.

- 53. Nistér, D., *Preemptive RANSAC for live structure and motion estimation*. Machine Vision and Applications, 2005. **16**(5): p. 321-329.
- 54. Zhou, K., et al., *Real-time KD-tree construction on graphics hardware.* ACM Transactions on Graphics (TOG) 2008. **27** (5).
- 55. Holland, P. and R. Welsch, *Robust regression using iteratively reweighted least-squares.* Comms & Statistical Theory & Methods, 1977. **6**: p. 813-827.
- 56. Chen, J., et al., A simple method for reconstructing a high-quality NDVI time-series data set based on the Savitzky–Golay filter. Remote Sensing of Environment, 2004. **91**(3–4): p. 332-344.
- 57. Ballard, D.H., *Generalizing the Hough transform to detect arbitrary shapes.* Pattern Recognition, 1981. **13**(2): p. 111-122.

### **Acknowledgements**

This project was funded by the Australian Government Department of Agriculture Water and the Environment Rural R&D for Profit program with co-investment from Wine Australia, Pernod Ricard Winemakers, La Trobe University, the Australian Wine Research Institute and the Department of Jobs, Precincts and Regions in Victoria. This work was funded by Wine Australia contract PPA1125, RRD4P Digital Technologies Project: Use of Unmanned Air Vehicles for early, real time detection of extreme weather events in vineyards.

## Appendix: Additional heat stress trial data (February 2018)



Climate Data Online, Bureau of Meteorology Copyright Commonwealth of Australia, 2018

# Rosedale, South Australia February 2018 Daily Weather Observations

## 8km away

| Observations | are from | Turretfield | Research | Centre |
|--------------|----------|-------------|----------|--------|
|              |          |             |          |        |

| Date   |                  | ay will wax | Dain                        | Evap   | Sun   | Max wind gust |       | 9 am |    |     |     |  | 3 pm |  |    |                 |      |    |
|--|------------------|-------------|-----------------------------|--|-------|---------------|-------|------|----|-----|-----|--|------|--|----|-----------------|------|----|
|  | Day              |             |                             |  |       | Dir Spd       |       |      |    |     |     | The state of the s |      | the last of the la |    |                 |      |    |
|  |                  | °C °C       |                             |  | hours | km/h          | local |      |    |     |     | km/h   | hPa  | ٥.   | 96 | 8 <sup>th</sup> | km/h | hP |
| 1  |                  | 13.0 25.2   | 177                         | 5.6  |       |               |       | 14.8 |    | 7   |     |  | 1470 |  |    |                 |      |    |
| 2  |                  | 14.0 29.5   | 0                           | 6.8  |       |               |       | 19.4 |    | 6   | E   |  |      |  |    |                 |      |    |
| 3  |                  | 18.5 33.0   | 0                           | 9.4  |       |               |       | 22.2 |    | 0   |     |  |      |  |    |                 |      |    |
| 4  | Su               | 20.0 36.2   | 0                           | 10.0   |       |               |       | 27.3 | 42 | 0   | E   | 4  |      | _  | т. |                 | . 1  |    |
| 5  | Mo               | 15.8 37.3   | 0                           | 10.8   |       |               |       | 32.8 | 24 | 3   | -   | Calm   |      | -  | ır | ia              | 31   |    |
| 6  | Tu               | 18.1 37.6   | 0                           | 11.6   |       |               |       | 26.9 | 43 | 2   |     | Calm   |      |  | ٠. |                 | 41   |    |
| 7  | We               | 22.2 41.5   | 0                           | 10.2   |       |               |       | 30.1 | 45 | 4   | ENE | 2  |      |  |    |                 |      |    |
| 8  | Th               | 21.4 42.3   | 0                           | 12.6   |       |               |       | 34.0 | 43 | 7   | NE  | 4  |      |  |    |                 |      |    |
| 9  |                  | 26.6 41.3   |                             | 14.2   |       |               |       | 29.6 | 52 | 8   | SE  | 7  |      |  |    |                 |      |    |
| 10   | Sa               | 24.0 34.0   | 0                           | 11.4   |       |               |       | 27.0 | 43 | 8   | SW  | 2  |      |  |    |                 |      |    |
| 11   | Su               | 10.5 26.3   | 0                           | 6.8  |       |               |       | 17.7 | 73 | 3   | NW  |  |      |  |    |                 |      |    |
| 12   | Mo               | 8.6 27.0    | 0                           | 7.8  |       |               |       | 17.0 | 70 | 8   | Е   | 2  |      |  |    |                 |      |    |
| 13   | Tu               | 9.4 31.4    | 0                           | 5.4  |       |               |       | 18.4 | 72 | 0   |     |  |      |  |    |                 |      |    |
| 14   |                  | 14.8 25.7   | 0                           | 8.0  |       |               |       | 20.0 |    | 8   | SW  |  |      |  |    |                 |      |    |
| 15   |                  | 7.0 25.0    | 0                           | 8.0  |       |               |       | 16.0 |    |     | WNW |  |      | -  |    |                 |      |    |
| 16   |                  | 13.0 27.0   | 0                           | 5.8  |       |               |       | 20.0 |    | 8   |     | Calm   |      |  |    |                 |      |    |
| 17   |                  | 11.5 31.0   | 0                           | 6.8  |       |               |       | 18.0 |    | 1   |     |  |      |  |    |                 |      |    |
| 18   |                  | 18.0 30.4   | 0                           | 6.0  |       |               |       | 23.3 |    |     |     |  |      |  |    |                 |      |    |
| 19   |                  | 16.5 30.2   | 4.0                         | 4.2  |       |               |       | 19.6 |    | 2   |     | Calm   |      |  |    |                 |      |    |
| 20   |                  | 19.2 35.0   | 0                           | 7.2  |       |               |       | 24.2 |    | 7   |     |  |      |  | 1  |                 |      |    |
| 21   |                  | 22.5 32.3   |                             | 7.2  |       |               |       | 27.0 |    | _   |     | Calm   |      |  |    |                 |      |    |
| 22   |                  | 21.5 34.0   | 0.6                         | 4.2  |       |               |       | 23.5 |    | 8   | ENE |  |      |  |    |                 |      |    |
| 23   |                  | 23.3 38.0   | 0.0                         | 8.8  |       |               |       | 34.0 |    | 5   | NE  |  |      |  |    |                 |      |    |
| 24   |                  | 19.2 25.5   | 1.2                         |  |       |               |       | 19.7 |    |     | WSW |  |      |  |    |                 |      |    |
| 25   |                  | 15.0 24.0   | 0                           | 4.0  |       |               |       | 17.2 |    | 7   | SE  |  | -    |  |    |                 |      |    |
| 26   |                  | 7.6 31.0    | 0                           | 6.0  |       |               |       | 16.2 |    | 0   |     |  |      |  | -  |                 |      |    |
| 11/2   |                  | 12.8 37.6   |                             | 6.6  |       |               |       | 24.6 |    |     | SE  |  |      | -  | -  |                 |      |    |
| 27   |                  |             |                             |  |       | /             |       |      |    |     |     |  |      | -  | -  |                 |      |    |
|  | Section Sections | 16.4 24.8   | and the same of the same of | CAPACITATION OF THE PARTY OF TH |       |               |       | 19.5 | 63 | - 1 | VV  | 15   |      |  |    |                 |      |    |
|  |                  | for Febru   |                             |  |       |               |       |      |    |     |     | 112  |      |  |    |                 |      | γ. |
|  |                  | 16.4 31.9   |                             | 8.0  |       |               |       | 22.9 |    |     |     | 4  |      |  |    |                 |      |    |
|  |                  | 7.0 24.0    |                             |  |       |               |       | 14.8 |    |     |     | Calm   |      |  |    |                 |      |    |
| and the latest and th |                  | 26.6 42.3   |                             |  |       |               |       | 34.0 | 93 | 8   | #   | 15   |      |  | 1  |                 |      |    |
|  | Total            | 1.201802 Pr |                             | 224.0  |       |               |       |      |    |     |     |  |      |  |    |                 |      |    |

IDCJDW00001.201602 Prepared at 13.02 010 on Indrsday 3 May 2016

#### Source of data

Observations were drawn from Rosedale (Turretfield Research Centre) {station 023343}.

You should read the important information in these notes.